PHOTONICS RESEARCH AND DEVELOPMENT FINAL REPORT

"An R&D project designed to develop advanced lighting technologies that will improve national energy conversion efficiencies, reduce heat load, increase brightness and significantly lower the cost of conventional lighting technologies"

Funded by the U.S. Department of Energy
Solar Technologies Program

Contract DE-FG36-05GO85032

Award Recipient:

UNLV RESEARCH FOUNDATION
8311 W. Sunset Road, Suite 200
Las Vegas, NV 89113
702-895-2833
Elizabeth.Dickson@unlv.edu

PHOTONICS RESEARCH AND DEVELOPMENT
FINAL REPORT
UNLV RESEARCH FOUNDATION
Contract DE-FG36-05GO85032

TABLE OF CONTENTS

PHOTONICS RESEARCH AND DEVELOPMENT
FINAL REPORT
UNLV RESEARCH FOUNDATION
Contract DE-FG36-05GO85032

ABSTRACT

During the period August 2005 through October 2009, the UNLV Research Foundation (UNLVRF), a non-profit affiliate of the University of Nevada, Las Vegas (UNLV), in collaboration with UNLV's Colleges of Science and Engineering; Boston University (BU); Oak Ridge National Laboratory (ORNL); and Sunlight Direct, LLC, has managed and conducted a diverse and comprehensive research and development program focused on light-emitting diode (LED) technologies that provide significantly improved characteristics for lighting and display applications. This final technical report provides detailed information on the nature of the tasks, the results of the research, and the deliverables.

It is estimated that about five percent of the energy used in the nation is for lighting homes, buildings and streets, accounting for some 25 percent of the average home's electric bill. However, the figure is significantly higher for the commercial sector. About 60 percent of the electricity for businesses is for lighting. Thus replacement of current lighting with solid-state lighting technology has the potential to significantly reduce this nation's energy consumption – by some estimates, possibly as high as 20%.[1]

The primary objective of this multi-year R&D project has been to develop and advance lighting technologies to improve national energy conversion efficiencies; reduce heat load; and significantly lower the cost of conventional lighting technologies. The UNLVRF and its partners have specifically focused these talents on (1) improving LED technologies; (2) optimizing hybrid solar lighting, a technology which potentially offers the benefits of blending natural with artificial lighting systems, thus improving energy efficiency; and (3) building a comprehensive academic infrastructure within UNLV which concentrates on photonics R&D.

Task researchers have reported impressive progress in (1) the development of quantum dot laser emitting diodes (QDLEDs) which will ultimately improve energy efficiency and lower costs for display and lighting applications (UNLV College of Engineering); (2) advancing green LED technology based on the Indium-Gallium-Nitride system (BU), thus improving conversion efficiencies; (3) employing unique state-of-the-art X-ray, electron and optical spectroscopies with microscopic techniques to learn more about the electronic structure of materials and contacts in LED devices (UNLV College of Science); (4) establishing a UNLV Display Lighting Laboratory staffed with a specialized team of academic researchers, students and industrial partners focused on identifying and implementing engineering solutions for lighting display-related problems; and (5) conducting research, development and demonstration for HSL essential to the resolution of technological barriers to commercialization.

---

[1] "Energy Consumption," dated 2008, by the National Energy Education Development (NEED) project

PHOTONICS RESEARCH AND DEVELOPMENT
FINAL TECHNICAL ACCOMPLISHMENT REPORT

Project Title:	Photonics Research and Development
Project Period:	August 1, 2005 – October 30, 2009
Date of Report:	December 15, 2009
Recipient:	The UNLV Research Foundation
Award Number:	DE-FG36-05GO85032
Working Partners:	University of Nevada, Las Vegas Boston University Oak Ridge National Laboratory Sunlight Direct, LLC
Cost-Sharing Partners:	YESCO (Young Electric Sign Company), Las Vegas Video Walls, Inc., Las Vegas, NV Tecnovision, Milan, Italy
Contacts:	Robert F.D. Perret, Project Manager (702) 630-1542 Linda M. Smith, Project Administrator (702) 275-2297

INTRODUCTION

It is estimated that about five percent of the energy used in the nation is for lighting homes, buildings and streets, accounting for some 25 percent of the average home's electric bill. However, the figure is significantly higher for the commercial sector. About 60 percent of the electricity for businesses is for lighting.[2] Most homes still use the traditional incandescent bulbs invented by Thomas Edison which convert only ten percent of the electricity they use to produce light. The other 90 percent is converted into heat. Most commercial buildings have been converted to fluorescent lighting which has higher installation costs but uses much less energy to produce the same amount of illumination. Replacement of current lighting with solid-state lighting (SSL) has the potential to significantly reduce this nation's energy consumption – by some estimates, possibly as high as 20% - translating to a cumulative savings on electric bills of more than $125 billion through 2025 for the consumer.[3]

Recognizing the significance of new lighting technologies to this country's commitment to energy independence, in August 2005 the UNLV Research Foundation (UNLVRF), a non-profit affiliate of the University of Nevada, Las Vegas (UNLV), assembled a diverse team of talented academic researchers who are at the forefront of developing new lighting technologies as well as building the photonics scientific and engineering talent of the future. This team includes

---

[2] "Energy Consumption," dated 2008, by The National Energy Education Development (NEED) Project - http://www.need.org/needpdf/infobook_activities/SecInfo/ConsS.pdf

[3] See http:/lighting.sandia.gov

representation from UNLV's Colleges of Science and Engineering, Boston University's (BU) Photonics Center, Oak Ridge National Laboratory (ORNL), and Sunlight Direct, LLC, of Knoxville, TN.

PROJECT OBJECTIVES

The *primary objective* of this multi-year R&D project has been to develop and advance lighting technologies that will improve national energy conversion efficiencies, reduce heat load, and significantly lower the cost of conventional lighting technologies.

A *secondary objective* has been to develop a photonics R&D capability within UNLV, bringing state-of-the-art lighting technology expertise to the world's largest entertainment venue and providing credentialed professionals to the nation.

From August 1, 2005 through October 31, 2009, the UNLVRF and its partners have specifically focused their talents on (1) improving light emitting diode (LED) technologies; (2) optimizing hybrid solar lighting (HSL), a technology which potentially offers the benefits of blending natural lighting with artificial lighting systems, thus improving energy efficiency and employee productivity; and (3) building a comprehensive academic infrastructure within UNLV which concentrates on photonics R&D, testing and evaluation, thus providing professionals with expertise in state-of-the-art lighting technologies for industries throughout the nation.

Funding for all but one of the tasks that comprise this diverse R&D project ended in September 2008. The R&D work associated with Task 1, LED Research, continued through October 2009. This work included the examination of the electronic structure of nanomaterials for use in LEDs in order to better understand the fundamental principles governing their structure and size, a collaborative effort between UNLV and BU; and a separate UNLV R&D effort focused on developing quantum dot LEDs (QD-LEDs) for improved energy conversion efficiency.

TECHNICAL APPROACH

The project has been organized into three major tasks: (1) LED Research (UNLV and BU's Photonics Center); (2) LED Display Engineering (UNLV's College of Engineering); and (3) Hybrid Solar Lighting (UNLV's Center for Energy Research; ORNL; and Sunlight Direct).

Task 1 – LED Research

This task has been divided into three sub-tasks: (1) Sub-Task 1.1, QDLED Development (UNLV College of Engineering); (2) Sub-Task 1.2, Green LED Research (BU's Photonics Center); and (3) Sub-Task 1.3, Electronic Properties of Nanomaterials for LEDs (UNLV's College of Science).

Sub-Task 1.1 – QDLED Development: UNLV College of Engineering researchers have focused their efforts on developing QDLEDs that will have improved energy conversion efficiency. Unlike traditional LEDS – where the color of the emitted light is determined by the LED materials – the color of QDLED emission is determined by the size of the quantum dots. Thus, multiple color light output can be realized from a single LED by incorporating quantum dots of the same material with different dimensions. Researchers are continuing their investigations under a different Federal funding source.

Sub-Task 1.2 – Green LED Research: BU's Photonics Center researchers have concentrated their efforts on green LED research focused on the Indium Gallium (InGaN) part of the electromagnetic spectrum (EM) in order to better understand why the efficiency of green LEDs is significantly lower than the LEDs emitting in the violet-blue part of the spectrum. The objective is to use this knowledge to fabricate green LEDs with significantly higher efficiency – by at least a factor of two. InGaN-based LEDs and laser diodes (LDs) have great commercial potential because they work in the short wave-length region which has, up to now, been inaccessible for LED technologies. By improving our understanding of these mechanisms, it should be possible to significantly improve the structural design, and with it, the performance of the devices. A detailed final report on BU's research efforts is attached as Appendix A. BU's work is continuing under funding from the Department of Energy's (DOE) Solid State Lighting (SSL) Program.

Sub-Task 1.3 – Electronic Properties of Nanomaterials: Since 2007, BU and UNLV's College of Science researchers have collaborated successfully in studying the electronic properties of LED materials and contacts.. This element of LED research is a sub-task which employs a unique combination of X-ray, electron and optical spectroscopies with microscopic techniques in order to investigate the detailed electronic structure of materials and contacts in LED devices. The team utilizes surface-sensitive photoelectron spectroscopy (with ultraviolet and X-ray excitation) to assess the valence band, inverse photoemission to investigate the conduction band, and a variety of microscopic imaging and spectroscopy techniques. In the framework of this project, the team has established an atomic force microscope to determine surface morphology and a UV-Vis spectrometer to derive the optical band gap. The research team also uses the capabilities of the Advanced Light Source, Lawrence Berkeley National laboratory (ALS-LLBL) to employ a combination of soft X-ray emission/absorption spectroscopy.

Task 2 – LED Display Engineering

The funding received through this award has allowed UNLV's College of Engineering to establish a Display Lighting Laboratory and develop a specialized team of academic researchers, students and industrial partners focused on identifying, developing and implementing engineering solutions for lighting display-related problems. In partnership with private industry, the researchers have developed and tested lighting display technologies from the perspective of quality, durability, energy efficiency and economics. This award has resulted in the development of resources (people and facilities) capable of providing practical solutions to lighting display challenges posed by new technologies. Their primary objective continues to be the further development of a nascent entertainment engineering program to provide a future workforce of skilled and trained engineers for the development and deployment of energy-efficient lighting technology, in partnership with regional, national and international industrial entities.

Variability of quality and performance of LEDs due to the manufacturing process and component aging make LED displays expensive and relatively inefficient. Engineering solutions such as periodic semi-automatic testing of LED groups, using robotic servo-mechanisms for optimum color balance and linearity for best performance, storing cluster dependent data in a memory and using it as a look-up table to drive the pixels individually with variable currents, can cost effectively re-balance an installed LED display due to the low cost of microprocessors and memories. Power management for installed displays is also of interest to the industry. Current displays are not designed for optimized power efficiency, resulting in loss of energy efficiency and increased heat load. Automatic adjustment of the picture characteristics due to ambient parameters, use of more efficient power converters – such as the electronic ballast or other specifically designed power supply – will make the displays more energy efficient, thus reducing the heat being generated.

The primary objective has been achieved through the development of a team of experts from the industry and academia to discuss problems and develop intelligent and inexpensive engineering solutions. Problems are identified based on the needs of industry. Active industrial collaborators during the project's existence have included Macon Gaming, Inc., Las Vegas, NV; Video Walls USA, Inc., Las Vegas, NV; YESCO Electronics, Las Vegas, NV; and Tecnovision, Milan, Italy. Industrial partners have provided in-kind cost-sharing through materials, components and use of testing facilities. The work of this task has continued through Federal funding from DOE's SSL program.

Task 3 – Hybrid Solar Lighting (HSL)

ORNL and UNLV have been teamed to conduct research, development and demonstration related to improving fiber optic systems used in conjunction with HSL technology. Developed at ORNL, HSL technology is licensed to Sunlight Direct, LLC, based in Knoxville, TN. HSL consists of a roof-mounted solar collector which captures sunlight through a bundle of plastic optical fibers designed to illuminate structural interiors through an interior fixture that is both electric and solar. This technology, which has been sporadically funded by DOE, has the potential to provide the benefits of natural lighting without many of the disadvantages of conventional daylighting techniques, significantly increasing energy efficiency and possibly improving employee productivity.

The application of HSL had been limited to only the first or second floor beneath the roof-top collector system due to the high optical loss inherent in the system's plastic optical fibers. Materials with improved solar light distribution capability are presently not economically feasible. This limitation, coupled with the high cost of the installed system, has hindered efforts to conduct a large-scale demonstration of the technology and its associated benefits.

Task 3 was thus focused on extending the system's maximum fiber length from 30 feet to 65 feet while maintaining the current delivered optical flux of 50,000 lumens. This increase in length was achieved by optimizing the design of the system's solar collector components and optical fiber bundle configuration to improve the system's overall collection efficiency.

Development of a low-cost, real-time remote monitoring/control system for each deployed HSL system is also critical to the realization of a reliable HSL technology. The ability to communicate with a deployed HSL tracker allows system improvements, diagnostics and maintenance issues to be quickly and affordably addressed. UNLV's Center for Energy Research was actively engaged in monitoring the demonstration systems installed at UNLV and in collaborating with Sunlight Direct, LLC to improve system operations.

Appendix B provides UNLV's detailed final technical report about this demonstration and monitoring task.

RESULTS AND ACCOMPLISHMENTS

Task 1 – LED Research

Sub-Task 1.1 – QDLEDs: The QDLED development project, originally planned to be executed in three phases, has focused on design and demonstration of QDLEDs fabricated by the all solid state approach during Phase I; the development of high efficiency QDLEDs with effective electrical injection during Phase II; and the development of the technology for a flat panel display, using QDLEDs, during Phase III. During Phase I, the UNLV research team successfully developed stacked five layers of cadmium sulphide (CdS) QDs, separated by thin alumina layers. Such stacked layers of QDs are needed to obtain sufficient optical power to be visible to the naked eye. However, an absence of strong emissions was attributed to the polycrystalline nature of the QDs. This problem, not uncommon for semiconductors, is usually addressed by annealing the QDs. Such annealing needs to be carried out carefully in order not to disturb the layered nature of the structure. A number of samples for thus fabricated and sent to collaborators at BU for experimental determination of the optimum annealing parameters. As work progressed, UNLV developed an effective internal annealing process. Further experimentation with increased annealing temperatures did not result in much improved light emissions from the stacked layers of CdSE QDs. However, the QDs showed significantly improved light emission when they were annealed at 400 C for thirty minutes. It was found that approximately 70% of the CdSE QDs were polycrystalline and only 30% monocrystalline, perhaps explaining the absence of strong optical emissions. UNLV researchers completed a systematic study to optimize the annealing parameters to maximize the light emission efficiency. They also conducted more detailed studies to better understand these results and to improve annealing parameters in order to achieve greater emission efficiencies.

During Phase II, primary research focused on the continuing development of process parameters for synthesis of high quality CdSE QDs with increased concentration of monocrystalline particles. QDs with diameters ranging from 5 nm to 7 nm have been of particular interest for solid state lighting and display applications. However, agglomeration was found to be a major problem for deposition of QDs at elevated temperatures, leading to the assumption that high substrate temperature deposition of QDs is not feasible. Upon further investigation, researchers determined that the deposition temperature can be fine-tuned to achieve increased crystallinity without the agglomeration problem. During the most recent quarter, depositions of CdSE QDs were carried out at different substrate temperatures, ranging from 100 degrees C to 350 degrees C. The samples were then characterized using field emission scanning electron microscopy. Researchers observed that for samples deposited at substrate temperatures above 200^{o}C, there were significant migrations of QDs resulting in agglomerated clusters. This was discouraging since agglomeration will cancel the effects of quantum confinement. Thus, it appears that the substrate temperatures will need to be limited to below 200^{o}C. A number of depositions were carried out during the latter stages of the project in this temperature range; they are currently being characterized using transmission electron microscopy to determine their crystalline structures. Another technique that was investigated during the recent past was post-annealing of the quantum dots deposited at room temperature. For such post-annealing steps, the temperature again needs to be limited to below 400^{o}C to avoid affecting the diode structure. One of the factors affecting such annealing is that the CdSE quantum dots are coated with an insulating layer which might be helpful or detrimental to the annealing process. During the past quarter, post-annealing steps were carried out on CdSE quantum dots at 350^{o}C; the samples are currently being analyzed using scanning electron and transmission electron microscopy.

In summary, UNLV task researchers have:

- Deposited a five-layered QD structure on a LED structure provided by BU researchers
- Developed and optimized an annealing process to improve light emission from QDs; this process will play an important role in improving the efficiencies of QDLED structures
- Effectively annealed QDs on the BU structure
- Developed process parameters for deposition of CdSE QDs, with precise size control
- Developed process parameters for deposition of CdSE QDs which can provide all three - red, green and blue – colors

- Demonstrated improvement in light emission by annealing of CdSE QDs

Significant project delays were incurred due to schedule slippage in the completion of UNLV's new Science and Engineering College (including a state-of-the-art nano-science laboratory). The project was granted a one-year no-cost extension, allowing UNLV researchers to continue their work through October 2009. The work is continuing under another Federal financial assistance award.

Sub-Task 1.2 – Green LED Research: Since the inception of this sub-task, BU researchers have focused on achieving an improved understanding of why the efficiency of green LEDs, based on the InGaN system, is significantly lower than the LEDs emitting in the violet-blue part of the electromagnetic spectrum, and to use this knowledge to fabricate green LEDs with efficiency significantly higher than the current state-of-the-art. The research work accomplished under this task has addressed the fabrication and comparative study of green LEDs, based on InGaN quantum wells and InGaN quantum dots grown by molecular beam epitaxy (MBE). Results of BU's research efforts include:

- An improved understanding about the growth and structure of Indium Nitride and Gallium Nitride QDs, detailed in publications listed in the last paragraph of this final report.

- Growth of InGaN QDs, utilizing the Stranski-Krastanov mode.

- Growth and characterization of blue-green LEDs based on nitride QDs. Two types of LED structures employing III-Nitride QDs, designed to emit in the blue and green, were grown and characterized in bare die configuration. Both structures were designed to have GaN QDs in the nucleation layer.

- Development of a new class of nitride multiple quantum wells, consisting of monolayers of InN wells and thicker GaN barriers.

The results and accomplishments of this sub-task are detailed in numerous published technical journal reports. A detailed final report for this sub-task is also attached as **Appendix A**. The work of Dr. Theodore Moustakas and his research staff at BU's Photonics Center continues under various DOE SSL financial assistance awards.

Sub-Task 1.3 – Electronic Properties of Nanomaterials for LEDs: UNLV's College of Science researchers have established a strong collaboration with BU researchers, using a unique combination of spectroscopic and microscopic techniques to characterize the electronic structure of nanomaterials for use in LEDs. This mutually beneficial collaboration will continue under other financial assistance agreements, and has been a significant strength for both institutions resulting from this award.

The primary focus of research has been on the electronic structure of (Indium, Gallium, Aluminum) Nitride semiconductors and their contacts for numerous applications in optoelectronic devices and other uses (e.g., solar cells and spintronics).

Researchers at BU have used angle-resolved photoelectron spectroscopy (ARPES) to measure the existence of quantum well states in the conduction band of InN due to the confinement of these electrons in an accumulation layer. They then used ARPES to show the existence of an inverted band structure near the valence band maximum, again caused by the confining electron accumulation potential. In order to study the electronic structure away from the surface, and outside the electron accumulation layer, they used bulk sensitive soft X-ray emission and soft X-ray absorption spectroscopies.

UNLV College of Science researchers conducted their experimentation at UNLV and at ALS-LLBL.

A detailed final report for this sub-task is attached as **Appendix B**.

Task 2 – LED Display Engineering

During the course of this project, UNLV College of Engineering researchers developed and implemented a Display Lighting Laboratory and strengthened significantly the collaboration between UNLV and the lighting industrial sector to enhance its nascent entertainment engineering programs.

In summary, UNLV task researchers have, and are continuing, to develop and demonstrate innovative new lighting display techniques based on more efficient lighting technologies. For example, they have:

- Designed a new schematic that has been converted into a printed board and populated by industrial partner, Tecnovision, in a large display (3' x 4'). The project uses UNLV's red-green-blue-white technology developed under this financial assistance award.
- Integrated important features within the board's motor controller, including communication capability between the PC and spectrometer and a receiver and interface within the new color analyzer.
- Advanced the software to drive the motors and acquire data.
- Studied red-green-blue and red-green-blue-white systems for potential energy savings and color perception differences by humans. Over 150 people took part in a human trial of color perception of red-green-blue and red-green-blue-white. Statistical analysis and energy calculations were also completed. Overall, human beings did not perceive any significant difference between same colors produced by the two techniques, RGB and RGBW. An energy savings of 10-30% was observed for the colors studied.
- Demonstrated a powerless display, using Sunlight Direct's HSL concentrator[4], to several interested researchers and industrial representatives.
- Continued R&D collaboration with industry. Tecnovision's President has visited UNLV on several occasions to discuss further joint initiatives, including support for the newly developed LED display.
- Two journal articles, two conference articles, and one Master's thesis (see Appendix C) resulted from this funding.

The R&D work in UNLV's Display Lighting Laboratory continues through funding from DOE's SSL program managed by the National Energy Technology Laboratory.

---

[4] As part of the scope of Task 3, an HSL solar concentrator was installed within the Display Lighting Laboratory for use in developing more efficient lighting displays utilizing renewable energy.

A detailed final report is included in **Appendix C**, a Master of Science in Electrical Engineering thesis, titled “A Novel RGBW Pixel for LED Displays” by Neveen Shlayan.

.

Task 3 – Hybrid Solar Lighting

The Task 3 research team included UNLV, ORNL and Sunlight Direct, LLC, collaborating to research, develop and demonstrate an improved fiber optic system for hybrid solar lighting (HSL), a technology developed by ORNL and commercialized by Sunlight Direct, LLC. HSL is composed of a rooftop-mounted 48-inch diameter collector and secondary mirror that tracks the sun throughout the day. The system focuses the sunlight into 127 optical fibers connected to special light fixtures, equipped with diffusion rods, similar to fluorescent light bulbs. The rods spread light in all directions.[5]

The task funded by this award was focused on extending the system’s maximum fiber length from 30 feet to 65 feet while maintaining the current delivered optical flux of 50,000 lumens in order to extend its lighting capability beyond one-story structures. This increased length was proposed to be achieved by optimizing the design of the system’s solar collector components and optical fiber bundle configuration to improve the system’s overall collection and coupling efficiencies without appreciably affecting the intensity and color of the delivered light.

Three methods for achieving the stated task objective were considered:

- Construct a fused bundle, using low-loss polymer optical (PMMA) 3-mm fibers;
- Use a quartz fiber bundle and transition to low-loss PMMA 3-mm fibers; or
- Use a short version of present fused plastic bundle and transition to large-core, low-los 3 mm fiber (fully cured polymethacrylate) which was used in the original HSL prototypes.

Of these three options, the first was considered the most desirable and was implemented. While the low-loss PMMA is not manufactured in diameters as large as 3 mm, a custom batch of the material was produced and utilized.

Testing of completed demonstration systems was included in the task to evaluate the performance of PMMA fiber at various locations and environments across the United States. In FY 2007, optical fiber testing began and continued for six weeks at three sites: in San Diego, CA, Logan, UT and Oak Ridge, TN. Each site was tested by revolving eight fiber optic bundles to each site. The testing determined that (1) overheating of the acrylic integrating rod was the reason for previous bundle failures; and (2) allowed researchers to establish a safe operating percentage (70%) for the system.

A demonstration unit was installed at the UNLV College of Engineering’s Renewable Energy Center’s campus in late 2007, and included a tracker controller unit. Development of a low-cost, real-time monitoring and control system for each deployed HSL unit is critical to the realization of a reliable HSL technology. The ability to communicate with a deployed HSL tracker allows system improvements, diagnostics and maintenance issues to be quickly and affordably addressed. The tracker controller was modified to allow a server module to act as the interface between the tracker controller and the outside world. This module allows the tracker to be associated with a static IP address that can be remotely accessed. The role of the UNLV research team was to develop and provide electrical interface requirements, install a system,

---

[5] ORNL News Release, “Hybrid solar lighting earns national technology transfer award,” June 1, 2007

collect data and troubleshoot the system. Data were collected and evaluate to determine HLS system performance and benefits.

During late 2007, an HSL demonstration unit was installed and operational at New Horizons Academy in Las Vegas as part of their “Greenest Classroom in Nevada” project. Unveiled on December 10, it was of particular interest to the large audience of community leaders and stakeholders. New Horizons Academy is an educational facility for “learning different” students. The HSL technology is integrated into the classroom both structurally and for learning purposes.

Another HSL demonstration unit was installed at the UNLV College of Engineering’s Display Lighting Laboratory; the collector is being used for developing new energy efficient display lighting technologies, and also for demonstration purposes for students, researchers, and stakeholders.

The results of the UNLV monitoring and tracking sub-task are detailed in the attached final report (Appendix D). In summary, two major issues were observed and noted:

- The tracking unit was noticed to be unstable. No pattern was identified over the times that the system had lost track. At times, loss of tracking resulted in physical damage to the primary mirror.

- The current rods are not the optimal method to disperse light. They are quite dim. A new technique should be modeled to ensure its compatibility with the application in terms of the spatial distribution of light.

SPECIAL RECOGNITIONS, AWARDS AND PATENTS

Oak Ridge National Laboratory, “Excellence in Technology Transfer Award,” recognizing ORNL’s development of hybrid solar lighting technology, presented by Federal Laboratory Consortium for Technology Transfer, June 2007

ORNL, R&D 100 Award, presented by R&D Magazine, recognizing HSL as one of the nation’s most promising technologies, July 2006

PRESENTATIONS

S. Pookpanratana presented a poster on **“Au/Ni contacts on p-type GaN: contact formation investigated with electron and soft x-ray spectroscopies”** at the 7th International Conference on Nitride Semiconductors in Las Vegas, NV, Sept. 19, 2007.

S. Pookpanratana presented a talk on **“Contact formation on GaN investigated with electron and soft x-ray spectroscopies”** at the Materials Research Society Fall 2007 Meeting in Boston, MA.

C. Heske presented an invited talk on “**How soft x-ray spectroscopy can shed light on the electronic and chemical properties of interfaces“**, at the PIRE-ECCI (Partnership for International Research and Education) Seminar, Electron Chemistry and Catalysis at Interfaces, Department of Chemistry and Biochemistry, University of California, Santa Barbara, November 5, 2008.

S. Pookpanratana presented a talk on “**Contact formation on GaN-based semiconductors investigated with electron and soft x-ray spectroscopies”** at the Spring 2009 Materials Research Society on April 15, 2009 in San Francisco, CA.

S. Pookpanratana presented a talk on **"Impact of oxygen-annealing on the morphology and chemical properties of Au/Ni contacts on p-GaN"** at the Spring 2009 European Materials Research Society on June 11, 2009 in Strasbourg, France.

MAJOR PUBLICATIONS

Tao Xu, L. Zhou, Y. Wang, A. Ozcan, K. F. Ludwig, D. J. Smith and T. D. Moustakas, **"GaN quantum dot superlattices by Molecular Beam Epitaxy at high temperatures"** Journal of Appl. Phys. **102,** 073517 (2007).

Tao Xu, A. Nikiforov, R. France, C. Thomidis, A. Williams and T. D. Moustakas, "**Blue-green-red LEDs based on InGaN quantum dots grown by plasma-assisted molecular beam epitaxy"** Phys. Stat. Sol. (a) Vol. 206, No.6, 2098 (2007)

J. Abell and T. D. Moustakas, **"The role of dislocations as non-radiative recombination centers in InGaN quantum wells"**, Appl. Phys. Lett. **92**, 091901(2008).

E. Dimakis, A. Yu. Nikiforov, C. Thomidis, L. Zhou, D. J. Smith, J. Abell, C. –K. Kao, T. D. Moustakas, **"Growth and properties of near-UV light emitting diodes based on InN/GaN quantum wells"**, Phys. Stat. Sol. (a) **205**, No. 5, 1070 (2008)

C. Thomidis, A. Yu. Nikiforov, T. Xu, T. D. Moustakas, **"InGaN-based LEDs grown by plasma-assisted MBE on (0001) sapphire with GaN QDs in the nucleation layer"**, Phys. Stat. Sol. (c) **5**, No. 6, 2309 (2008)

Tao Xu and T. D. Moustakas, **"Growth and Characterization of III-Nitride Quantum Dots and their Applications to Emitters"** *in Self-Assembled Quantum Dots,* Edited by Zhiming M. Wang (Spring 2008), Chapter 15

S. Pookpanratana, R. France, M. Bar, L. Weinhart, O. Fuchs, M. Blum, W. Yang, J.D. Denlinger, T.D. Moustakas and C. Heske, **"Intermixing and chemical structure at the interface between n-GaN and V-based contacts,"** Appl. Phys. Lett., Vol. 93, 2008, pp. 172106

N. Shlayan, R. Venkat, P. Ginobbi, A. Singh**, "Energy efficient RGBW pixel configuration for light-emitting display,"** Journal of Display Technology, Volume: 5, Issue: 11, pp. 418-424 (2009)

N. Shlayan, R. Venkat, P. Ginobbi, G. Mercier, **"A novel RGBW pixel for LED displays,"** Systems Science, Vol. 35, No.2, pp. 95-99 (2009)

Appendix A

Detailed Final Report
Task 1.2, BU, “Green Led Research”

Final Scientific/Technical Report

Project Title:	Photonics Research and Development Task 1.2 Green LED Research
Project Period:	10/01/05 to 07/31/08
Date of Report:	10/10/08
Recipient:	Boston University
Award Number:	Subcontract #RF-06-PRD-001
Working partners:	UNLV
Cost-Sharing Partners:	none
Contact:	**PI:** Theodore D. Moustakas Tel. No: 617-353-5431 Moustakas@bu.edu

I. Project Objectives: The basic objective of this task (Green LED Research) is to understand why the efficiency of green LEDs, based on the InGaN system, is significantly lower than the LEDs emitting in the violet-blue part of the electromagnetic spectrum and to use this knowledge to fabricate green LEDs with efficiency significantly higher than the current state-of-the art. The proposed work addresses the fabrication and comparative study of green LEDs based on InGaN quantum wells and InGaN quantum dots grown by molecular beam epitaxy (MBE). The two main objectives of this project are:

- Material studies of the InGaN system, which includes the development of quantum dots (QDs) based Nitride semiconductors
- Fabrication and characterization of blue-green LEDs using InGaN QDs.

II. Background: The production of white light using LEDs for displays and general light illumination can be accomplished by direct mixing of the three primary colors (red, green and blue) or by indirect processes involving ultra-violet LEDs and tri-colored phosphor or blue LEDs and yellow phosphor. However, to meet the DOE's goals of 200 lm / W and Color Rendering Index (CRI) more than 90 % by the year 2020, the direct mixing of primary colors or the process involving a near UV LED and a tricolor phosphor are the methods of preference. Red LEDs are usually made out of the AlGaInP system, while the blue and green LEDs are currently made from the InGaN system. It has however been observed that the green LEDs are significantly less efficient than the violet, blue and red LEDs (5% vs. 50%). The exact mechanism of reduction in the efficiency of green LEDs has not been understood. Some of the reasons are the high dislocation density as well as alloy phenomena such as phase separation and partial atomic ordering, which are common problems in InGaN alloys. In the following we summarize our progress towards the objectives stated in the previous section.

III. Development of blue-green LEDs using III-nitride quantum dots

1. Introduction: LEDs emitting in the violet-blue-green parts of the electromagnetic spectrum are based on InGaN multiple quantum wells (MQWs). The internal quantum efficiency (IQE) of such devices decreases as the InN mole fraction in the InGaN wells increases, a result that has not been fully understood. Alloy phenomena and/or strong piezoelectric fields across the QWs could possibly contribute to this decrease in IQE.

Alloy phenomena such as spinodal decomposition driven phase separation [1,2] lead to compositional inhomogeneities and the resulting potential fluctuations have been thought to be beneficial to emission by LEDs due to localization of excitons [3]. However, III-Nitride alloys were also found to undergo partial atomic ordering [4-6], and this was thought to be undesirable to LED performance, because electron-hole pairs tend to separate in the ordered and random domains and this minimizes the efficiency of spontaneous radiative recombination [7]. Theoretical calculations by Dudiy and Zunger [8] on partially ordered $Al_xGa_{1-x}N$ indicate that the energy band alignment between random and ordered domains changes from Type I to Type II heterostructures for $x \sim 0.4$. This leads to an increase by two to three orders of magnitude in the radiative lifetimes of injected e-h pairs. Although such studies have not been reported in InGaN alloys one expects qualitatively a similar behaviour. Thus, the spontaneous radiative lifetime is expected to increase with the increase in InN mole fraction.

The role of the piezoelectric fields across the QWs in influencing the performance of InGaN LEDs has also been addressed by a number of authors [9, 10]. In particular, since the strength of the piezoelectric fields across the InGaN QWs increases as the InN mole fraction increases.

An alternative approach is to use InGaN quantum dots (QDs) instead of QWs as the active region of the LED. In such LED structures exciton localization occurs by 3D quantum confinement rather than by potential fluctuations due to compositional inhomogeneities. This is because the density of states of QDs has delta-function energy dependence. Of course electron confinement in all three dimensions requires that the lateral dimensions of the QDs are equal or smaller than the de Broglie wavelength of electrons. In such small structures phase separation and partial atomic ordering are not likely to occur. However, piezoelectric fields are likely to be as important in the case of QDs as in QWs. For this reason the QDs must be 1 to 2 nm in average size to minimize the quantum confined Stark effect (QCSE).

In this report we summarize our progress in the fabrication and characterization of III-Nitride QDs and their application to blue-green LEDs. In particular we discuss the problems with the current generation QDs and what improvements in the growth and microstructure are required to lead to more efficient LEDs than those based on quantum wells.

2. Experimental methods: The InN, GaN and InGaN QDs were grown by rf plasma-assisted MBE using the Varian Gen II MBE system. Ga, Al and In were evaporated from standard effusion cells and the molecular nitrogen was activated in an EPI rf plasma source. The plasma power was kept at 300 W and the nitrogen flow rate was 1.0 sccm. In all cases c-plane sapphire substrates were used, which led to InN, GaN and InGaN QDs having the [0001] orientation. The sapphire substrates were first subjected to nitridation at 870 ˚C for approximately 1 h, followed by the deposition of a 60-300-

nm thick AlN film grown at the same temperature under Al-rich conditions of growth. These nucleation steps lead to group-III polar growth on c-sapphire substrates. The specific growth conditions of the three types of QDs investigated are described in Section III.3.

The surface dot density and height distribution were evaluated using Atomic Force Microscopy (AFM). The structure and microstructure of the dots was determined by transmission electron microscopy (TEM). Observations were made in both plan-view and cross-section geometries with a JEM-4000EX high-resolution electron microscope.

3. Results and discussion:

In this section we discuss the growth and characterization of InN, GaN and InGaN QDs as well as our initial efforts to incorporate such QDs in blue –green LEDs.

InN Quantum Dots: Details on the growth and structure of InN QDs were published elsewhere [11] and in here we only review the most important findings. Following the deposition of 60 nm AlN as described in the previous section, a 500-nm thick Ga-polar GaN film was grown at 770 ˚C under slightly Ga-rich conditions. Standard **g.b** diffraction contrast analysis revealed that dislocations of either edge or mixed (edge-screw) type were the primary threading defects present in this relatively thin GaN buffer layer. Plan-view observations revealed that the dislocation densities were typically in the range of 2-5x10^{10}/cm^2. The InN QDs were deposited at substrate temperature of 425 ˚C. The relatively low temperature was chosen primarily because of the low decomposition temperature of In-polar InN. The typical equivalent growth rate for InN deposition was ~0.05 nm/s. A total equivalent coverage of approximately nine InN monolayers [where one monolayer (ML) ~0.285 nm] was used during the deposition of the InN QDs. The sample was annealed for 5 mins at the growth temperature under N-atmosphere before cooling down.

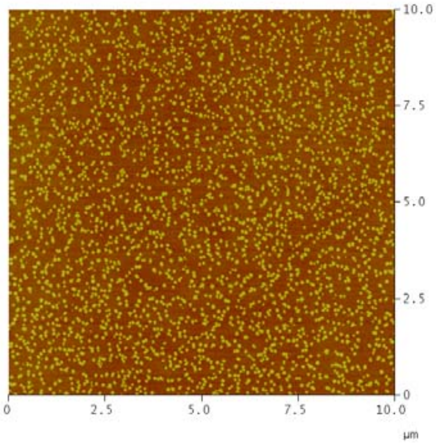

Figure 1: AFM image showing distribution of InN QDs grown on a Ga-polar GaN template.

Figure 1 shows a typical panorama showing the apparently random distribution of the InN QDs. From these data we calculated the quantum dot density to be ~2x10^9/cm^2 and the mean diameter and height dimensions were 115 and 15 nm respectively.

Both *in-situ* reflection high energy electron diffraction (RHEED) and *ex-situ* transmission electron microscopy show no evidence of InN wetting layer, a result consistent with the large lattice mismatch

(11%) between GaN and InN. Examination by electron microscopy indicates that almost all of the InN islands have nucleated directly above threading dislocations present in the GaN buffer. Detailed examination at higher magnifications indicates that the InN QDs have the wurtzite crystal structure and that the QDs also maintained a well defined epitaxial relationship with the underlying GaN buffer layer. Periodic arrays of moiré fringes with spacings of ~ 2.8 nm were visible along the InN QD/ GaN buffer layer interface, as would be expected for perfect InN/GaN heteroepitaxy. This periodicity also corresponds to the spacings between the misfit dislocations that would accommodate the lattice mismatch between the two materials. This is an indication that the InN QDs are completely relaxed.

GaN Quantum Dots: Details on the growth and characterization of GaN QDs were published elsewhere [12] and in here we summarize the most important findings. After the deposition of 300 nm AlN on the substrate at 870 ˚C the substrate temperature was then reduced to 770 ˚C for the deposition of GaN QDs or QD superlattice consisting of GaN QDs separated by 10-20 nm AlN barriers. The growth rate of the GaN QDs was about 0.3 ML/s. The GaN QDs were grown in the modified Stranski-Krastanov growth mode [13, 14]. In this mode several MLs of GaN were deposited under Ga-rich conditions (Ga/N ~ 1.1), followed by evaporation of the excess Ga in vacuum. During this stage the deposited GaN film undergoes 2D to 3D transition as indicated by the conversion of the RHEED pattern from streaky to spotty.

Figure 2 shows a high resolution TEM image of two GaN QDs at the last layer of a QD superlattice, consisting of four periods of GaN/AlN. The GaN QDs were obtained using 5 ML of GaN coverage, and the QDs are separated by 18 nm AlN barriers. From this electron micrograph we estimate that the height of the QDs is about 4 nm and that the dot diameter is about 15 nm. The QDs in the free surface have truncated pyramidal shapes, faceted along the {1-103} planes. A continuous 2D wetting layer with a thickness of about 2-2.5 ML was identified from these studies. These findings agree with other published results [15]

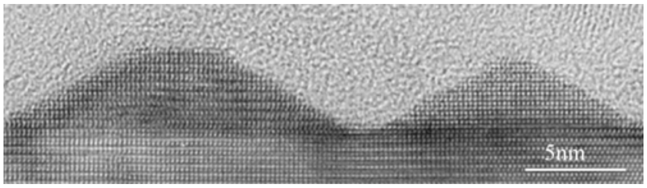

Figure 2: High resolution TEM image of GaN QDs on the surface of a 4 period GaN/AlN QD superlattice.

The surface morphology of this GaN quantum dot superlattice (QDSL) is shown in the AFM image of Figure 3. The QD density on the top surface of this QD superlattice was measured to be $9x10^{10}cm^{-2}$.

The height distributions of the surface GaN QDs for samples produced with different GaN coverage are shown in Figure 4. Thus, the height of the GaN QDs has a bimodal distribution. Mode 1 has a narrow Gaussian distribution with an average height of 1.4-1.8 nm and full width at half maximum of 0.8 to 0.9 nm. Mode 2 has a broader distribution with an average height of about 3.6 nm and FWHM of 2 nm. As the GaN coverage increases, mode 2 becomes the dominant one. When the coverage is more than 5 ML, the height distribution becomes practically Gaussian with an average height of about 3.4

nm and FWHM of 1.8-1.9 nm. The height of mode 2 dots did not increase with increasing coverage, which was different from that reported for GaN QDs grown under N-rich conditions [16].

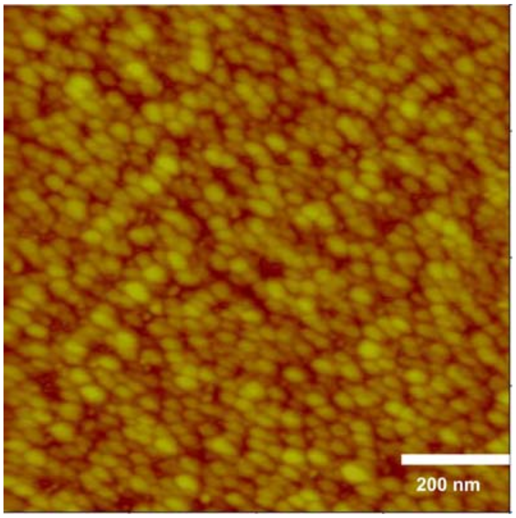

Figure 3: AFM height image of a GaN QDSL with four stacks of QDs and 5 ML GaN coverage in each stack (z scale is 10 nm).

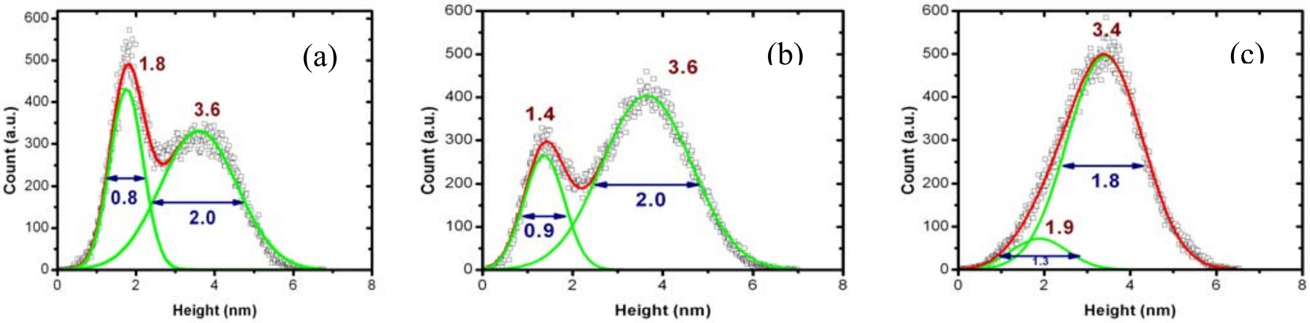

Figure 4: AFM height distribution for GaN QDs grown with (a) 3, (b) 4, and (c) 5 ML GaN coverage, respectively.

Bright-field plan-view TEM images were used to determine the density of dislocations with edge components as well as to access any correlation between dislocations and QDs. Figure 5 shows an image of the GaN QDSL sample with 30 GaN stacks. The patches of faint dark contrast correspond to the GaN QDs, while the small dark spots correspond to dislocations having edge components. As shown in this image, some GaN QDs are associated with threading dislocations while other QDs appear to be located in areas that are free of dislocations. Moreover, the GaN QDs associated with dislocations sometimes appear to have a larger diameter than QDs in dislocation free regions. These results are in agreement with previous reports [17].

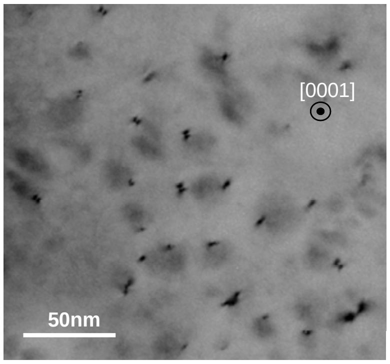

Figure 5: Bright-field plan-view TEM image of GaN QDSL sample with 30 GaN stacks

To further investigate the origin of the bimodal distribution we have also studied the GaN QD height distribution as a function of the periods of the QDSL. The height distribution for the QDs on the top layer of three GaN/AlN QDSL samples with 1, 4 and 30 stacks is shown in Figure 6. Again, the height of the GaN QDs has a bimodal distribution. However, mode 1 becomes the dominant one as the number of stacks increases. In fact the density of mode 1 QDs remains the same while the mode 2 QDs decreases with the number of stacks. This result is also consistent with the association of the larger QDs with threading dislocations since it is known that threading dislocations annihilate as the number of stacks increases [12].

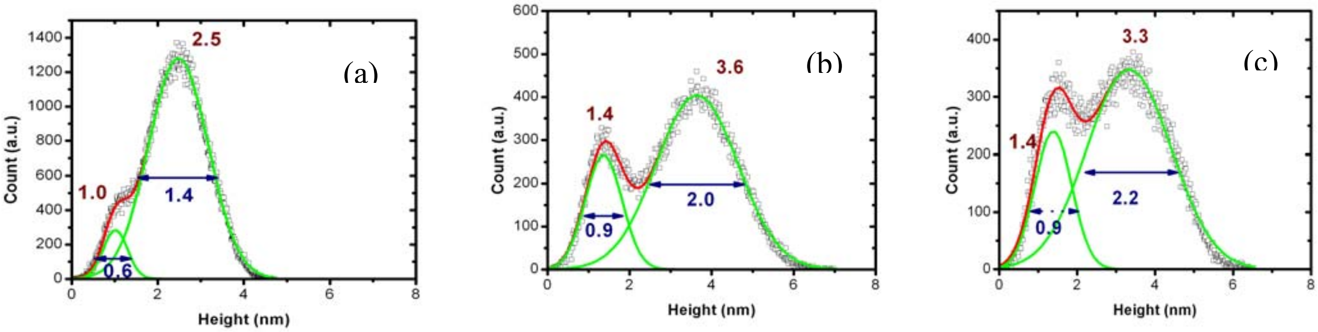

Figure 6: Height distribution of GaN/AlN QDSL samples for different number of stacks and the same GaN coverage (4 ML) in each stack. (a) 1 stack, (b) 4 stacks, and (c) 30 stacks [12].

This bimodal height distribution of GaN QDs grown heteroepitaxially on highly dislocated nitride templates is undesirable for the use of GaN QDs in a number of applications.

<u>InGaN Quantum Dots:</u> The InGaN QDs were grown at 520 to 580 ˚C on 500 nm Ga-polar MBE grown GaN templates. The self-assembled InGaN QDs were grown in the Stranski-Krastanov growth mode. In this mode, several MLs of InGaN were deposited under N-rich conditions. After the thickness of the deposited InGaN exceeds the critical thickness we have observed the 2D to 3D transition by RHEED. At that stage the QD layer was left in vacuum for 1 min before the sample was cooled to room temperature. The dependence of the size distribution and emission properties of these InGaN QDs were reported previously [18]. Figure 7 shows a typical AFM image of an InGaN QD sample grown at 520 ˚C with equal fluxes of Ga and In and 12 ML InGaN coverage. The average dot height and diameter are 3 nm and 30 nm respectively and the dot density is 7×10^{10} cm^{-2}.

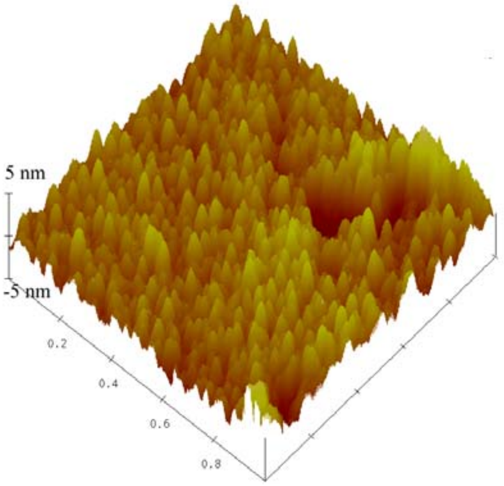

Figure 7: AFM image of an InGaN QD sample grown under the conditions described in the text.

In addition to single InGaN QDs we have also deposited InGaN/ GaN multiple quantum dots (MQDs) at the same temperature. It contains ten stacks of InGaN QDs, each layer with 12 ML InGaN coverage.

The composition and thicknesses of the InGaN QDs and GaN barriers were determined by XRD to be 43% InN mole fraction and 4 and 6 nm respectively. The emission properties of these InGaN QDs and MQDs were investigated by cathodoluminescence measurements at room temperature. Specifically, the single InGaN QDs were investigated at 3 KV accelerating voltage, while the InGaN/GaN MQDs were investigated at 13 KV accelerating voltage. The results are shown in Figure 8.

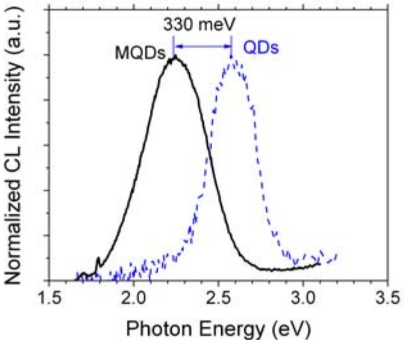

Figure 8: Room temperature CL emission of a single layer of InGaN QDs (blue) and an InGaN/GaN MQD sample with identical InGaN QDs [17].

We note that the emission spectra from the single layer of InGaN QDs have its peak at 2.58 eV and a FWHM of 308 meV, while that of the MQD have a peak at 2.25 eV and FWHM of 415 meV. Thus, the spectra of the MQDs have been red shifted by 330 meV and broadened by 107 meV. The relatively broad emission spectra suggest a rather broad size distribution of InGaN QDs. We speculate that the significant red shift of the emission spectra of the MQDs is consistent with strong QCSE since the InGaN QDs in the MQD structure are subjected to greater strain from the GaN barriers. We came to this conclusion since the dots in successive layers are spatially correlated [12]. In other words the QDs in the new layer tend to nucleate directly above the buried QDs. This spatial bias is attributed to the strain in the surface of the new barrier due to the buried strained QDs [19-23]. Indeed, Gogneau et al. reported that in GaN /AlN QD superlattices both the in plain strain of the AlN barriers as well as the elastic relaxation of the GaN QDs depend on the number of stacks [24].

Blue-Green LEDs based on Nitride QDs: Two types of LED structures employing III-Nitride QDs, designed to emit in the blue and green, were grown and characterized in bare die configuration. Both structures were designed to have GaN QDs in the nucleation layer, which was shown to filter threading dislocations [25]. The blue LED has an active region consisting of 3 $In_{0.18}Ga_{0.82}N$/GaN MQWs. The active regions of the green LED is made of 5 periods of InGaN/GaN MQDs with the InGaN composition of 41%. The InGaN QD layer height and barrier thickness are 4 nm and 6 nm respectively. A schematic of the cross-section structure of the two LEDs and photographs of the two devices upon injection with 50 mA current are shown in Figure 9.

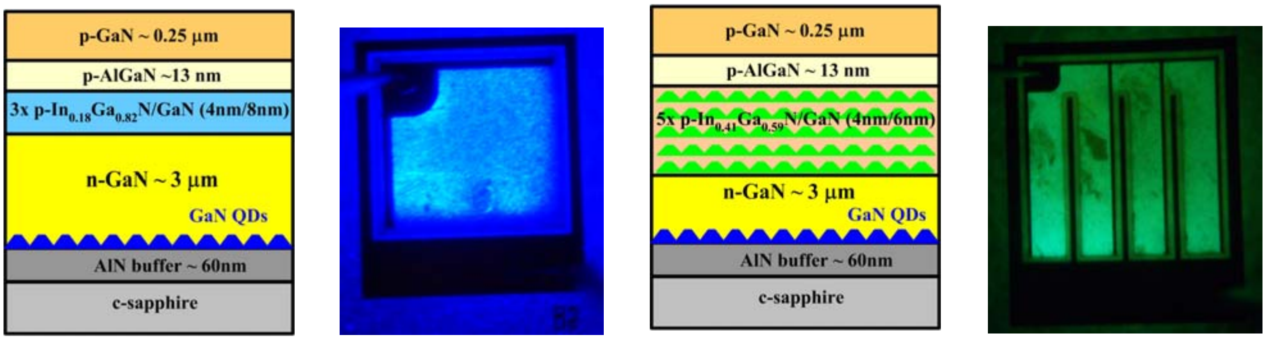

(a) (b) (c) (d)

Figure 9: (a) Schematic of an LED with GaN QDs in the nucleation layer and three InGaN/GaN MQWs in the active region. (b) A photograph of the LED structure shown in (a) upon injection with 50 mA current. (c) Schematic of an LED with InGaN QDs in the nucleation layer and five periods of InGaN/GaN QDs in the active region. (d) A photograph of the LED structure shown in (c) upon injection with 50 mA current. The mesa dimensions of both devices are 800 μm x 800 μm.

At low injection current the peak emission from the blue LED occurs at 440 nm while that of the green LED occurs at 560 nm. In both of these devices the emission spectra are blue shifted with increase in the injection current. However, the blue shift is even stronger for the green LED due to the stronger QCSE resulting from the relative large size of the QDs.

IV. Development of near UV LEDs based on monolayer InN / GaN MQWs

During this project we also developed a new class of nitride multiple quantum wells consisting of monolayers (ML) of InN wells and thicker GaN barriers. The investigated MQW structures were grown onto C-plane GaN templates. A cross section TEM picture of one such MQW structure and the corresponding photoluminescence spectra are shown in Figure 10.

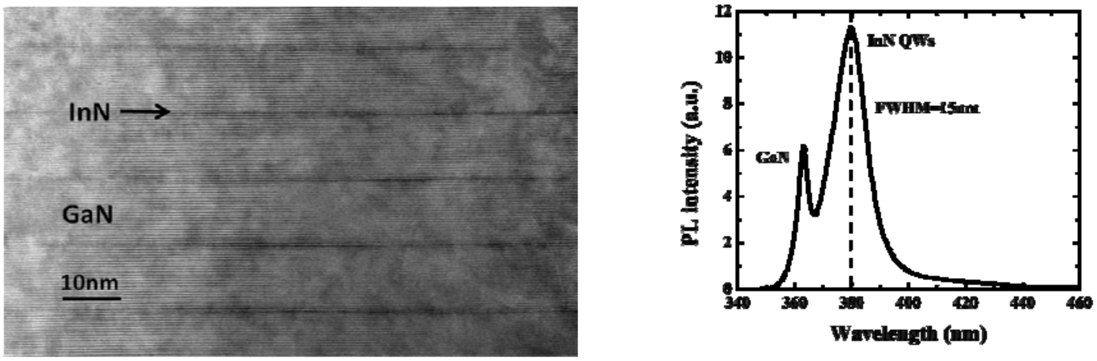

(a) (b)

Figure 10. (a) XTEM micrograph of a structure consisting of five InN/GaN QWs. The thickness is 1 ML for the InN wells and 11 nm for the GaN barriers. The InN layers are continuous and characterized by well defined interfaces and uniform thickness. (b) Room temperature PL spectrum of a structure consisting of five InN/GaN QWs. The emission from the QWs peaks at 380nm, i.e. in the near-ultraviolet spectral region. The low intensity peak at 363 nm corresponds to optical transitions in the GaN template.

The InN/GaN MQWs described in Figure 10 were used as the active region of LEDs with emission in the near UV spectral region (~380nm). As mentioned in Section II, these LEDs are suitable for the excitation of tri-color phosphor for the generation of white light.

For the LED structure presented here, the active region consisted of fifteen InN/GaN QWs. The InN QW thickness was 1 ML, while the GaN barrier thickness was 5 nm. In addition, four equally spaced 12.5 nm thick intermediate GaN barriers were employed to relief the average built-in misfit strain in the active region and prevent the lattice relaxation through the formation of dislocations. The active region was grown on n-type (10^{18}-10^{19} cm^{-3}) GaN template and capped by a 10 nm thick Mg-doped $Al_{0.1}Ga_{0.9}N$ electron blocking layer and, subsequently, by a 300 nm thick Mg-doped GaN layer. The hole concentration is estimated to be 10^{17}-10^{18} cm^{-3} for the p-type $Al_{0.1}Ga_{0.9}N$ layer and 10^{18} cm^{-3} for the p-type GaN layer. The active region was grown at 685 ^{o}C, while the subsequent p-type layers were grown under extreme Ga-rich conditions at 750 ^{o}C. Large excess of Ga flux during the growth of Mg-doped GaN has been shown to increase the incorporation of Mg in the GaN crystal [26].

For the fabrication of the LED, 300 × 300 μm^2 square mesas were formed by inductively coupled plasma (ICP) etching, using chlorine (Cl_2) gas. Ohmic contacts, consisting of V (15 nm)/Al (80 nm)/V

(20 nm)/Au (100 nm) [27], were deposited by e-beam evaporation on the n-type GaN, while Ni (4 nm)/Au (1 nm) contacts were deposited on the p-type GaN.

The room temperature EL spectra of the LED, for injection currents from 20 to 200 mA, are shown in Figure 11 (a). The EL spectra consist of a single peak at 384 nm, which corresponds to emission from the QWs, with FWHM as low as 14 nm for an injection current of 200 mA. Furthermore, the peak wavelength of the EL emission is independent of the injection current. This is indicative of the absence of the quantum confined Stark effect (QCSE) in the 1 ML thick InN/GaN LEDs. Besides, the presence of polarization field in 1 ML thick QWs is not expected to affect substantially the overlap of the wavefunctions of electrons and holes.

The output optical power was measured in a bare die configuration at 300 K as a function of the injection current and the results are plotted in Figure 11 (b). As it is indicated by the dashed line, the output power is linearly dependent on the current and equals to 0.84 mW at 200 mA. These results have recently been published in reference [28].

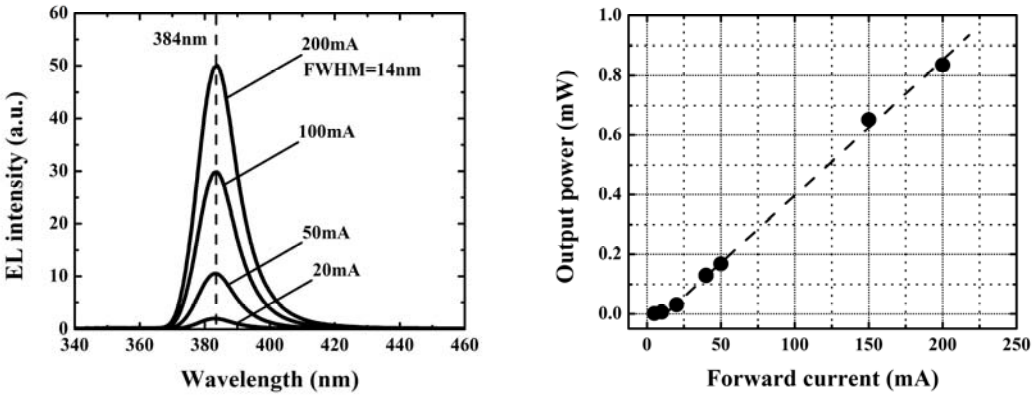

(a) (b)

Figure 11. (a) Room temperature EL spectra of an LED, consisting of fifteen InN/GaN QWs, for various injection currents. The peak emission is located at 384 nm and is independent of the injection current, indicating in that way the absence of the quantum confined Stark effect in the LED. (b) Output optical power of the device shown in Fig. 10, as measured in a bare die configuration, for various injection currents. The output power increases linearly with the injection current and equals to 0.84 mW at 200 mA

V. Soft X-Ray Spectroscopic Studies of the Surface and Bulk Electronic Structure of Wide Band Gap Nitride Semiconductors (Professor Kevin Smith at BU)

Nitride semiconductors are the focus of intense scientific scrutiny due to their numerous potential applications in optoelectronic devices, solar cells, and spintronics. However, our understanding of the basic physics and chemistry of these materials lags far behind our ability to make electronic devices from them. If nitride semiconductors are to achieve their full technological potential then we must have as deep an understanding of their *fundamental* properties as exists for Si and III-V electronic materials. The subcontract in Professor Smith's group covered a program aimed at understanding the electronic structure of clean and adsorbate-covered nitride semiconductors. The materials were studied using a powerful combination of synchrotron radiation-based spectroscopies that include soft x-ray emission, resonant inelastic x-ray scattering, core and valence band photoemission, and soft x-ray absorption. The samples were synthesized using plasma assisted molecular beam epitaxy by a team led by Professor Ted Moustakas from Boston University.

The main focus of our research during the funded period was on the electronic structure of InN. We previously used angle resolved photoemission spectroscopy (ARPES) to measure the existence of quantum well states in the conduction band of InN due to the confinement of these electrons in an accumulation layer. We then used ARPES to show the existence of an inverted band structure near the valence band maximum, again caused by the confining electron accumulation potential. In order to study the electronic structure away from the surface, and outside the electron accumulation layer, we used bulk sensitive soft x-ray emission and soft x-ray absorption spectroscopies, and measured the valence and conduction band densities of states. These studies lead to two manuscripts:

1. **"Electronic Structure of InN Studied Using Soft X-ray Emission, Soft X-ray Absorption, and Quasiparticle Band Structure Calculations"**
   L.F.J. Piper, L. Colakerol, T. Learmonth, K.E. Smith, F. Fuchs, J. Furthmüller, F. Bechstedt, T.C. Chen, T.D. Moustakas, and J.H. Guo, Phys. Rev. B **76**, 245204 (2007)

2. **"Observation of an Inverted Band Structure near the Surface of Indium Nitride."**
   L. Colakerol, L.F.J. Piper, A. Fedorov, T.C. Chen, T.D. Moustakas, and K.E. Smith, Phys. Rev. Lett. (*submitted*).

one invited talk:

1. **"Observation of Intrinsic Quantum Well States in InN",** Presented at
   17th International Vacuum Congress, Stockholm, Sweden; (July 5th, 2007)

and two contributed talks:

1. **"Observation of Intrinsic Quantum Well States in InN",** Presented at
   15th Vacuum Ultraviolet Conference, Berlin, Germany; (August 5th, 2007)

2. **"Observation of Intrinsic Quantum Well States in InN"**, Presented at
2007 AVS National Symposium, Seattle, WA; (October 15, 2007)

VI. Patents: No patent applications filed

VII. Publications

- Tao Xu, L. Zhou, Y. Wang, A. Ozcan, K. F. Ludwig, D. J. Smith and T. D. Moustakas, **“GaN quantum dot superlattices by Molecular Beam Epitaxy at high temperatures”** Journal of Appl. Phys. **102,** 073517 (2007).

- Tao Xu, A. Nikiforov, R. France, C. Thomidis, A. Williams and T. D. Moustakas, “**Blue-green-red LEDs based on InGaN quantum dots grown by plasma-assisted molecular beam epitaxy”** Phys. Stat. Sol. (a) Vol. 206, No.6, 2098 (2007)

- J. Abell and T. D. Moustakas, **“The role of dislocations as non-radiative recombination centers in InGaN quantum wells”**, Appl. Phys. Lett. **92**, 091901 (2008).

- E. Dimakis, A. Yu. Nikiforov, C. Thomidis, L. Zhou, D. J. Smith, J. Abell, C. –K. Kao, T. D. Moustakas, **“Growth and properties of near-UV light emitting diodes based on InN/GaN quantum wells”**, Phys. Stat. Sol. (a) **205**, No. 5, 1070 (2008)

- C. Thomidis, A. Yu. Nikiforov, T. Xu, T. D. Moustakas, **“InGaN-based LEDs grown by plasma-assisted MBE on (0001) sapphire with GaN QDs in the nucleation layer”**, Phys. Stat. Sol. (c) **5**, No. 6, 2309 (2008)

- Tao Xu and Theodore D. Moustakas, **“Growth and Characterization of III-Nitride Quantum Dots and their Applications to Emitters”** *in Self-Assembled Quantum Dots,* Edited by Zhiming M. Wang (Springer 2008), Chapter 15

VIII. Presentations

- “**Blue-green InGaN/GaN LEDs using quantum dots (QDs) grown by plasma-assisted molecular beam epitaxy (MBE)**”, Tao Xu, Jasper S. Cabalu, Alvin G. Stern, Wei Li, Ryan France, Adrian Williams and T. D. Moustakas. Presented at the Materials Research Society Meeting (Boston, Nov. 28 to Dec. 2, 2005). Best Poster Award Nomination.

- **“Growth of InGaN Alloys with High Indium Concentration by plasma-assisted MBE”,** Joshua Abell, Papo Chen, T.D. Moustakas, presented at MRS Fall meeting, (Boston, Dec. 2005).

- “**Physics of Textured III-Nitride Quantum Wells for Applications to LEDs”,** T. D. Moustakas, International Semiconductor Device Research Symposium (Invited presentation-Washington Dec. 7-9, 2005).

- **“Blue-green-red LEDs based on InGaN QDs”** T. Xu and T.D. Moustakas. Presented in the International Workshop on Nitride Semiconductors in Kyoto, Japan on October 2006.

- **"InGaN-based LEDs grown by plasma-assisted MBE on (0001) sapphire with GaN QDs in the nucleation layer"** C. Thomidis*, A. Yu. Nikiforov, Tao Xu, and Theodore D. Moustakas**,** Presented at the 7th International Nitride Semiconductor Conference in Las Vegas (Sept. 16 to 21, 2007).

References

[1] I. Ho and G. B. Stringfellow, Appl. Phys. Lett. **69,** 2701 (1996)

[2] R. Singh, D. Doppalapudi, T.D. Moustakas and L.T. Romano, Appl. Phys. Lett. **70,** 1089 (1997)

[3] S. F. Chichibu, T. Azuhata, T. Sota and S. Nakamura, Appl. Phys. Lett. **70,** 2822 (1997)

[4] D. Korakakis K. F. Ludwig and T. D. Moustakas, Appl. Phys. Lett., **71,** 72 (1997)

[5] D. Doppalapudi, S.N. Basu, K.F. Ludwig and T. D. Moustakas J. Appl. Phys. **84**, 1389 (1998)

[6] D. Doppalapudi, S.N. Basu and T.D. Moustakas. J. Appl. Phys., **85**, 883 (1999)

[7] M. Misra, D. Korakakis, H.M. Ng and T.D. Moustakas. Appl. Phys. Lett. **74**, 2203 (1999)

[8] S. V. Dudiy and Alex Zunger, Appl. Phys. Lett. **84,** 1874 (2004)

[9] A. Bell, J. Christen, F. Bertram, F. A. Ponce, H. Marui and S. Tanaka, Appl. Phys. Lett. **84,** 58 (2004)

[10] I. H. Brown, I. A. Pope, P. M. Smowton, J. D. Thomson, W. W. Chow and D. P. Bour, Appl. Phys. Lett. **86,** 131108 (2005)

[11] L. Zhou, Tao Xu, D. J. Smith, and T. D. Moustakas, Appl. Phys. Lett., 231906, **88** (2006)

[12] Tao Xu, Lin Zhou, Yiyi Wang, Ahmet S. Ozcan, K. F. Ludwig, David Smith and T. D. Moustakas, J. Appl. Phys. **102,** 073517 (2007).

[13] N. Gogneau, D. Jalabert, E. Monroy, T. Tanaka, and B. Daudin, J. Appl. Phys. **94,** 2254 (2003).

[14] J. Brown, F. Wu, P. M. Petroff, and J.S. Speck, Appl. Phys. Lett. **84,** 690 (2004).

[15] E. Sterigiannidou, E. Monroy, B. Daudin, J. L. Rouviere, and A. D. Andreev, Appl. Phys. Lett. **87,** 203112 (2005)

[16] C. Adelmann, B. Daudin, R. A. Oliver, G.A. D. Briggs, and R. E. Rudd, Phys. Rev. B **70,** 125427 (2004).

[17] J. L. Rouviere, J. Simon, N. Pelekanos, B. Daudin and G. Feuillet, Appl. Phys. Lett. **75,** 2632 (1999)

[18] Tao Xu, A. Nikiforov, R. France, C. Thomidis, A. Williams and T. D. Moustakas, Physica Status Solidi (a) **204**, No. 6, 2098 (2007)

[19] D. J. Eaglsham and M. Cerullo, Phys. Rev. Lett. **64,** 1943 (1990).

[20] F. K. LeGoues, M. Copel and R. M. Tromp, Phys. Rev. Lett. **63,** 1826 (1989)

[21] T. S. Kuan and S.S. Iyer, Appl. Phys. Lett. **59,** 2242 (1991)

[22] J. Y . Yao, T. G. Anderson and G.L. Dunlop, J. Appl. Phys. **69,** 2224 (1991)

[23] J. Tersoff, C. Teichert and M. G. Lagally, Phys. Rev. Lett. **76,** 1675 (1996)

[24] N. Gogneau, F. Fossard, E. Monroy, S. Monnoye, H. Mank and B. Daudin

[25] Tao Xu , A. Yu Nikiforov, C. Thomidis, R. France, A. Williams, W. Li, T. D. Moustakas, L. Zhou and D. J. Smith (To be published).

[26] A. Bhattacharyya, W. Li, J. Cabalu, T. D. Moustakas, D. J. Smith, R. L. Hervig, Appl. Phys. Lett. 85, No. 21, 4956 (2004).

[27] R. France, T. Xu, P. Chen, R. Chandrasekaran, T. D. Moustakas, Appl. Phys. Lett. 90, 062115 (2007).

[28] E. Dimakis, A. Yu. Nikiforov, C. Thomidis, L. Zhou, D. J. Smith, J. Abell, C. –K. Kao, T. D. Moustakas, Phys. Stat. Sol. (a) **205**, No. 5, 1070 (2008).

Appendix B
Detailed Final Report

Task 1.3, UNLV,
“Electronic Properties of Nanomaterials for Light Emitting Devices”

PHOTONICS RESEARCH AND DEVELOPMENT FINAL REPORT
APPENDIX B – TASK 1.3
ELECTRONIC PROPERTIES OF NANOMATERIALS FOR LIGHT-EMITTING DEVICES

Project Title:	Electronic Properties of Nanomaterials for Light-Emitting Devices
Covering Period:	October 1, 2006 – August 30, 2009
Date of Report:	November 25, 2009
Recipient:	UNLV
Award Number:	Subcontract #RF-06-PRD-003
Cost-Sharing Partners:	None

Project Objective: The goal of this project was to utilize a unique combination of spectroscopic and microscopic techniques to assess the electronic structure of nanomaterials for use in light-emitting devices (LEDs). The results aid in the development of highly efficient LEDs and shed light on the underlying fundamental principles governing the electronic structure and contact formation to LED materials.

Results: In close collaboration with Prof. Ted Moustakas' group at Boston University (BU), the UNLV activities have focused on a deeper understanding of the electronic structure of nitride-based materials and contacts.

1. Contact Formation on p-type GaN

For p-type GaN, a metal layer stack of Au (50 Å)/Ni (50 Å) is usually deposited onto the GaN films for contact formation. The actual formation of the contact takes place by annealing the "contact stack" on the nitride samples in O_2-atmosphere at 500°C for 10 minutes. Based on microstructural studies, it was suggested that NiO islands are formed in this annealing process, which serves as the ohmic contact to the gallium nitride.

To investigate the contact formation, the deposited thicknesses of nickel and gold onto p-GaN were varied. In particular, the following samples were studied: bare p-GaN, Ni (25Å)/p-GaN, Au (5Å) / Ni (25Å)/ p-GaN, and Au (50Å) / Ni (50Å)/ p-GaN. The last sample represents the standard contact scheme. Parts of the contact/p-GaN samples were annealed in a furnace under O_2/air for 10 minutes at 500ºC. All the samples, along with relevant reference materials, were characterized by x-ray emission (XES) and x-ray absorption spectroscopy (XAS) at the Advanced Light Source (ALS), Lawrence Berkeley National Laboratory. These techniques are able to investigate the chemical environment of a specific element from 10's of nm to a few 100 nm into the surface. Thus, XES and XAS can probe the interfaces between p-GaN and the metal contacts.

The XAS and XES spectra at the Ni L edge are shown in Figs. 1 and 2, respectively. The Ni L_3 XAS spectra show significant differences between the annealed and unannealed samples. The differences are similar to that of the Ni L_3 XAS between NiO and Ni foil. The spectra of the unannealed samples are similar to that of metallic Ni. However, closer inspection of the unannealed spectra reveals a weak feature just below 852 eV. Comparing these spectra to the NiO reference spectrum indicates that the surface is slightly oxidized. Upon heat treatment, the metal contacts/p-GaN spectra have more pronounced NiO features. This can be interpreted as a continual conversion of metallic Ni to NiO. In addition, the spectra of the annealed samples show a reduction in peak width and a shift to higher energies (with respect to the absorption edge) when compared to the respective unannealed samples. This trend is also observed when comparing the XAS spectra of NiO to Ni foil.

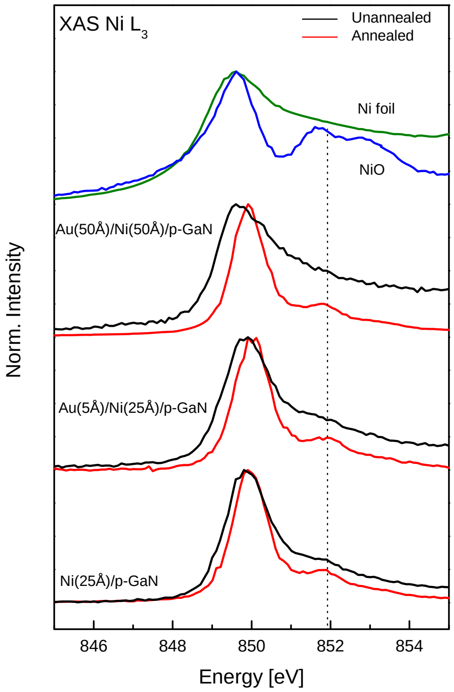

Fig 1. Ni L_3 XAS spectra of annealed and unannealed p-GaN samples along with reference materials of Ni foil and NiO powder.

Like the XAS spectra, the Ni $L_{2,3}$ XES data (Fig. 2) show that the Ni in the annealed and unannealed samples are in similar chemical environments to that of NiO powder and Ni foil, respectively. As seen in Fig. 2, the Ni L_2: Ni L_3 emission intensity ratio of NiO is greater than that of metallic Ni. Since the Ni density in NiO is smaller than in metallic Ni, this intensity ratio variation is due to less-pronounced self-absorption of the Ni L_2 emission in NiO compared to that of metallic Ni. For the contact stack samples, we observe that the annealed samples have a greater Ni L_2: Ni L_3 intensity ratio than the unannealed samples, in accordance with the above-described assignment to NiO formation after heat-treatment of the samples.

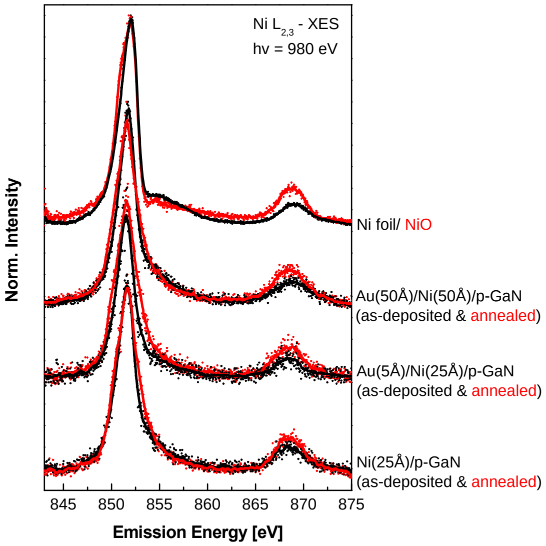

Fig. 2. Ni $L_{2,3}$ XES spectra of different contacts on p-GaN samples, along with reference spectra of NiO powder and Ni foil.

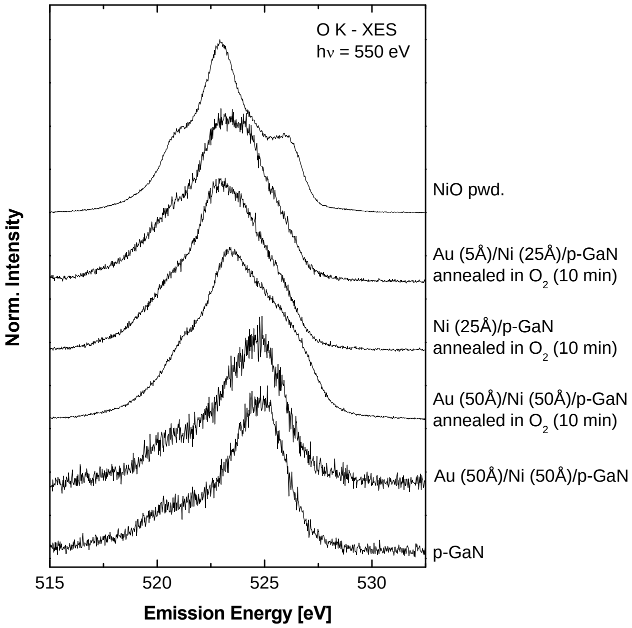

Fig. 3. O K emission spectra of various contacts on p-GaN samples and a NiO powder reference.

Normalized O K XES spectra of the contacts on p-GaN samples are shown in Fig. 3. The O K emission spectra of the uncovered p-GaN and Au(50Å)/Ni(50Å)/p-GaN samples have similar features while the spectra of the heated sample are different. The O K emission of the bare p-GaN is likely due to oxygen adsorbed on the surface. Upon closer inspection, the spectra of the annealed samples can be displayed as a linear combination of the O K XES spectrum of NiO powder and the bare p-GaN (see

Fig. 4). It can be seen that the NiO contribution for the annealed samples is dependent on the thickness of the gold layer. With or without a thin (5Å thick) gold layer, the O K emission spectra is presented as a sum with equal contributions of NiO and (oxidized) p-GaN. However, the O K XES spectrum of the p-GaN with a thicker layer of gold (50Å) has a dominating contribution from NiO.

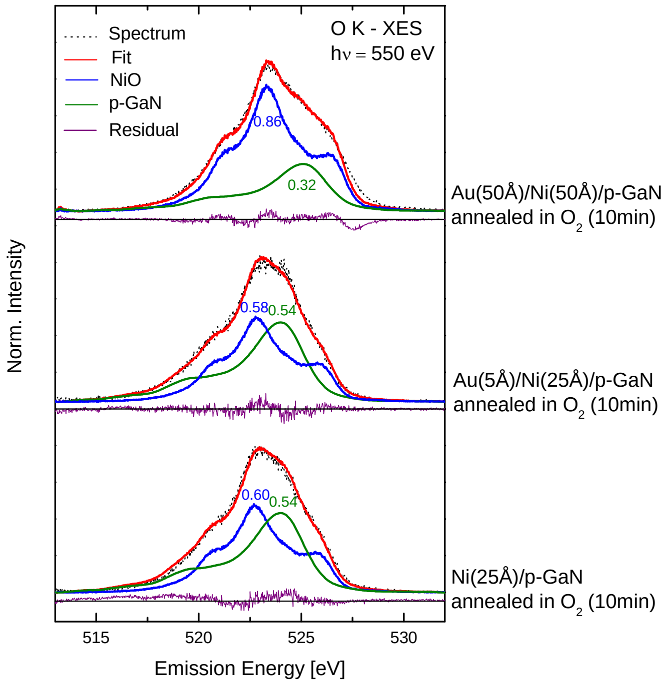

Fig. 4. The O K emission spectra of heated p-GaN samples are shown as a sum from the O K XES of NiO powder and (oxidized) p-GaN.

From the combination of XES and XAS spectra, we are able to deduce the contact formation onto p-GaN. As a result of the contact formation, we find that some of the Ni transforms into NiO.

2. Contact Formation on n-type GaN

For n-type GaN, a metal layer stack of Au/V/Al/V is deposited onto the GaN films for contact formation. The actual formation of the contact takes place by rapid thermal annealing (RTA) the "contact stack" on the nitride samples in N_2-atmosphere at 650°C for 30 seconds. At BU, it is speculated that VN is formed in this annealing process. Having a lower work function than V metal, it is believed that VN actually provides the ohmic contact to the wide-gap GaN. However, it is still under discussion how the VN forms – whether it forms due to the N_2 in the annealing atmosphere or "released" nitrogen from the GaN itself participates in the VN formation.

In order to investigate the contact formation by x-ray photoelectron (XPS) and x-ray excited Auger electron (XAES) spectroscopy, Au/V/Al/V/GaN/sapphire test structures with varying thicknesses of Au, V, and Al were characterized. In particular, the following samples were studied: bare n-GaN, Au

(1000Å)/V(200Å)/Al(800Å)/V(150Å)/n-GaN, and Au (100Å)/V(20Å)/Al(80Å)/V(15Å)/n-GaN. The latter two samples will be referred to as 'thick' and 'thin' contact samples, respectively. The thick contacts sample represents the standard contact scheme used in BU devices. Both the thick and thin contact samples were heat-treated by RTA at 650°C for 30 seconds at BU in N_2. Both XPS and XAES are surface-sensitive techniques that can offer insight into the surface composition.

The XPS Ga $2p_{3/2}$ and XAES Ga LMM spectra of the investigated samples are shown in Figs. 5 and 6, respectively. The symmetric Ga $2p_{3/2}$ XPS peak of the bare n-GaN (Fig. 5a) is indicative for one Ga species. In contrast, the RTA-treated contacts on n-GaN have more than one chemical species contributing to the spectra (Fig 5b and 5c), as indicated by the different pronounced spectral contributions to the Ga $2p_{3/2}$ XPS spectra. The presence of a second Ga species is more pronounced for the thick metal contact (Fig. 5c) as seen by the increasing high-binding energy shoulder of the Ga2$p_{3/2}$ peak. Preliminary spectral fits with Voigt profiles are also shown in Fig. 5 (solid lines).

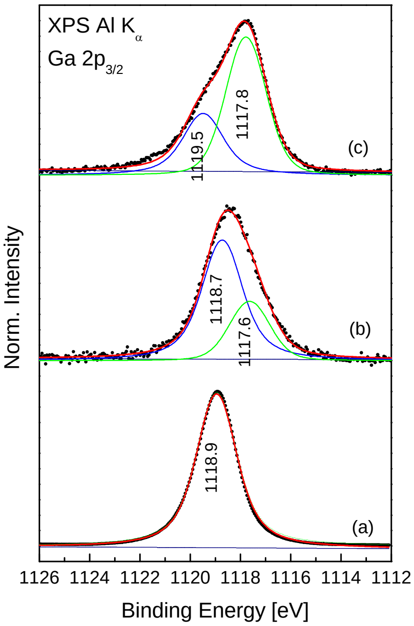

Fig. 5. Ga $2p_{3/2}$ XPS spectra of the (a) bare n-GaN, (b) RTA treated thin contact n-GaN, and (c) RTA treated thick contact n-GaN.

The changes in the Ga LMM Auger signals (Fig. 6) are more pronounced amongst the different samples. For the bare n-GaN (Fig. 6a), the spectral shape of the Ga LMM Auger signal again suggests the presence of one Ga species. However, the RTA-treated contacts on n-GaN show additional features at higher kinetic energies which are due the presence of Ga in more than one chemical environment. This observation is in agreement with the noticeable change in the Ga $2p_{3/2}$ XPS spectra. Similarly, the changes in the spectrum vary with contact thickness. The additional Auger feature at higher kinetic energies is much more pronounced for the thicker contact than the thinner. To properly identify the chemical species present on the samples, the modified Auger parameter (α') was computed. The modified Auger parameter for a given element is the sum of the binding energy of a core level and the kinetic energy of an associated Auger transition. For these samples, the Ga $2p_{3/2}$ and LMM positions were chosen [$\alpha' = E_{kin}$ (Ga LMM) + $E_{binding}$ (Ga $2p_{3/2}$)]. The modified Auger parameter is independent of any potential charging or band bending effects. The values of the Auger parameter for the samples are summarized and compared to reference values in Fig. 7. The α’ value for the bare n-GaN lies between published data for GaN and Ga_2O_3. Since the bare n-GaN sample had very little oxygen (contamination) on the surface, we believe that this α’ can be ascribed to GaN. For the RTA treated samples we can determine two α’ values; one for the higher binding energy (lower kinetic energy) and one for the lower binding energy (higher kinetic energy) component. For both contact samples, the first α’ lies in the same range as that of the n-GaN sample and thus can be ascribed to GaN (possibly with some Ga_2O_3 contribution). The other α’ value from the contact samples lies higher in energy and is in agreement with data published for metallic Ga. This indicates that nitrogen – as speculated above – is indeed released from the GaN during RTA treatment and hence could be involved in the formation of VN

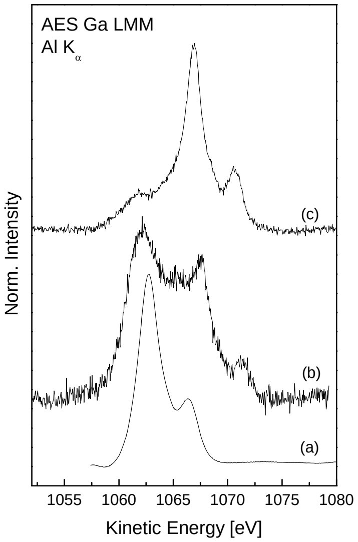

Fig. 6. Ga LMM XAES spectra of the (a) bare n-GaN, (b) RTA treated thin contact n-GaN, and (c) RTA treated thick contact n-GaN.

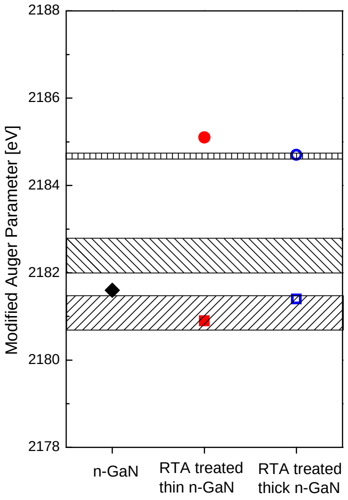

Fig. 7. The determined modified Auger parameter values for the samples are shown along with values published for various Ga containing compounds (from lower to higher energy: Ga_2O_3*, GaN, Ga metal). The error value in the calculated Auger parameters is ±0.1 eV.*

The X-ray photoelectron spectroscopy (XPS) survey spectra of the V-based contacts on n-GaN prior to RTA treatment are dominated by Au features due to the Au top layer (Fig. 8b and 8d; compare with Fig. 8a representing pristine n-GaN). Upon RTA treatment, the materials stemming from once buried layers (Al, V, and GaN) can also be detected by XPS and XAES, as seen in the survey spectra (Fig. 8c and 8e). However, the reason for detecting atoms from the once buried layers is unclear, and thus atomic force microscopy (AFM) measurements were conducted in air to deduce the morphology and to gain further insight into the layer structure of the contacts.

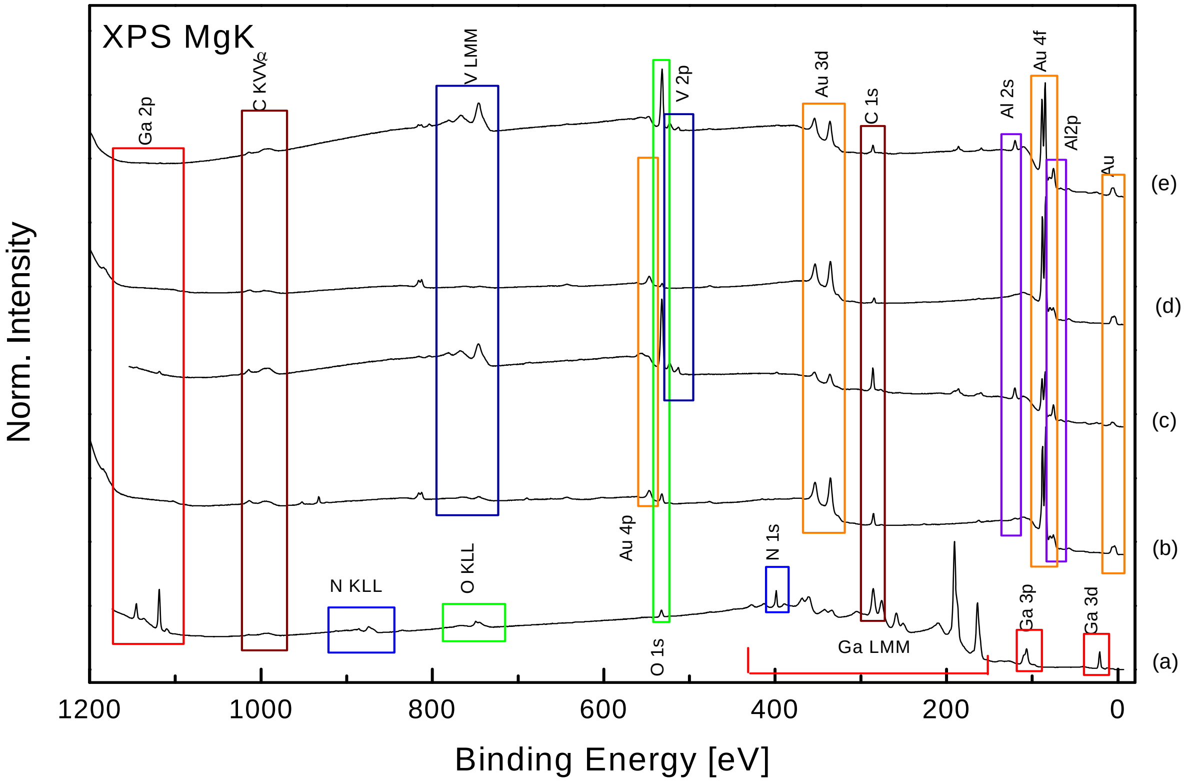

Fig. 8. The survey spectra of (a) n-GaN, (b) untreated thin contact n-GaN, (c) RTA treated thin contact n-GaN, (d) untreated thick contact n-GaN, and (e) RTA treated thick contact n-GaN.

AFM measurements, in both contact and non-contact (NC) mode, were performed on all samples mentioned in Fig 8. The contact-free n-type GaN surface is shown in Fig. 9. The surface of the sample consists of crystalline structures. The AFM images of V-based thin and thick contacts on n-GaN are shown in Fig. 10 and 11, respectively. The surface of the untreated thin contact on n-GaN consists of distributed "pits" (see Fig. 10a and 10c). We speculate that the pits are formed during an etch-step of the n-GaN surface prior to contact deposition (this etch step was not performed on the sample shown in Fig. 9). Upon deposition of the thin contact, the top surface of the film as well as the side surfaces of the pits are coated with metal, but since the metal layer is very thin, the etch pit morphology is retained. A close inspection of the corresponding XPS survey spectrum (Fig. 8b) shows traces of Al but no other buried layer material can be detected, which supports the finding of the AFM analysis that the metal contact layer covers both the external surface as well as the "internal" surfaces of the pits. Upon RTA treatment, the thin contact sample's surface morphology significantly changes (Fig. 10b and 10d). After RTA treatment, the contact material appears to have conglomerated into clusters. Consequently, areas between clusters are likely responsible for the detection of atoms from previously buried layers (such as Al, V, Ga, and N).

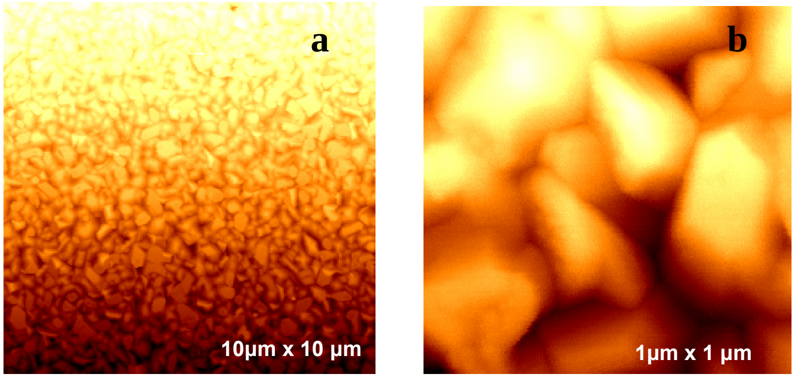

Fig. 9. NC-AFM images of n-GaN in a scan size of (a) 10 µm x 10 µm and (b) 1 µm x 1 µm.

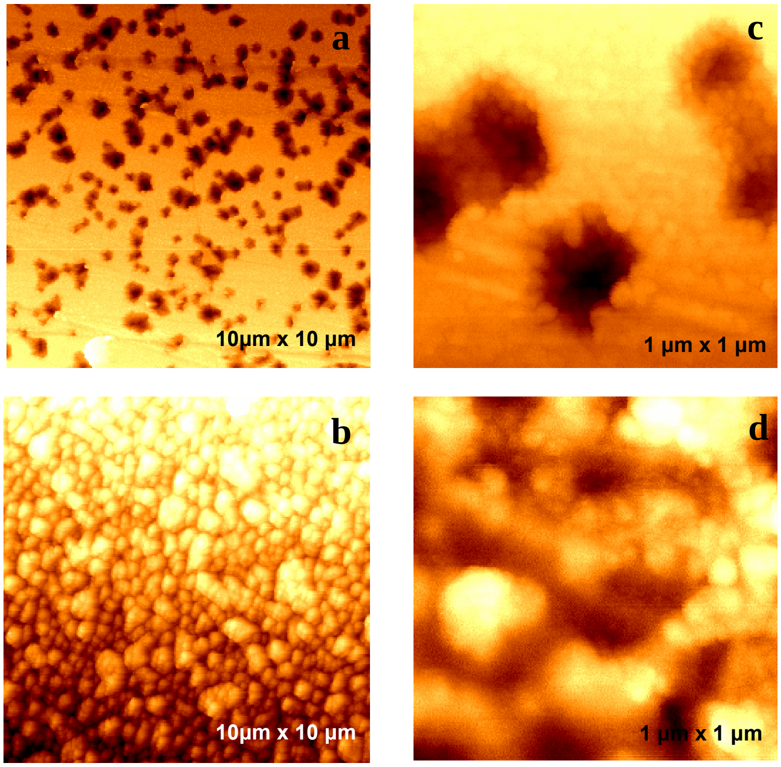

Fig. 10. AFM images of thin contacts on n-GaN (a) and (c) without RTA treatment, and (b) and (d) after RTA treatment.

The thick contact samples show distinctive morphology differences when compared to the thin contact samples (Fig. 11). Unlike the untreated thin contact samples, the untreated thick contact on n-GaN (Fig. 11a) has a relatively flat, closed Au layer without "pits" (also seen in a 10 x 10 μm^2 AFM image, not shown). After RTA treatment, the surface of the thick contact sample shows dendritic vein-like structures (Fig. 11b) in contact-AFM images. The surface far away from the dendrites of the non-vein like structure is shown in detail in Fig. 11c and 11d. Similar to the RTA-treated thin contact samples, there appears to be an aggregate of clusters with voids. The presence of voids and cluster formation confirm the results seen in the XPS where atoms from previously buried layers are detected.

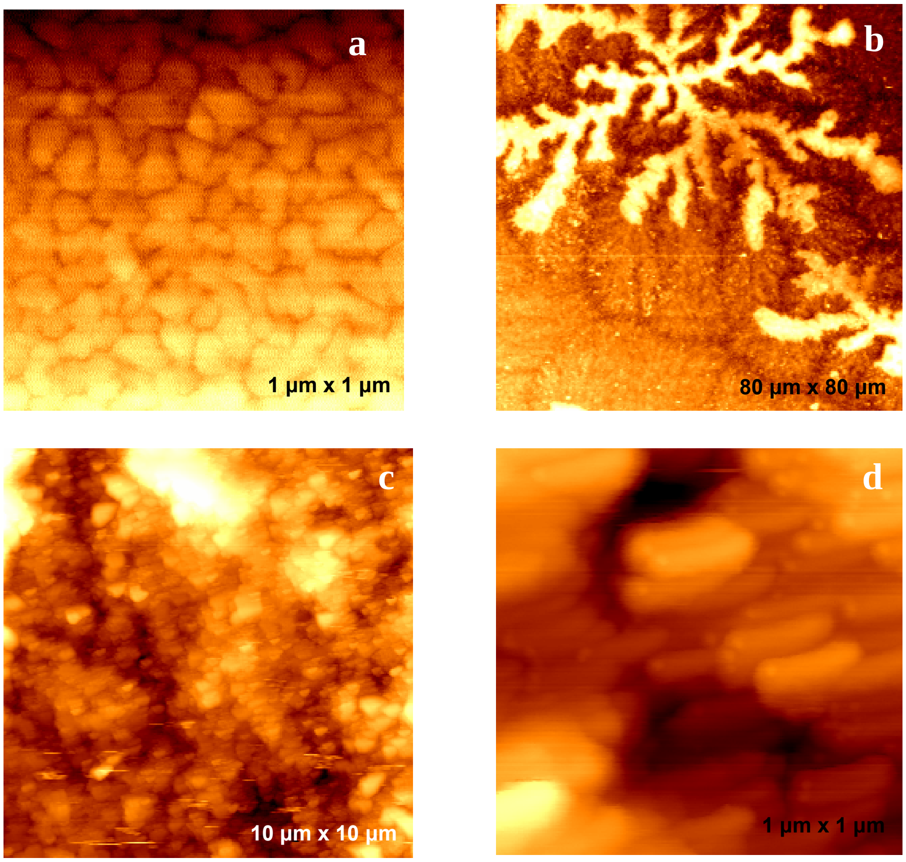

Fig. 11. AFM images of thick contacts on n-GaN (a) without RTA treatment, and (b-d) after RTA treatment.

To identify the composition of the "veins" and areas between the "veins", the thick RTA-treated sample was analyzed by electron probe microanalysis with wavelength dispersive spectroscopy (WDS). The WDS method provides a 2-D elemental map to decipher the relative concentration of each element present. The dendritic surface morphology is shown in the back-scattered secondary electron microscope (SEM) image (Fig. 12), which was taken in the area probed by the WDS. As is evident from the SEM image, three different surface "levels" exist on the surface: the dendrites (white regions), the actual surface (grey regions), and cracks in the actual surface (dark regions).

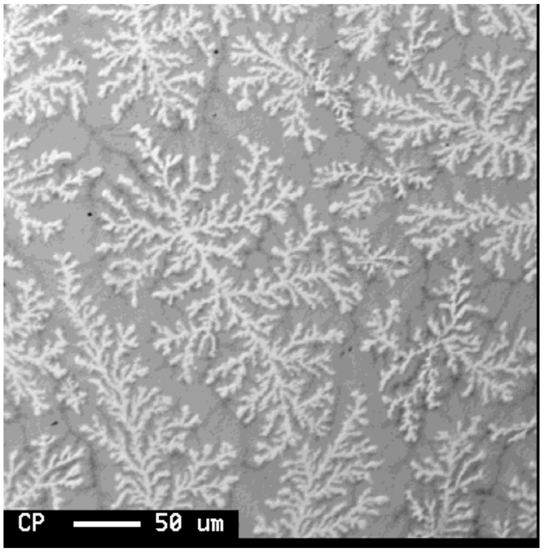

Fig. 12. Backscattered electron SEM image of the RTA-treated thick contact sample.

WDS element maps for Al Kα, V Kα, Au Mα, and Ga Lα are shown in Fig. 13 for the RTA-treated thick contact sample. The map for Al (Fig. 13a), shows an approximately equal distribution in the sample and the "veins" are not easily distinguishable. In contrast to the Al map, the V, Au, and Ga maps show different elemental concentrations amongst the "veins" and areas between the "veins." The Au map (Fig. 13c) indicates that the gold is mostly at the veins and particularly weak in the cracks. Vanadium and gallium (Fig. 13b and 13d, respectively) are higher in concentration in areas between the veins than on the veins. The Ga (Fig. 13d) has the highest concentration at the cracks between the veins which is expected since the GaN is initially buried under ~200 nm of metal contact layers. The cracks are about 40-50 nm below the area between the veins while the veins are about 200 nm tall (as measured by AFM in air).

The WDS x-ray maps are able to provide us with more clues to the RTA-treatment on n-type GaN for contact formation. As mentioned, the RTA treatment results in the formation of VN as shown by XES. As mentioned, the formation of VN was previously speculated since its low work function is compatible with that of n-GaN. From XES results, the nitrogen probed was in a VN chemical environment, but the V probed was in two distinct chemical environments. It was mostly unconverted as metallic V and reacted as VN. The presence of metallic V is likely due to characteristics of the contact scheme: while the upper V layer remains metallic, the lower V layer at the V-GaN interface undergoes VN formation. The VN formation is supported by the XPS and XAES results where metal-like Ga was detected at the surface, thus indicating that a Ga-V exchange occurred where the nitrogen source of VN came from the GaN. We propose that upon RTA treatment, the veins (top) are formed which are mostly composed of Au and Al, and that most of the vanadium detected remains between the veins, thus supporting the V-Ga exchange. Using all these techniques, we are able to paint a clearer picture of the contact formation on n-type GaN.

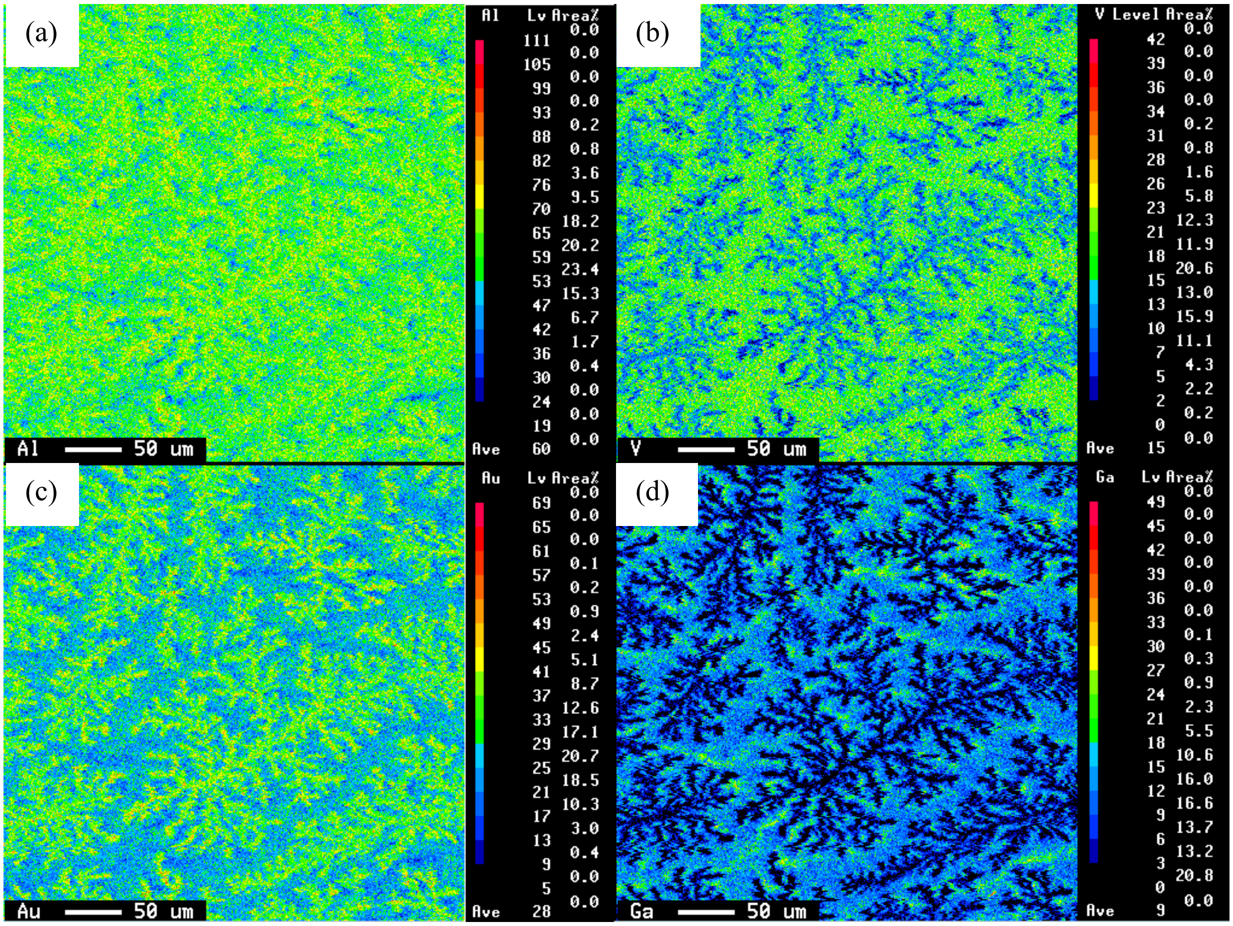

Fig. 13. WDS element maps of the RTA-treated thick contact sample for (a) aluminum, (b) vanadium, (c) gold, and (d) gallium.

3. Contacts on n-type AlN:

For n-type AlN contact studies, our partners at BU deposited a metal layer stack of Au/V/Al/V onto the AlN films for contact formation. The investigated n-AlN samples with contacts consisted of a "thin" (Au(100Å)/V(20Å)/Al(80Å)/V(15Å)) and "thick" (Au(1000Å)/V(200Å)/Al(800Å)/V(150Å)) scheme. The contact scheme is the same as for n-GaN, and is intended for the n-$Al_xGa_{1-x}N$ alloy. The formation of the contact on n-AlN takes place by RTA of the "contact stack" on the nitride samples in N_2-atmosphere at 1000°C for 30 seconds. This processing temperature is much higher than the 650°C for n-GaN for reasons discussed below. Like for V-based contacts on n-GaN, it is hypothesized that vanadium nitride (VN) is formed from the contact formation. The formation of VN is of interest since it has been attributed to the Ohmic contact formation on n-$Al_xGa_{1-x}N$. It was shown by the Moustakas group that, for increasing Al content in the alloy, the RTA-treatment temperature had to be increased in order to achieve an Ohmic contact. Thus, the mechanism of the contact formation on n-AlGaN is likely to be different for little or no Al content (i.e., pure GaN) than for little or no Ga content (i.e., pure AlN).

XPS was used to analyze the surface composition of samples before and after RTA treatment. In Fig. 14, the survey spectra of thick untreated, thick RTA-treated, thin untreated, thin RTA-treated, and bare n-AlN are shown. The untreated samples have photoemission lines dominated by Au since it is the topmost layer. Upon RTA heat-treatment, elements from originally buried layers (*i.e.*, V, Al, and N) are now detected at the surface. The O 1s signal of the RTA-treated samples is pronounced compared to that of their untreated counterparts.

For some samples, we find the presence of F, Zn, and Cu. The F and Zn are likely due to the temporary UNLV chamber contamination; however, the source of Cu is still unknown.

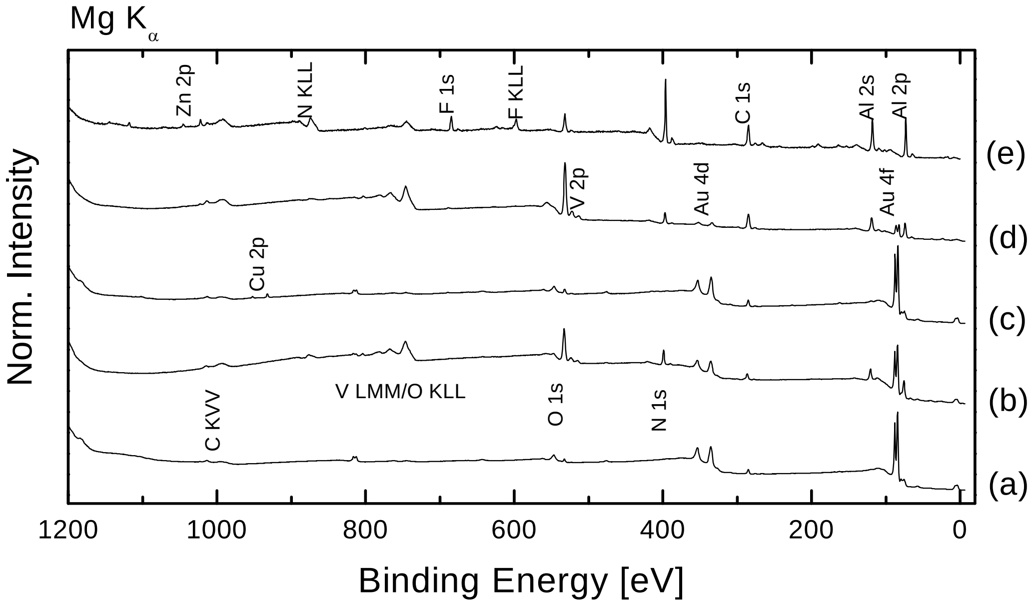

Fig. 14. XPS survey spectra of (a) untreated thick contact n-AlN, (b) RTA-treated thick contact n-AlN, (c) untreated thin contact n-AlN, (d) RTA-treated thin contact n-AlN, and (e) n-AlN.

The V $2p_{3/2}$ and Au 4f XPS spectra are shown in Fig. 15a and 15b, respectively. XPS lines associated with V were only seen in samples after RTA-treatment. For both the thick and thin contacts on n-AlN, dominant peaks at lower binding energy are observed, which corresponded well to the metallic V reference foil. The V $2p_{3/2}$ XPS spectra provide complementary data to the V L_3 XES data (Fig. 17), where the thick contact appears to have a contribution from metallic V (see discussion below). For both the thick and thin samples, a shoulder appears at higher binding energies (~517 eV), which is more pronounced for the thick contact sample. Further data evaluation (spectra fitting) will need to be performed to get additional insights.

The Au 4f XPS spectra are shown in Fig. 15b with the untreated samples in black and the RTA-treated in red. The Au 4f spectra of the untreated samples are in agreement with metallic Au. Upon RTA-treatment, the Au 4f spectra broaden and shift towards lower binding energies. Both effects are more pronounced for the thick contact scheme. The broadening of the spectra is possible indication of an additional Au species or alloy formation; again, further fit analysis is needed for final clarification.

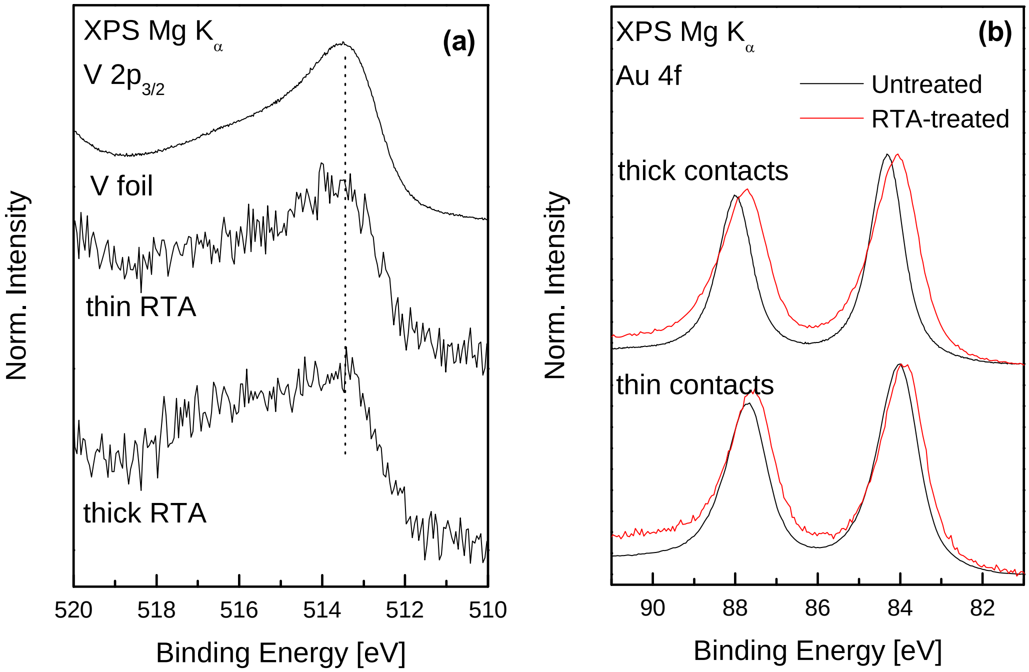

Fig. 15. (a) V $2p_{3/2}$ XPS spectra and (b) Au 4f XPS spectra of untreated and RTA-treated contacts on n-AlN samples and a reference V foil.

Complementary to XPS measurements, XES experiments were also conducted (shown in Fig. 16 and 17). The nitrogen K (N K) emission of the untreated and RTA-treated samples along with reference n-AlN and VN powder are shown in Fig. 16. Spectra (b), (c), and (e) are very similar to n-AlN (a). The spectrum of the untreated thick contact n-AlN shows only a weak nitrogen signal, as expected (since the AlN is buried under ~215 nm of contact metal). The spectrum of the *RTA-treated* thick contact n-AlN, in contrast, shows a significant nitrogen signal that looks very similar to the n-AlN reference spectrum (a). Further analysis was performed (*i.e.*, spectral subtraction) to deduce additional spectral contribution to the RTA-treated thick contact n-AlN (Fig. 16f). A weighted amount (0.8) of AlN (a) was subtracted from the RTA-treated thick contact (e), which resulted in the difference (f). The difference spectrum (f) is very similar to that of VN (g). The difference spectrum contains the high energy shoulder (around 396 eV) and a broad peak (centered around 391 eV) similar to those of the VN spectrum (g). Spectral subtraction was attempted on the RTA-treated thin contact, but the nitrogen signal was dominated by the AlN. Thus, we find that upon RTA-treatment, the nitrogen atoms are present in two distinct chemical environments: AlN (dominant) and VN.

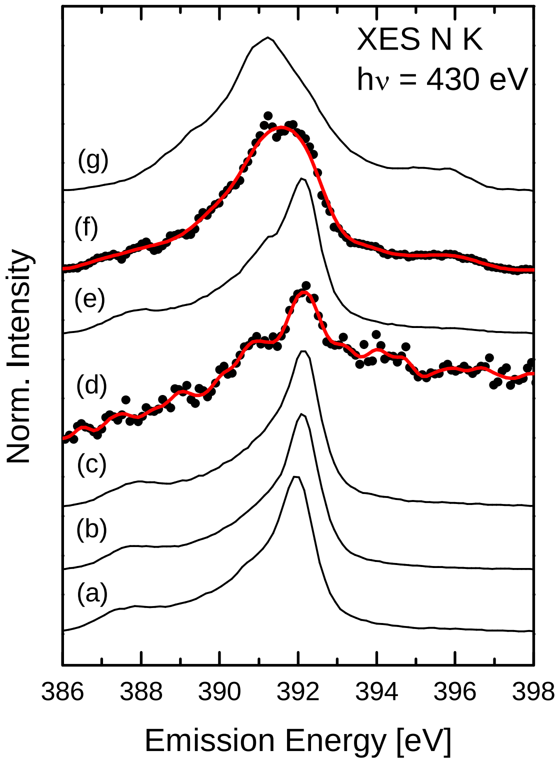

Fig. 16. N K XES spectra of (a) n-AlN, (b) untreated thin, (c) RTA-treated thin, (d) untreated thick, (e) RTA-treated thick, (f) difference, and (g) VN. The difference spectrum is n-AlN (a) subtracted from RTA-treated thick (e). The red line denotes a "smoothing" procedure as a guide to the eye.

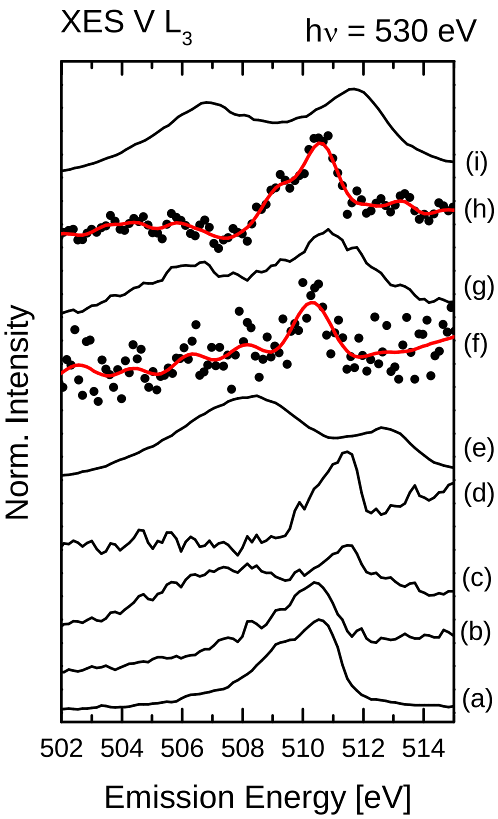

Fig. 17. V L_3 XES spectra of (a) V metal, (b) untreated thin contact, (c) RTA-treated thin contact, (d) RTA-treated thin difference, (e) VO_2, (f) untreated thick contact, (g) RTA-treated thick contact, (h) RTA-treated thick difference, and (i) VN.

In Fig. 17, the V L_3 XES spectra of the samples and relevant references are shown. As expected, the untreated thick and thin contact samples (Fig. 17b and f) show a vanadium emission similar to that of metallic vanadium (Fig. 17a). However, upon RTA treatment, the shape of the V L_3 emission changes and displays two distinct peaks. The RTA-treated thin contact (Fig. 17c) displays a broad feature at lower emission energies which is similar to that found in the VO_2 spectrum (Fig. 17e). The RTA-treated thick contact has a feature at lower emission energies that coincides well with the VN spectrum. Like for the N K XES result, spectral subtraction was performed on the RTA-treated samples. For the RTA-treated thin sample, VO_2 (weighted 0.77) was subtracted, and the result, shown in Fig. 17d (labeled RTA-treated thin difference), is similar in shape to that of metallic vanadium (Fig. 17a). From this, we find that the RTA treatment leaves the vanadium atoms in either metallic form or converted to VO_2. In the case for the RTA-treated thick contact sample, VN (weighted 0.73) was subtracted, and the result, shown in Fig. 17h (labeled RTA-treated thick difference), also appears to be similar to that of vanadium metal. Thus, for the thick contact sample, the RTA treatment either has vanadium atoms in metallic form or has converted them to VN. While we see evidence of the presence of VN in the thick contact sample, we speculate that the RTA-treatment of the thin contact sample was unable to produce a detectable (using XES) amount of VN due to (1) the thinner interfacial V layer thickness (between the AlN and Al layers) (i.e., fewer V atoms to interact with AlN), and (2) the significant decrease in thickness of the metal overall layer (x10 less) aided in the oxidation of V (instead of nitridation).

In summary, we find that the nitrogen atoms are in two different environments – unchanged as AlN (dominant) and reacted to form VN. Preliminary results of the analysis of the V L_3 XES spectra show that the vanadium atoms are in a metallic V and VN environment. The V $2p_{3/2}$ XPS spectra indicate that the vanadium is not in a single chemical environment, while the Au 4f spectra show that the Au is not benign in the contact formation either. The survey and V $2p_{3/2}$ XPS spectra also point to the possibility of intermixing as a result of contact formation.

Patents: None

Publications: "Intermixing and chemical structure at the interface between n-GaN and V-based contacts", S. Pookpanratana, R. France, M. Bär, L. Weinhardt, O. Fuchs, M. Blum, W. Yang, J. D. Denlinger, T. D. Moustakas, and C. Heske, Appl. Phys. Lett. **93**, 172106 (2008). (3 pages)

Presentations:

Sujitra Pookpanratana presented a poster on “Au/Ni Contacts on p-type GaN: Contact Formation Investigated with Electron and Soft X-ray Spectroscopies” at the 7th International Conference on Nitride Semiconductors in Las Vegas, NV, Sept. 19, 2007.

Sujitra Pookpanratana presented a talk on “Contact Formation on GaN investigated with Electron and Soft X-ray Spectroscopies” at the Materials Research Society Fall 2007 Meeting in Boston, MA.

M. Bär presented an invited talk on “Spectroscopic Characterization of Thin Films Used in Energy Conversion Devices”, at the American Chemical Society 42nd Western Regional Meeting, Las Vegas, USA, September 22-26, 2008.

C. Heske presented an invited talk on “How soft x-ray spectroscopy can shed light on the electronic and chemical properties of interfaces“, at the PIRE-ECCI (Partnership for International Research and Education) Seminar, Electron Chemistry and Catalysis at Interfaces, Department of Chemistry and Biochemistry, University of California, Santa Barbara, November 5, 2008.

S. Pookpanratana presented a talk on “Contact Formation on GaN-based Semiconductors Investigated with Electron and Soft X-ray Spectroscopies” at the Spring 2009 Materials Research Society on 15 April 2009 in San Francisco, CA.

S. Pookpanratana presented a talk on “Impact of oxygen-annealing on the morphology and chemical properties of Au/Ni contacts on p-GaN” at the Spring 2009 European Materials Research Society on 11 June 2009 in Strasbourg, France.

Appendix C

Master's in Electrical Engineering Thesis,
"A Novel RGBW Pixel
For LED Displays"

A NOVEL RGBW PIXEL FOR
LED DISPLAYS

by

Neveen Shlayan

Bachelor of Science
University of Nevada, Las Vegas
2006

A thesis submitted in partial fulfillment
of the requirements for the

Master of Science Degree in Electrical and Computer Engineering
Howard R. Hughes Department of Electrical and
Computer Engineering College of Engineering

Graduate College
University of Nevada, Las Vegas
December 2008

Approval page

ABSTRACT

A Novel RGBW Pixel for LED Displays

by

Neveen Shlayan

Dr. Rama Venkat, Examination Committee Chair
Professor of Electrical Engineering
University of Nevada, Las Vegas

In this work, a novel pixel configuration RGBW, consisting of red (R), green (G), blue (B), and white (W) LEDs, is employed and investigated for color generation. Energy consumption and various hues of new pixels are compared to standard pixels consisting of RGB LEDs. Human perception experiments are conducted in order to study the perceptual difference between the two architectures when the same colors are generated using RGBW vs. RGB. Power measurements for an 8x8 pixel LED display has demonstrated up to 49% power savings for gray scale, over 30% power savings for low saturated colors, and up to 12% for high saturated colors using RGBW as an alternative. Furthermore, human perception studies has shown that vast majority of test subjects could not distinguish between most colors displayed using RGB and RGBW showing that RGBW is an excellent substitute for RGB. Statistics has shown that 44% of test subjects found the colors in gray scale to be the same, whereas 82% and 95% of test subject found low saturated colors and high saturated, respectively, colors to be identical.

TABLE OF CONTENTS

LIST OF FIGURES

LIST OF TABLES

ACKNOWLEDGMENTS

I would like to acknowledge my advisor and committee chair, Dr. Rama Venkat, for his thesis guidance, the technical and editorial help and for being devoted to his students. I would also like to thank, Dr. Paolo Ginnobi, for the practical teaching and training of concepts and hardware implementation of the project. In addition, I would like to thank Dr. Ashok Singh for the statistical counseling and help. Last but not least, I would like to acknowledge, Dr. Emma Regentova and Dr. Mohamed Trabia, for being members in my committee. Financial support from DoE grant # DE-FG36-05GO85032 is greatly appreciated.

CHAPTER 1

INTRODUCTION

Every year, the display industry introduces many innovations to improve quality and economy of displays. The factors, which contribute to the superiority of various displays, are: response time, size, weight, viewing angle, brightness, screen life, and power consumption. The current market places very high expectations in terms of the quality of the display. The limitations of the liquid crystal display (LCD), size and brightness, and that of the Plasma display, image retention and size [1] render them unsuitable for certain applications such as billboards and entertainment displays [2,3,4]. LED displays, which are perfect fit for such applications, just like any other technology have some issues, such as cost, power consumption, and achromatic point (AP) maintenance.

LEDs are semiconductor devices that are capable of fast switching with the addition of appropriate electronics [5]. Different types of LED displays were initially introduced in the early 70s such as LED array with silicon micro reflector and integrated circuits for driving LEDs. The reflector is formed on a silicon wafer by anisotropic chemical etching. LEDs on the unit are arrayed in a matrix structure and the strength of light emission is controlled by the pulse width of the current into the LEDs [6]. In the other type of display, the LED chips are mounted on the driving circuits that allow holding and controlling of the selected LED currents. Integrated circuit drivers are superior in brightness to the silicon micro reflector displays and therefore are still used for the current LED display technologies.

In the early seventies, when LED displays were first originated, red was the only color available. By the late seventies, the color variety became wider to include green, yellow, orange and red [7]. Solid state has witnessed significant advancements to improve LED's brightness by up to 40% per year [7]. Shuji Nakamura of Nichia Corporation of Japan demonstrated the first high-brightness blue LED based on InGaN which quickly led to the development of the first white LED, which is basically a yellow LED with a phosphors coating to produce a blue light. The mixture of yellow and blue lights produces a white light.

Advancements of LED technology tremendously improved LED display technology. The fact that obtaining light of the colors red, green, and blue was feasible, LED displays went through a revolutionary phase. RGB are monochromatic colors or centered about a single wavelength with a small bandwidth. The mixture of the three lights with the different possible intensities for each light results in a forth unique color perceptible to the human eye. The possible range of colors that can be produced using RGB is called the color gamut. Thus, LED display technology uses RGB LEDs to form a pixel in order to produce any color in the gamut. The LEDs in the display are connected to an integrated driver chip that controls each and every LED individually and hence the pixel.

In LEDs, colors are produced by a recombination process where electrons and holes are recombined. As a result, the electron falls into a lower energy level and the excess energy is released in a form of photons with a certain wavelength which determines the color to be perceived after the emission. This process is power consuming. There are many factors that affect the efficiency of LEDs such as the wavelength of the emitted photon and the human visual perception. The human eye, for example, is more sensitive to green in day vision than red and blue. It is, however, more sensitive to blue in night vision. Taking these factors into consideration, efficiency of LED displays could be further improved.

Since LED's I-V characteristics are not identical due to manufacturing imperfections, usage, weather conditions, and heat dissipation, it is a challenge to maintain a uniform color throughout the display throughout its life time. The difference between the colors becomes more noticeable in gray scale or, in other words, when LEDs are at equal intensity. This may be noticed as different shades of the color displayed or as spots of discoloration at random locations on the display.

High cost is one of the disadvantages in LED displays due to the expensive process used. Thus, maintenance costs are one of the major issues of LED displays. Therefore, one of the purposes of this work is to increase the life time of LED displays as much as possible in order to avoid these maintenance costs.

The three major drawbacks identified in the current RGB LED display technology are: power consumption, degradation of display, and cost. In order to address these three issues, a new pixel architecture including a white LED in the traditional RGB LEDs configuration is proposed. A 5"x5" board containing RGBW LEDs placed in a square configuration is used for the investigation.

In chapter 2, a survey of different types of display technologies and the current state of the art advancements are presented. Theoretical foundation of this work is presented in chapter 3. Chapter 4 presents the design of the front end software and hardware. The proposed technology is introduced and discussed theoretically as well. Results and discussions of human experiment and energy measurements are in chapter 5. Then conclusions and recommendations are in chapter 6.

CHAPTER 2

DIFFERENT DISPLAY TECHNOLOGIES

In this chapter, different display technologies with state of the art technological developments are presented. A detailed survey of LED technology and recent trends are also presented.

2.1 Liquid Crystal Display (LCD)

LCDs have come into prominence in the last few years because of their low power consumption and picture quality. LCDs are power efficient since they either reflect or transmit light efficiently [8]. Therefore, LCDs are very suitable for battery-powered electronics such as: cell phones, ipods, laptops, calculators, and digital watches.

In LCDs, every pixel is composed of a cell between two glass plates coated with a conductive material as shown in figure 2.1. The light utilized by the LCD display goes through a polarizer before going through the cell. The cell is basically filled with liquid crystal material which is a phase of matter over a certain temperature range. At the lowest end of the range, the material becomes crystalline with a set of optical and electrical properties; whereas, at the upper end of the range, this material becomes clear liquid with a different set of electrical and optical properties. However, within this range the material combines some of the optical properties of solids with the fluidity of liquids [8]. One of the most important characteristic of the liquid crystal material is the rod shape of its molecule. These rods can take a certain orientation with respect to each other and to the surface of the cell. The most widely used orientation in LCD technology is twisted nematic. In nematic ordering, all the rod shaped molecules (directors) are parallel to each other. The direction of this ordering can be changed by applying an electric field to the liquid crystal material. A schematic Diagram illustrating the operation of an LCD cell is shown in Figures 2.1 a and b.

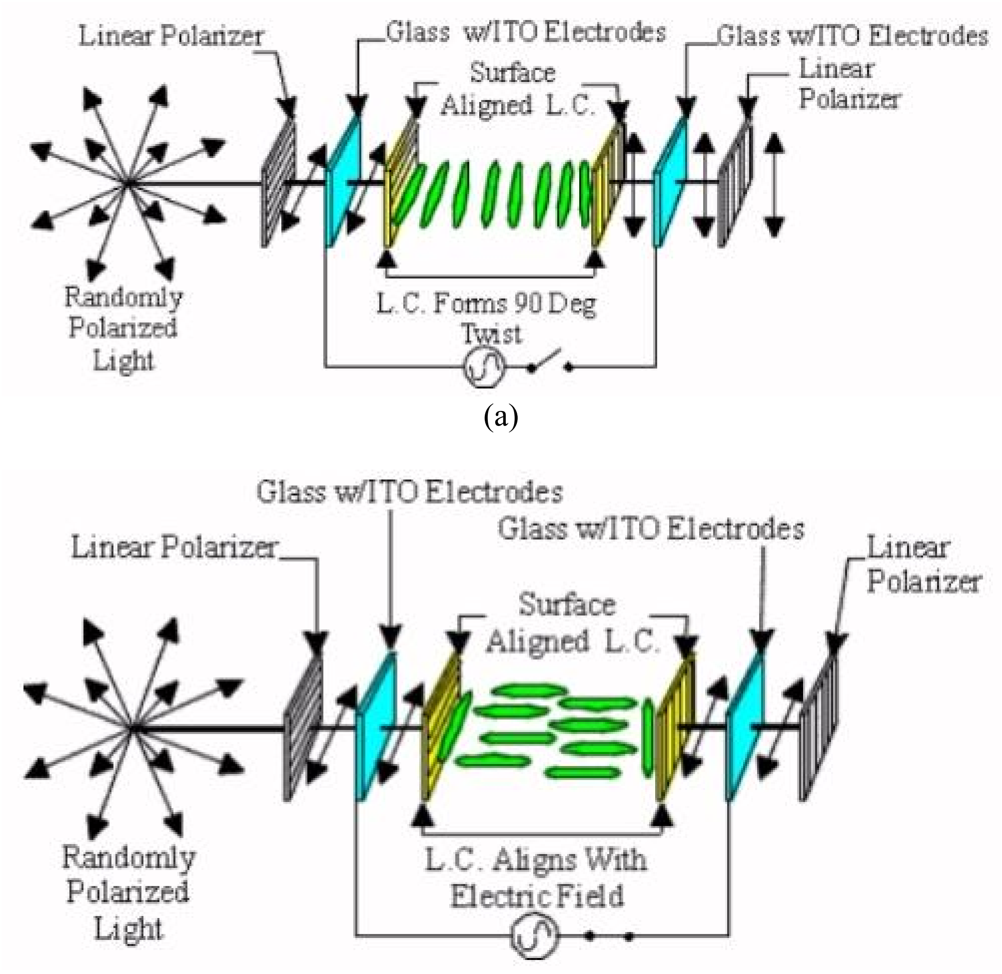

(a)

(b)

Figure 2.1 A schematic diagram showing a liquid crystal cell in the (a) off state (b) on state [9].

There are two types of LCDs: reflective and transmissive. The first of which utilizes front illumination. Most displays of the reflective type use ambient light with provision for secondary illumination such as an incandescent lamp or LED when ambient light becomes insufficient. On the other hand, the transmissive type requires rear illumination.

There are two types of architectures for LCD displays: passive matrix and active matrix. In passive-matrix addressed topology, each row or column of the display has a single electrical circuit. The pixels are addressed one at a time by row and column addresses. The pixel must retain its state between refreshes without the benefit of a steady electrical charge. This becomes less feasible as the number of pixels increases, since the response time will increase as well, resulting in a poor contrast which is typical of passive-matrix addressed LCDs.

Active matrix architecture results from adding a matrix of thin film transistors (TFT) to the polarizing and color filters. Each pixel is controlled by a single transistor. A schematic diagram showing the TFT active matrix array is shown in Figure 2.2. When a row line is activated, all the columns connect to the pixels in the selected row driving the appropriate voltage while the rest of the rows are electrically isolated which reduces cross talk. The row lines are activated in sequence during the refresh period in order to charge the capacitors that belong to each pixel with the desired amount given by the column voltage [10]. This method has largely improved the quality of LCD displays guaranteeing a brighter and sharper image than passive matrix. Most importantly, active matrix has significantly improved the response time.

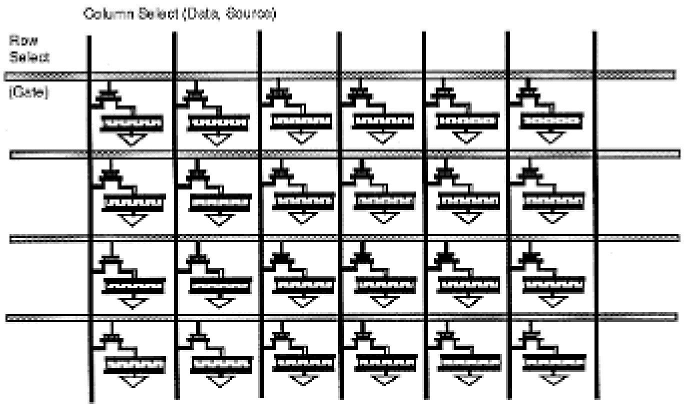

Figure 2.2. A schematic diagram showing simple TFT Active Matrix Array [11]

TFT technology, however, is very complex and the cost increases rapidly with increasing the area of the matrix [10]. Another disadvantage of TFT displays is that the transistor blocks part of the light-path which limits the resolution which requires a brighter backlight.

LCD technology, however, has its draw backs such as low contrast ratio, image scaling, ghosting (resulting from low response time), limited viewing angle, fragile, and dead pixels. This limits their usage to certain application such as billboards. LCD displays are equipped with an illuminator called a backlight system disposed at the rear surface. Thus, the amount of light from the backlight which transmits through the liquid crystal panel is controlled by the liquid crystal panel in order to realize images, which makes it more challenging to obtain dark colors. Low contrast ratio is a result of the unwanted light leakage in dark areas and passive full-on backlight control [12]. LCD screens can only display native resolution which is the number of pixels in every vertical and horizontal line that make up the LCD matrix. Changing the resolution settings of the display will cause it to use a reduced visible area of the screen or to extrapolate in which multiple pixels are blended together. This can result in a fuzzy image [13].

In an LCD, there are two different time responses describing two different transitions. Rising time response, which is the amount of time required to turn on the cell from an off-state and falling time response, which is the amount of time required to turn off the cell from an on-state. Rising time is much smaller than falling time. Thus, a blurring action will occur on bright moving images on black background or in other words ghosting effect.

Images in LCDs are produced by having a film that will turn on the desired shade of color when a current is applied to the pixel. This color can only be accurately represented when viewed straight on which could be problematic. The color tends to wash out when viewed further away from a perpendicular viewing angle [13].

2.1.1 Recent Trends in LCD Technology

LCD monitors are very desirable in the current market especially for applications like computer monitors, portable electronics, laptops, etc. Thus, recent market has been witnessing many competitors such as Gateway, Samsung, Dell, and Lenovo attempting to come up with the best LCD in the market by improving viewing angle, contrast ratio, resolution, and size.

Gateway has recently launched their XHD3000 monitor. It offers a wide-range of connectivity options along with bright picture and an up-scaler [14]. Then Samsung's brand new 743B offers a 1280x1024 resolution, fast 5ms response time and a 7000:1 contrast ratio [14]. Dell has recently developed an award winning LCD monitor sandwiched between layers of clear glass are significant advancements in LCD display;

protruding elegantly from the rear of the monitor are minimal speaker housings. All of the electronic wiring for the capacitive touch controls, digital camera, and the speakers has visible wire traces [15]. Lenovo has produced a 22" LCD monitor that offers a 1920 x 1200 native resolution [14].

2.2 Plasma Display

Plasma technology was invented at the University of Illinois in 1964 by Donald Bitzer, H. Gene Slottow, and graduate student Robert Willson [16]. Larry Weber developed the first prototype of a 60-inch plasma display that combines many of the industry’s desirable features such as large size, high definition, and thickness.

Plasma has many characteristics that increased the demand for plasma technology in the display industry especially home entertainment. Plasma displays are bright, have a wide viewing angle, have a wide color gamut, and can be produced in large sizes, up to 150 inches diagonally [17]. Compared to the LCD, plasma displays have a better low luminance black level. The total thickness of a plasma display, including electronics, is less than 4 inches; the display panel by itself is only about 2.5 inches thick [17]. Power consumption differs with the brightness level of the image displayed, with bright scenes drawing significantly more power than darker ones. Nominal power rating is typically 400 watts for a 50-inch screen. Newer models (after 2006) consume 220 to 310 watts for a 50-inch display. The lifetime of the latest generation of plasma displays is estimated at 60,000 hours of actual display time [17].

Plasma displays are based on light generation. When an electrical current passes through gas, the electrons acquire a high kinetic energy, and when they collide with the gas atoms, they transfer their kinetic energy to the atoms exciting them into energy levels above their ground state. Either direct or alternating currents can be used in order to generate an internal electric field. A plasma element is composed of a gas cavity with transparent electrodes on the outside of the containing dielectric layer as shown in Figure 2.3. The gas is normally neon that is electrically turned into plasma which, then, excites the phosphors to emit white light.

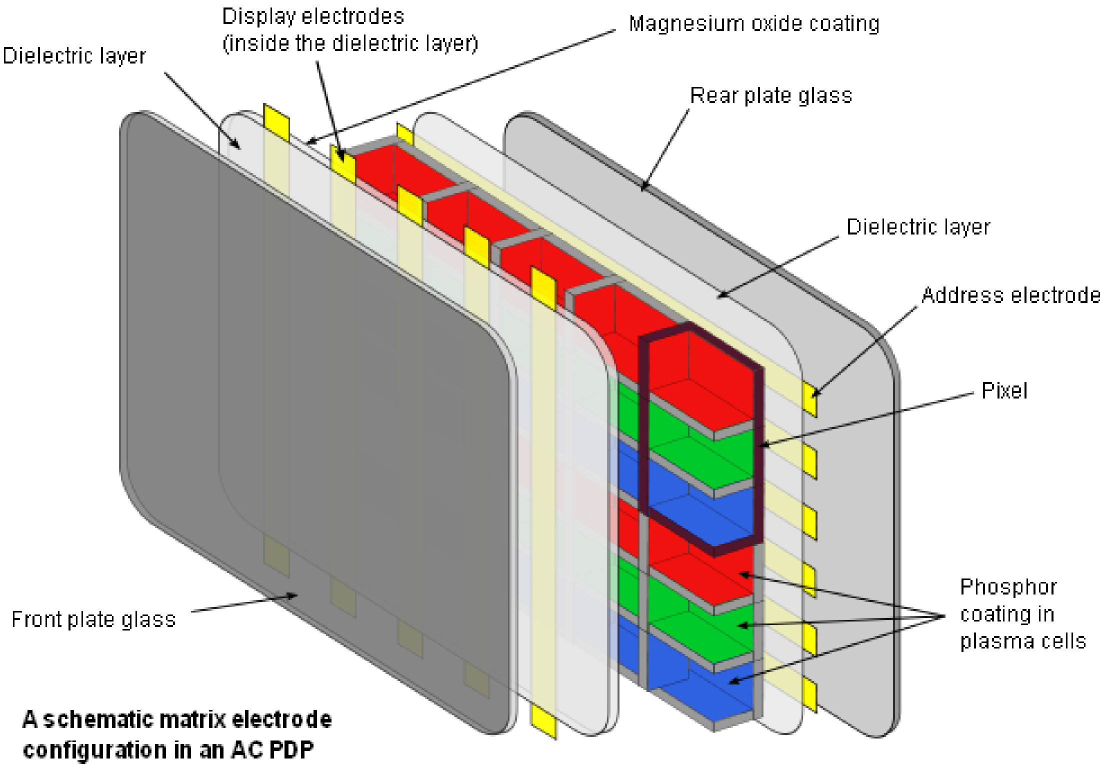

Figure 2.3. A schematic diagram showing a composition of plasma display panel [17]

The driving circuitry of the plasma display technology has been a major issue due to its complexity. To drive a plasma display, the driving circuit must apply high voltage and high frequency pulses to the scan electrodes [18]. The address-electrodes are located under the cells perpendicular to the X and Y electrodes. A schematic diagram showing the 3-electrods of AC plasma display is shown in Figure 2.4. As mentioned, cells in a plasma display emit visible lights via a plasma discharge induced by a pseudo square alternating electric field applied between the X and Y electrodes [19]. For charging the panel capacitance and supporting the plasma discharge, a large amount of displacement and discharge current is required. Hence, it is necessary to use the switches that can cope with high peak and root mean square (RMS) currents, which means a high cost driving system [19].

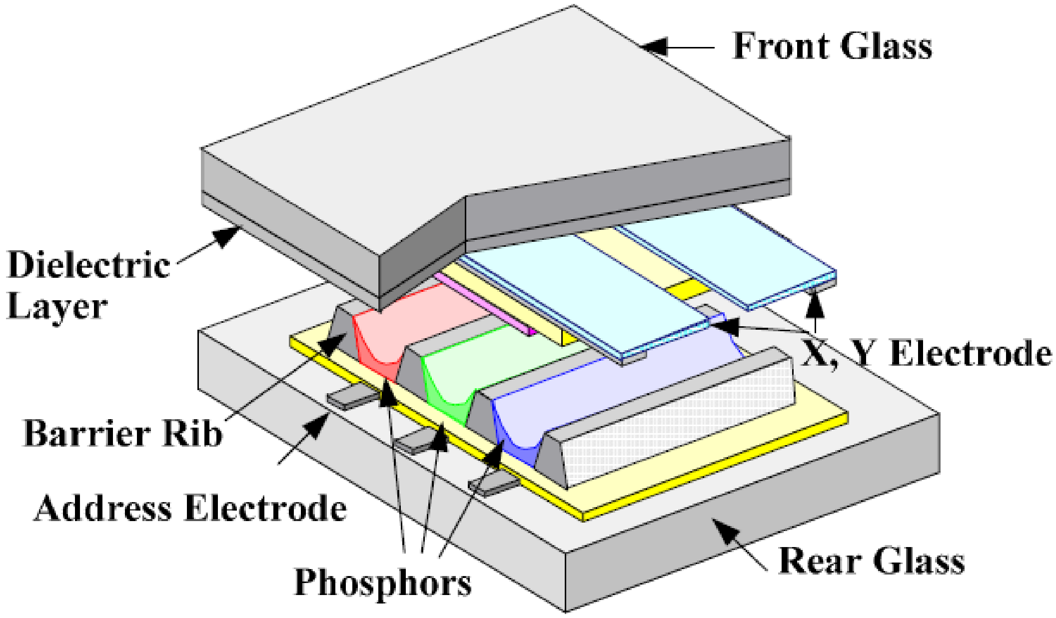

Figure 2.4. A schematic diagram showing the structure of the three-electrode AC plasma display [19].

Address Display period Separation (ADS) scheme as illustrated in Figure 5 that is a commonly used driving method for commercialized plasma display TV sets. In the ADS scheme, there are 9–11 subfields in one TV field of 1/60 or 1/50 second, and one subfield is divided into three operational periods such as reset, scan (or address), and sustain. Since the ADS scheme requires three different operations, conventional plasma display panel (PDP) schemes have three different circuit blocks corresponding to each operation [19]. For the sustain operation, a half bridge structure with energy recovery circuits (ERC) of the Weber type, which is based on an LC series resonance between an inductor and a panel capacitor, is typically used [19]. The ramp reset is widely adopted, which initializes RGB cells to have the same wall charge conditions by a weak gas regardless of the previous on/off state of cells. In the address period, scanning pulses from scan ICs are sequentially applied to the Y electrodes, and data pulses are given to the cells to be addressed while the scan switch Ysc is turned on to offer a negative scan voltage [19]. A circuit schematic for the panel driving system is shown in Figure 2.5.

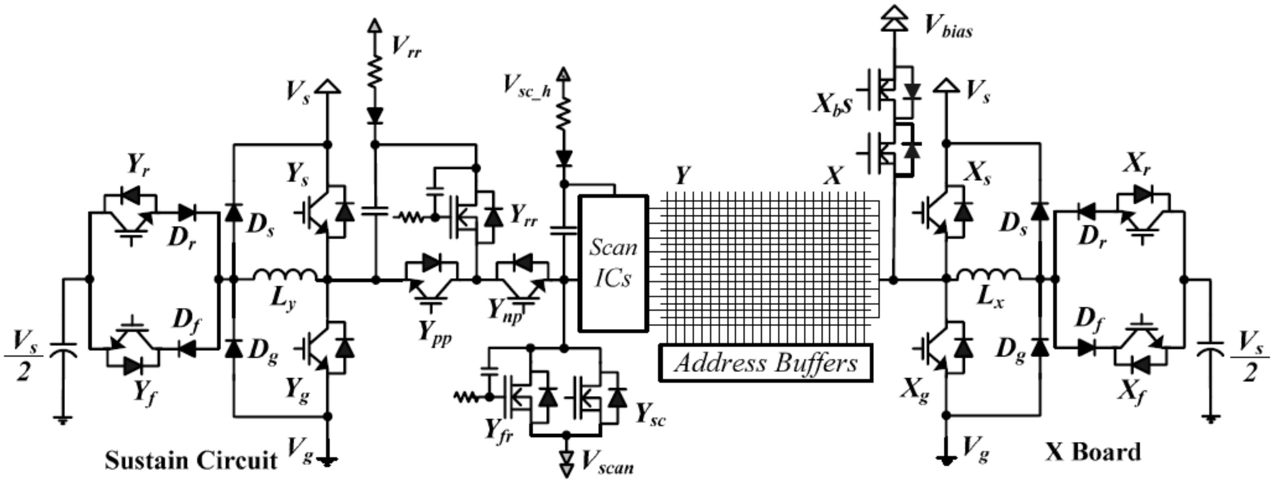

Figure 2.5. A schematic showing a PDP driving system [19].

Advantages of plasma display technology are the possibility of producing very large and thin screen, and very bright image and a wide viewing angle. Contrast ratios for plasma displays are as high as 30,000:1, which is a significant advantage of plasma technology over most other display technologies other than LED [19]. However, just like any other technology, plasma display technology has its challenges. Each cell on a plasma display has to be precharged before it is illuminated so that the cell would respond quickly enough. Due to precharging, the cells cannot achieve a true black [19]. Also, with phosphor-based electronic displays, the phosphor compounds, which emit the light, lose their capacity to emit light with use, which causes burn in [19]. When a group of pixels are run at high brightness for an extended period of time, a charge build-up in the pixel structure occurs, which results in a ghost image [19].

2.2.1 Current Trends in Plasma Technology

The size of plasma display has been one of the key advantages that attract electronic consumers to them. However, the complex and expensive circuitry that is involved in this technology is a major downside. Thus, most recent researchers and plasma manufacturers have been focused on reducing this aspect of plasma displays. Pioneer, Samsung and Panasonic have recently come up with the latest plasma display technology. Pioneer has developed a 50-inch plasma TV. The KURO PDP-5010FD is the best in cinematic image quality. The colors are rich and well-saturated, with great black levels [20]. The Pioneer TV is also packed with features, and an anti-glare screen coating helps reduce shine. The big downside is cost compared to other plasma TV sets [20]. The latest Samsung's 50-inch plasma HDTV has a great blend of image quality and value. Colors in Samsung

PN50A550 are very accurate, and video processing is one of the best. However, Top rated Pioneer and Panasonic plasma TVs have slightly deeper blacks [20]. Like most plasma TVs, the Samsung PN50A550 has a reflective screen, but reports say that glare is worse than most, which could pose a problem in bright rooms [20]. Panasonic's best 46-inch plasma TV when it comes to color accuracy, shadow detail and screen uniformity rank among the best [20].

2.3 LED Displays

In LED displays every pixel consists of 3 LEDs that are of the colors red, green, and blue, normally formed in a shape of a square as shown in Figure 2.6.a. These pixels are spaced evenly apart and are measured from center to center for absolute pixel resolution. There are two types of LED panels conventional, and surface mounted device panel (SMD) panels. Conventional panels use discrete LEDs (individually mounted LEDs) and are usually used for outdoor displays and sometimes indoor. Most indoor screens on the market are built using SMD technology that has a minimum brightness of 600 candelas per square meter. SMD technology is currently reaching the outdoor market as well, but under high ambient-brightness conditions, higher brightness may be required for visibility. Minimum of 2,000cd/m² is required in most for outdoor use, whereas higher brightness types of up to 5,000cd/m² cope better with direct sunlight on the screen. An SMD pixel also consists of red, green, and blue diodes mounted on a chipset, which is then, mounted on the driver PC board as shown in Figure 2.6.a and 2.6.b. The individual diodes are very small and are set very close together. The difference is that the maximum viewing distance is reduced by 25% from the discrete LED display with the same resolution [21].

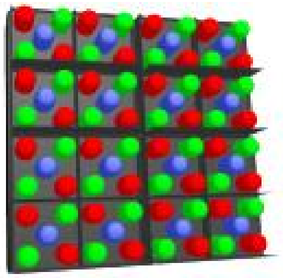

(a)

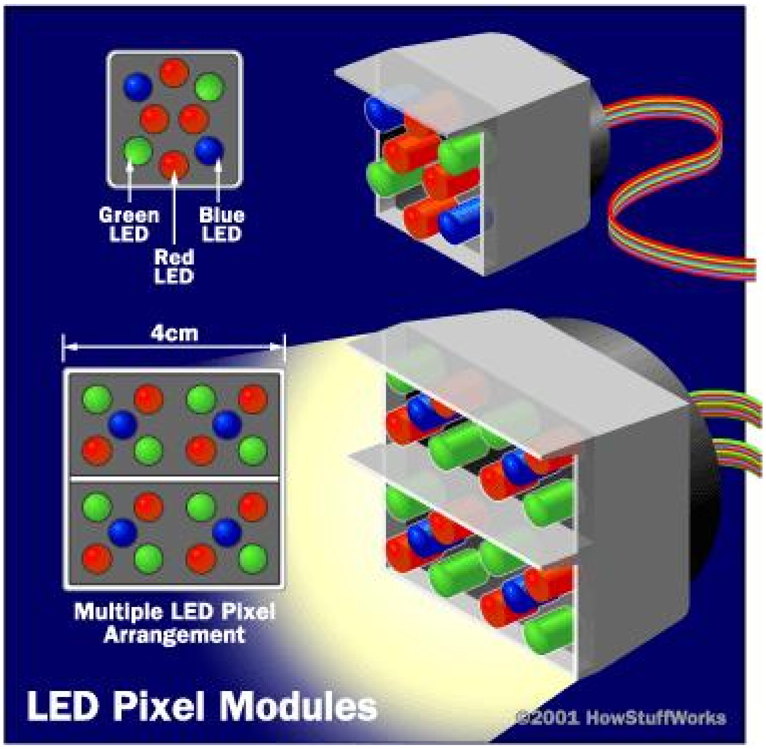

(b)

Figure 2.6 A schematic picture showing (a) 4x4 LED display matrix (b) LED pixel Modules [22].

The first recorded flat panel LED television screen was developed in 1977 by J. P. Mitchell in 1977 [21]. The modular, scalable display array was initially enabled by hundreds of MV50 LEDs and a newly available TTL (transistor transistor logic) memory addressing circuit from National Semiconductor [21]. In Anaheim May 1978, at the 29th Engineering Exposition organized by the Science Service in Washington D.C. the 1/4 inch thin flat panel prototype was displayed and a related scientific paper was presented. However, efficient blue LEDs were missing in order to develop a color display which they did not emerge until the early 1990s completing the desired RGB color triad [21]. In the 1990s, LEDs with high brightness colors progressively developed allowing new innovations for such as huge video displays for billboards and stadiums [21].

Using LEDs for displays has many advantages. LEDs can emit light of an intended color, which is more efficient and less costly than the use of color filters that traditional lighting methods require. In order to display a moving image frequent on-off cycling is required; LEDs are ideal for use in such applications because of the fast response time of LEDs. LEDs have a very fast response time which is its advantage over other display technologies such as LCD and Plasma. LEDs light up very quickly. A typical red LED will achieve full brightness in microseconds. LEDs can be dimmed very easily either by Pulse width modulation or lowering the forward current. Saving power or achieving an apparent higher brightness for a given power input is also feasible when pulse width or duty cycle modulated. Furthermore, LEDs mostly fail by dimming over time, rather than the abrupt burn out of incandescent bulbs. LEDs can have a relatively long useful life estimated to be 35,000 to 50,000 hours where fluorescent tubes, typically, are rated at about 30,000 hours, and incandescent light bulbs at 1,000–2,000 hours [21]. LEDs, being solid state components, are difficult to damage with external shock. They can also be very small and are easily mounted onto printed circuit boards.

On the other hand, LED displays are currently more expensive than more conventional lighting technologies. Most of its expense partially stems from the relatively low lumen output and the drive circuitry and power supplies needed. LED performance largely depends on the ambient temperature of the operating environment. Over driving the LED in high ambient temperatures may result in overheating of the LED package, eventually leading to device failure [21]. Adequate heat sinking is required to maintain long life [21]. Since white LEDs emit much more blue light than conventional outdoor light sources such as high pressure sodium lamps, the strong wavelength dependence of Rayleigh scattering means that LEDs can cause more light pollution than other light sources. It is, therefore, very important that LEDs are fully shielded when used outdoors [21].

LEDs have become very popular in certain applications such as display boards because they offer significant advantages in brightness, energy efficiency and product lifetime over traditional illumination choices.

2.3.1 Recent Developments in LED Displays

LED display industry has started in the early 1990s and has rapidly and steadily developed. Each year, the LED display market shows a growth of 15-20% [23]. There is a high demand for LED displays especially for outdoor screens such as sign displays and billboards, and also for indoor screens. With the improving LED technology, LED displays have developed to meet high industry standards when it comes to color variability, quality, viewing angle, resolution, etc. Therefore, competitors have found it very critical to introduce more features that extend even beyond high image quality. For example, LED display market is headed towards mobile displays in some companies such as YESCO and GOVISION. Water proof and flexible LED displays are being produced by Shenzhen Cheng Guangxing Industrial Development Co. and BaoChengXin Opto-electronic Technologies Co. Technology developments of LED screen in the near future will target many issues such as improvement of performance indexes color, brightness, angle of view, etc. of LED screen, development of color and gray degree control, improving color regenerating ability and visual quality of a full color screen, and constant current driving control technology. Development of the system technology will also be a target for future developments such as applying automatic checking and remote control [23]. Improving the product structure technique is also vital for instance LED's level, heat dissipation and protection degree. Definitely, there is always room for improving the overall stability and reliability of the display [23].

CHAPTER 3

UNDERSTANDING COLORS

3.1 Definitions of Basic Colorimetric Concepts

Psychological concepts related to color perception as defined by the authors in [24]:

Light: is an aspect of radiant energy of which a human observer is aware through the visual sensations that arise from the stimulation of the retina of the eye by the radiant energy.

Color: is an aspect of visual perception by which an observer may distinguish differences between structure free fields of view of the same size and shape, which may be caused by differences in the spectral composition of the radiant energy concerned in the observation.

Hue: is the attribute of a color perception.

Saturation: is the attribute of a color perception determining the degree of its difference from the achromatic color perception most resembling it.

Chromaticness: is the attribute of a color perception composed of the attributes hue and saturation.

Brightness: is the attribute of a color perception ranging from very dim

	to very bright.
Lightness:	is the attribute of a color perception ranging for light-diffusing objects from black to white, and ranging for regularly transmitting objects from black to perfectly clear.

Psychophysical Concepts Related to Color-Matching as defined by the authors in [24]:

Color:	is that characteristic of a visible radiant energy by which an observer may distinguish differences between structure free fields of view of the same size and shape, which may be caused by differences in the spectral composition of the radiant energy concerned in the observation.
Color stimulus:	is radiant energy of given intensity and spectral composition, entering the eye and producing a sensation of color.
Spectrum color:	is the color of monochromatic light, that is, light of a single frequency.
Achromatic color:	is a color of a light chosen because it usually yields an achromatic color perception under the desired observing conditions.
Primary colors:	are the colors of three reference lights by whose additive mixture nearly all other colors may be produced.
Tristimulus values:	are the amounts of the three reference lights required to give by additive mixture a match with the color or light considered.

Color–matching functions:	are the tristimulus values, with respect to 3 primary colors, of monochromatic lights of equal radiant energy, regarded as functions of the wavelength.
Chromaticity coordinates:	are the ratios of each tristimulus value of the color of their sum.
Dominant wavelength:	is the wavelength of the spectrum color that, when additively mixed in suitable proportions with a specified achromatic color, yields a match with the color considered.

Basic photometric concepts and units as defined by the authors in [24]:

Luminous flux:	is the quantity derived from radiant flux by evaluating the radiant energy according to its action upon a selective receptor, the spectral sensitivity of which is defined by a standard relative luminous efficiency function.
Lumen (lm):	the unit of luminous flux defined by the luminous flux emitted within unit solid angle by a point source having a uniform luminous intensity of one candela.
Luminous intensity:	is the quotient of the luminous flux emitted by a point source in an infinitesimal cone containing the given direction, by the solid angle of that cone.
Candela (cd):	the unit of luminous intensity.

3.2 The Eye and Perception

The external stimulus is the visible radiant flux incident on the eye. The ability of the human eye to distinguish colors is based on the varying sensitivity of different cells in the retina (rods and cones) to different wavelengths of visible light.

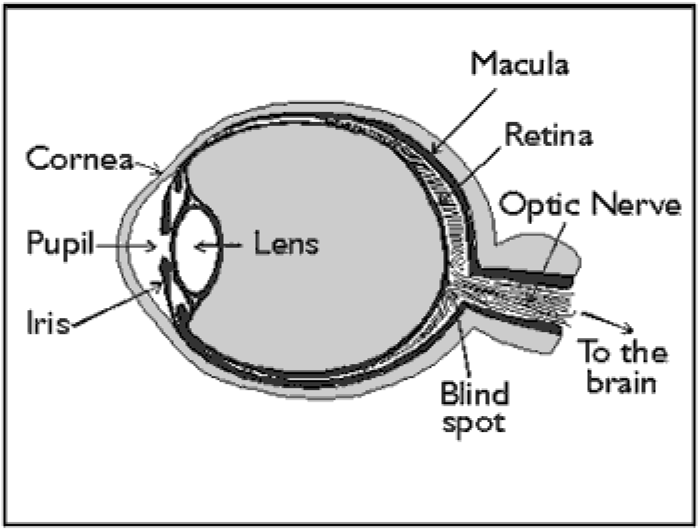

Figure 3.1. A schematic diagram showing different parts of the eye [25].

The vision is an optical process up to a certain point, the critical point. This point is reached when the radiant flux, originated from the external stimulus, is absorbed by the light sensitive visual pigments of the retinal end organs the rods and the cones [24]. The internal stimulus is defined as the quality and intensity of the radiant flux at each point occupied by a visual pigment.

There are two different sensors in the retina: the cones which are sensitive to the colors concentrated in the fovea (macula), as shown in Figure 1, and the rods which are sensitive to low levels of light. Cones are coated with pigments that are sensitive to different wavelengths. There are about seven million cones in every eye; each of which is connected with single neuron. However, rods are grouped in bunches and every bunch is connected to a neuron. There are about 120 million Rods in each eye. A schematic diagram in Figure 3.2 pictorially depicts the nature of the retina.

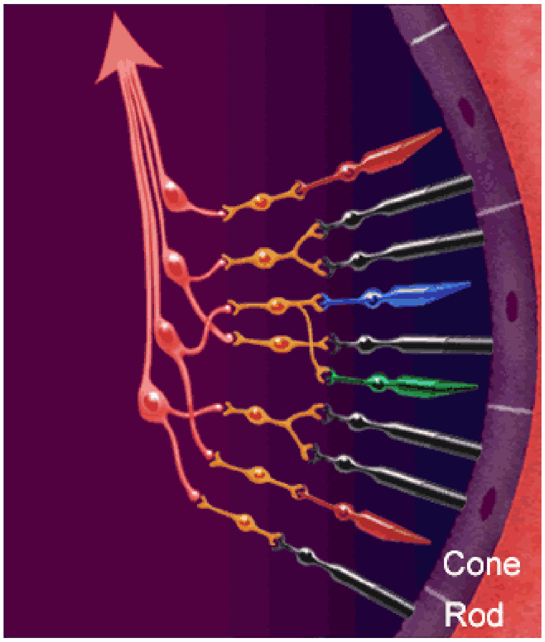

Figure 3.2. A schematic diagram showing rods and cones [26]

No matter how complex light is, the composition of wavelengths is reduced to three color components by the eye which are red, green and blue. For each location in the visual field, the three types of cones yield three signals based on the extent to which each is stimulated. These values are called tristimulus values. The "green" and "red" cones are mostly packed into the fovea centralis. Approximately, 64% of the cones are sensitive to red, 32% green sensitive, and about 2% are blue sensitive [24]. The "blue" cones have the highest sensitivity and are mostly found outside the fovea. A schematic diagram shoeing response of the retina versus wavelength of light is shown in figure 3.3. These curves are obtained by measurement of the absorption by the cones, but the relative heights for the three types are set equal for lack of detailed data. There are fewer blue cones, but the blue sensitivity is comparable to the others, so there must be some boosting mechanism [24]. In the final overall visual perception, the three colors appear comparable. Light may be precisely characterized by giving the power of the light at each wavelength in the visible spectrum, and this function is called the spectral power distribution (SPD).

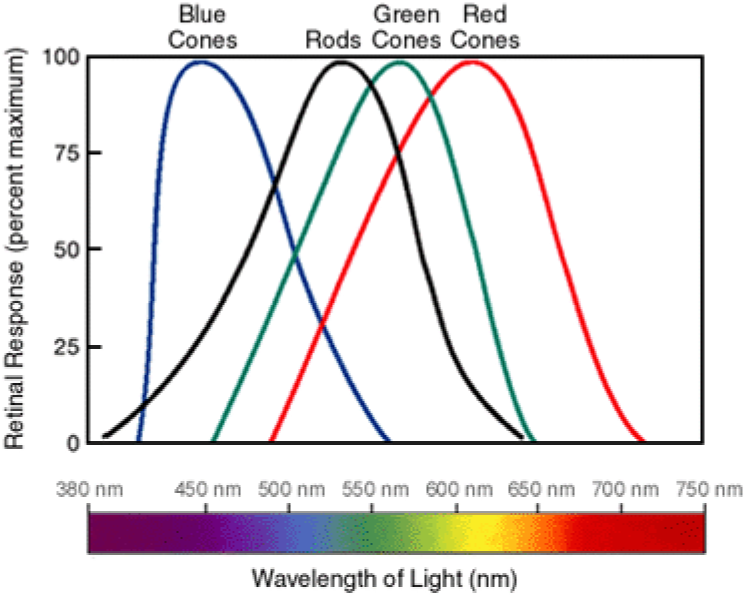

Figure 3.3. A schematic diagram showing the different response curves for cones and rods [27].

3.2.1 Photoptic and Scotoptic Vision

Scotopic vision is the eye's nighttime sensitivity; at night the vision shifts toward the blue end of the visible light. It is at its peak at 507 nm and falls to 10^{-4} at 340 and 670 nm as shown in figure3.4. The eye's daytime sensitivity is called photopic vision which shifts toward the green end of the visible light with a peak at 555 nm. It falls to 10^{-4} at 380 and 750 nm. In other words, human vision is more sensitive to blue at night; where it is more sensitive to green in day vision.

The scotopic vision is primarily rod vision, and the photopic vision includes the cones. The response curve of the eye, shown in Figure 3.4, together with the spectral power distribution of a luminous object determines the perceived color of the object. The curves represent the spectral luminous efficacy for human vision. The lumen is defined such that the peak of the photopic vision curve has a luminous efficacy of 683 lumens/watt. The efficacy of the scotopic vision equals the efficacy of the photopic value at 555 nm [27]. This was done by taking a person with normal vision, and having them compare the brightness of monochromatic light at 555 nm, where the eye is most sensitive, with the brightness of another monochromatic source of differing wavelength. To achieve a balance, the brightness of the 555 nm source was reduced until the observer felt that the two sources were equal in brightness. The fraction by which the 555 nm source is reduced measures the observer's sensitivity to the second wavelength [27].

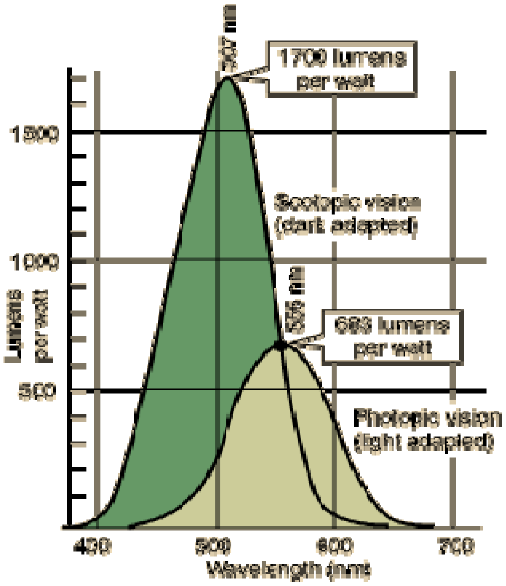

Figure 3.4. A schematic diagram of the spectral luminous efficacy for human vision [27]

3.3 The Nature of Color

Color is a visual perceptual property that steams from the spectrum of light, which is the distribution of light energy versus wavelength, interacting with the light receptors of the eye that is featured by spectral sensitivities [28]. Visible light is when the wavelength is within the visible spectrum which is the range of wavelengths humans can perceive, approximately from 380 nm to 740 nm. Table 1 shows the colors that can be produced by visible light of a single wavelength only, the pure spectral or monochromatic colors. Different light sources emit light at many different wavelengths; a source's spectrum represents the intensity distribution at each wavelength. The spectrum of light arriving at the eye from a given direction determines the color sensation in that direction.

Table 3.1. The colors of the visible light spectrum [26]

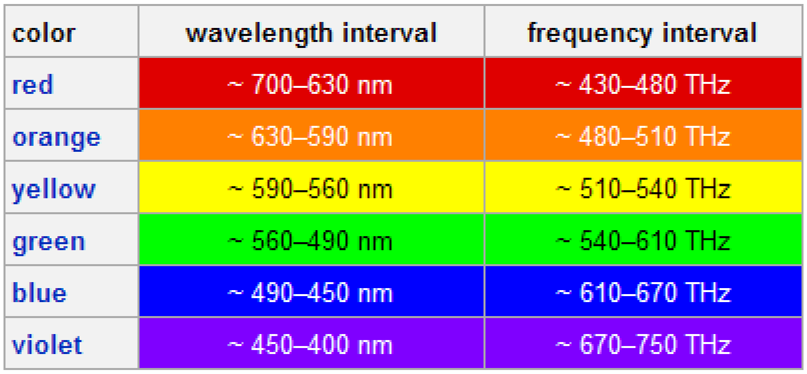

color	wavelength interval	frequency interval
red	~ 700–630 nm	~ 430–480 THz
orange	~ 630–590 nm	~ 480–510 THz
yellow	~ 590–560 nm	~ 510–540 THz
green	~ 560–490 nm	~ 540–610 THz
blue	~ 490–450 nm	~ 610–670 THz
violet	~ 450–400 nm	~ 670–750 THz

A common list identifying six main bands: red, orange, yellow, green, blue, and violet; their wavelengths and frequencies are presented in Table 3.1. Newton's conception included a seventh color, indigo, between blue and violet. The intensity of a spectral color may alter its perception considerably; for example, a low-intensity orange-yellow is brown, and a low-intensity yellow-green is olive-green.

3.4 Color Interpreted by the Brain

3.4.1 Reproduction of Colors

Light sources are either monochromatic or mixtures of various wavelengths of light. Some monochromatic colors can be reproduced as combination of other light sources. Orange, for instance, is a monochromatic color that is also obtained as a combination of red and green light. In Newton’s experiment [29], he investigated what happens when mirrors are placed so as to superimpose on a white screen, two beams of monochromatic light from different regions of the spectrum. He found that a different third color was seen. This intermingled light was not monochromatic, because Newton found that when it passed through another prism two beams emerged with the two original monochromatic colors. From these observations Newton deduced that the notion of color applies to the perception we have, not to the light itself [29]. Two different light spectra which have the same effect on the three color receptors in the human eye will be perceived as the same color. This is exemplified by the white light that is emitted by fluorescent lamps, which typically has a spectrum consisting of a few narrow bands, while daylight has a continuous spectrum but human beings perceive them as very similar. The human eye cannot tell the difference between such light spectra just by looking into the light source, although reflected colors from objects can look different, because the absorption behavior of the object may be different for different parts of the spectrum.

3.4.2 Luminous Flux

Luminous flux is a weighted average of the Radiant Flux in the visible spectrum. It is a weighted average since the human eye responds unequally (it has different sensitivity) to the different visible wavelengths [24]. For conversion of Radiant Flux to Luminous Flux at any wavelength a weighing factor (V_λ) has to be taken into consideration; this weighing factor is the luminance efficacy, which is the response of the eye as a function of frequency. Further discussion is in section 3.3.

3.4.3 Matching Function

Given that Q is the vector representing a particular color and R, G, and B are the unit vectors representing three fixed primaries, then the vector equation

$$Q = \mathit{R}\mathrm{R} + \mathit{G}\mathrm{G} + \mathit{B}\mathrm{B} \tag{3.4.1}$$

states that the given color is matched by a linear combination of quantities R, G, B of the respective primaries [29]. The scalar multipliers *R, G*, and *B* are the tristimulus values of the given color with respect to the set of primaries R, G, and B. This three dimensional vector space is called the *RGB* tristimulus space. Given that P_λ is the spectral energy distribution of color Q, then Q can be considered as an additive mixture of colors whose corresponding stimuli are the monochromatic components P_λ of the original stimulus out of which the color Q is composed. If $R_\lambda\, d\lambda$, $G_\lambda\, d\lambda$, and $B_\lambda\, d\lambda$ are the tristimulus values of $Q_\lambda\, d\lambda$ and *R, G, B* are those of Q, then [24]

$$Q = \int_\lambda Q_\lambda\, d\lambda \tag{3.4.2}$$

and

$$R = \int_\lambda R_\lambda\, d\lambda, \quad G = \int_\lambda G_\lambda\, d\lambda, \quad B = \int_\lambda B_\lambda\, d\lambda \tag{3.4.3}$$

Using Equation 3.4.2 and 3.4.3, Equation 3.4.1 can be written as

$$Q = \int_\lambda Q_\lambda\, d\lambda = R \int_\lambda R_\lambda\, d\lambda + G \int_\lambda G_\lambda\, d\lambda + B \int_\lambda B_\lambda\, d\lambda \tag{3.4.4}$$

Given that $\overline{q}_\lambda$ is the tristimulus value of spectrum for the color Q, one can conclude that the corresponding stimuli are monochromatic and contain the same constant radiant flux. These values are denoted by $\overline{r}_\lambda$, $\overline{g}_\lambda$, $\overline{b}_\lambda$ which represent the color matching properties of the human eye in the particular primary system, R, G, B, and are called color matching functions as shown in Figure 3.5. Therefore, the set of equations in (3.4.2) and (3.4.3) above can be rewritten as follows:

$$Q=\int_\lambda P_\lambda\ \bar{q}_\lambda\ d\lambda \qquad (3.4.5)$$

$$R=\int_\lambda P_\lambda\ \bar{r}_\lambda\ d\lambda, \quad G=\int_\lambda P_\lambda\ \bar{g}_\lambda\ d\lambda, \quad B=\int_\lambda P_\lambda \bar{b}_\lambda\ d\lambda \qquad (3.4.6)$$

This implies that the tristimulus values *R, G, B*, the coefficients of the unit vectors R, G, B in the linear equation (3.4.1), can be represented as the multiplication of two amounts the spectral energy distribution and the matching function which adapts the radiant flux observed by the human eye to the corresponding, wave length dependent, luminance flux. In other words, *R, G*, and *B* are the weighted average of the spectral energy distribution. Thus, Q is the summation of the product of those weighted averages by the RGB unit vectors.

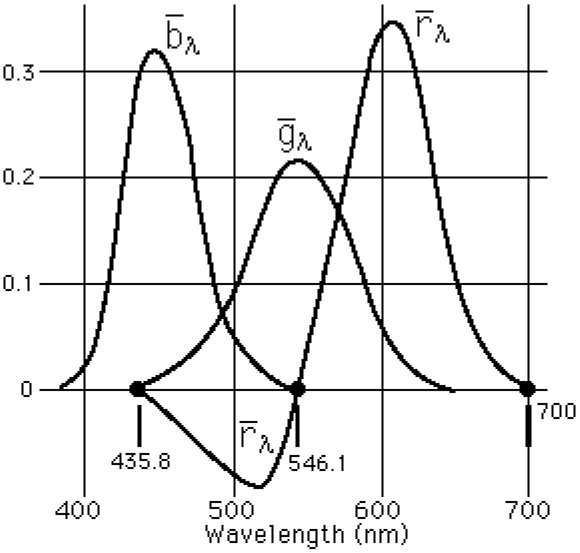

Figure 3.5. Color- matching functions, $\bar{r}_\lambda$, $\bar{g}_\lambda$, $\bar{b}_\lambda$ in the primary system R, G, B [27].

The color matching functions are based on 3 laws, Grassmann's laws of additive color mixture (1853), which state [29]:

1. Any four colors Q, R, G, and B are always linearly dependent. In other words, the following relationship must hold

   $$Q\mathrm{Q}+R\mathrm{R}+G\mathrm{G}+B\mathrm{B} = 0$$

   where the scalar multipliers, Q, R, G, B are not all 0.
2. The color of a mixture of colors Q and Q_1 is the same as that of a mixture Q and Q_2, if Q_1 matches Q_2, although the spectral energy distributions $\{P_{1\lambda}\, d\lambda\}$ and $\{P_{2\lambda}\, d\lambda\}$ of the color stimuli corresponding, respectively, to Q_1 and Q_2 may be different.
3. A continuous change in the spectral energy distribution $\{P_{\lambda}\, d\lambda\}$ of the color stimulus of color Q results in a continuous change of Q.

3.5 Color Spaces

A color space is a notation, by which we can quantify colors. There are many different color spaces that are used for different applications specifically in image processing. The choice of a color space can be a very important decision, which can largely influence the results of the processing [30]. Color spaces can be categorized in 3 different categories: human visual system (HVS) based color spaces, Application specific color spaces, and CIE color spaces.

3.5.1 HVS Color Spaces

The HVS based color spaces fall under three categories: the RGB color spaces, the opponent colors theory based color spaces, and the phenomenal color spaces. The RGB color space is the first attempt to simulate light in the human eye based on the HVS. The color is described with three components: R, G and B. The value of these components is the sum of the respective sensitivity functions S_λ and the light spectrums $R_\lambda\, d\lambda$, $G_\lambda\, d\lambda$, and $B_\lambda\, d\lambda$.

$$R= \int_\lambda S_\lambda R_\lambda\, d\lambda, \quad G= \int_\lambda S_\lambda G_\lambda\, d\lambda, \quad B= \int_\lambda S_\lambda B_\lambda\, d\lambda \tag{3.5.1}$$

The RGB color space is device dependent since the RGB values depend on the specific sensitivity function. Capturing, printing, and displaying devices are based on the RGB color space.

The German physiologist Ewald Hering proposed the opponent colors theory in the late 19th century [30]. He noted that certain hues were never perceived to occur together; for example, reddish-green or yellowish-blue are not visually possible, while all other combinations are possible such as bluish-green or reddish-yellow. Researchers found out that there is a layer in the HVS that converts the RGB values from the cones into an opponent color vector. This vector has an achromatic component White-Black (WhBl) and two chromatic components Red-Green (RG) and Yellow-Blue (YeB) [30]. The transformation between RGB values and RG, YeR, and WhBl is done according to the following model:

$$RG = R - G$$

$$YeB = 2B - R - G$$

$$WhBl = R + G + B \tag{3.5.2}$$

Isaac Newton [24] arranged colors in a circle, called the Newton’s color circle, which belongs to the phenomenal color spaces. This uses the attributes of hue and saturation for describing colors as shown in Figure 3.6, where the hue is represented by the angle, saturation by the radius, and value or luminance by the hypotenuse formed by the line that extends on the surface of the cone from zero brightness, the pointy part of the cone. Naturally, the human brain tends to organize colors by hue, saturation and brightness. This is the mind's representation of colors - the highest level in human visual processing [30]. Hue is the attribute which tells us whether the color is red, green, yellow, blue, purple, etc which is represented by the angle. Saturation is the level of non-whiteness which is represented by the radial length of the point from the center. Brightness is a measure of the intensity of light which is represented by the tangent of the cone. The Munsell color space is a phenomenal color space and an atlas of 1500 systematically ordered color samples. These samples are chosen in such a way that the steps are perceptually equal [30].

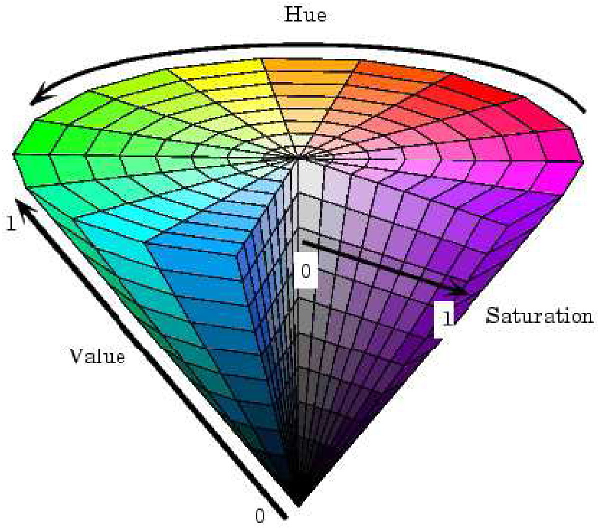

Figure 3.6 A schematic diagram representing the phenomenal color space [31]

HSV (hue, saturation, and value) color spaces are also phenomenal color spaces. They are a linear transformation from the RGB space. There are many of HSV spaces defined in literature [30]. In the following, one of the models used for HSV transformation is described below:

Saturation is presented as:

$$S = \frac{\max(R,G,B) - \min(R,G,B)}{\max(R,G,B)} \tag{3.5.3}$$

Value is defined as:

$$V = \max(R,G,B) \tag{3.5.4}$$

Hue is defined as:

$$H = 5 + B' \quad \textit{when} \quad \mathrm{R} = \max(R,G,B), G = \min(R,G,B)$$

$$H = 1 - G' \quad \textit{when} \quad \mathrm{R} = \max(R,G,B), G\ 6\!= \min(R,G,B)$$

$$H = R' + 1 \quad \textit{when} \quad G = \max(R,G,B), B = \min(R,G,B)$$

$$H = 3 - B' \quad \textit{when} \quad G = \max(R,G,B), B\ 6\!= \min(R,G,B)$$

$$H = 3 + G' \quad \textit{when} \quad B = \max(R,G,B)$$

$$H = 5 - R' \ \text{otherwise} \tag{3.5.5}$$

where

$$R' = \frac{\max(R,G,B) - R}{\max(R,G,B) - \min(R,G,B)}$$

$$G' = \frac{\max(R,G,B) - G}{\max(R,G,B) - \min(R,G,B)}$$

$$B' = \frac{\max(R,G,B) - B}{\max(R,G,B) - \min(R,G,B)}$$

then H is converted to degrees by multiplying by 60.

Phenomenal color spaces do not take into account the human perception. There is also a bad correlation between the computed and the perceived lightness [30]. Thus, using phenomenal color spaces becomes inaccurate in many applications.

3.5.2 Application Specific Color Spaces

The two main applications, where the usage of color spaces is essential, are printing and television. In printing, subtractive mixing of colors is used, which is a way to produce colors by selectively removing a portion of the visual spectrum. The CMY (Cyan Magenta Yellow) color space is a subtractive color space and is mainly used in printing applications [30]. It is perceptually non-linear. The three components represent three reflection filters. There is also the CMYK color space, where the fourth component K represents the amount of black ink [30]. There are two types of transformation to the CMYK color space, a simple one and a more complicated one that uses complicated polynomial arithmetic or three-dimensional interpolations of lookup tables.

Simple transformation from RGB to CMY color space is given by:

$$C = 1 - R$$

$$M = 1 - G$$

$$Y = 1 - B \qquad (3.5.6)$$

Transformation from $C'\ M'\ Y'$ to the *CMYK* color space is given by:

$$K = \min\ (C, M, Y)$$

$$C = \frac{(C' - K')}{(1 - K')}$$

$$M = \frac{(M' - K')}{(1 - K')}$$

$$Y = \frac{(Y' - K')}{(1 - K')} \tag{3.5.7}$$

The YUV color space is one of the color spaces used for TV application. The RGB signals are encoded in the YUV space with the following equations:

$$Y = 0.299R + 0.587G + 0.114B$$

$$U = -0.147R - 0.289G + 0.437B = 0.493\,(B - Y)$$

$$V = 0.615R - 0.515G - 0.1B = 0.877\,(R - Y) \tag{3.5.8}$$

The YUV space can be transformed in a phenomenal color space, with Y representing the V (value) component, as:

$$\begin{aligned} H_{UV} &= \tan^{-1}\left(\frac{V}{U}\right) \\ S_{UV} &= \sqrt{U^2 + V^2} \end{aligned} \tag{3.5.9}$$

3.5.3 The CIE Color Spaces

The CIE, the international Commission on Illumination, laid down the CIE 1931 standard colorimetric observer in 1931. This is the data on the ideal observer on which all colorimetric is based [30]. As shown in equation 3.4.1, colors can be expressed as vectors that are geometrically represented as a three-dimensional vector space where R, G, and B are the axis, color of vector Q is a point with the coordinates of *R*, *G*, and *B* [24]. The unit plane that satisfies the condition R+G+B = 1 is considered as the two dimensional (r, g) chromaticity diagram as shown in Figure 3.7.

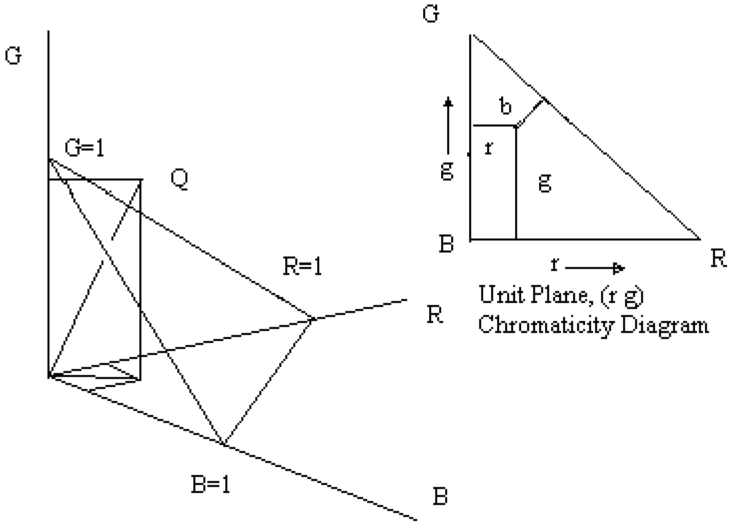

Figure 3.7 A schematic diagram showing the three-dimensional RGB vector space and the (r g) chromaticity diagram.

The following set of equations is used for the transformation of the tristimulus values *R, G, B* to the chromaticity coordinates r, g, b:

$$r = \frac{R}{R+G+B}, \quad g = \frac{G}{R+G+B}, \quad b = \frac{B}{R+G+B}, \tag{3.5.10}$$

The CIE standardized the XYZ values as tristimulus values that can describe any color that can be perceived by an average human observer. This color space is defined by the color matching functions $\bar{x}_\lambda, \bar{y}_\lambda, \bar{z}_\lambda$ [24]. These values, which were experimentally obtained, are tabulated with the corresponding chromaticity coordinates $x_\lambda, y_\lambda, z_\lambda$. The

CIE color space chromaticity presented in Figure 3.8 is showing the color gamut for the (x y) chromaticity coordinates; the wavelengths are denoted by the values surrounding the color gamut.

The tristimulus values X, Y, and Z are obtained by the summation of the spectral distribution of its radiant flux {P_λ dλ} as shown in the following equations:

$$X = k\sum_{\lambda} P_{\lambda}\bar{x}_{\lambda}\Delta\lambda$$

$$Y = k\sum_{\lambda} P_{\lambda}\bar{y}_{\lambda}\Delta\lambda$$

$$Z = k\sum_{\lambda} P_{\lambda}\bar{z}_{\lambda}\Delta\lambda \tag{3.5.11}$$

where the color matching functions $\bar{x}_{\lambda}, \bar{y}_{\lambda}, \bar{z}_{\lambda}$ are obtained from the tabulated data, and k is a normalizing factor. After obtaining the tristimulus values, the chromaticity coordinates are obtained by using the following equations:

$$x = \frac{X}{X+Y+Z}$$

$$y = \frac{Y}{X+Y+Z}$$

$$z = \frac{Z}{X+Y+Z} \tag{3.5.12}$$

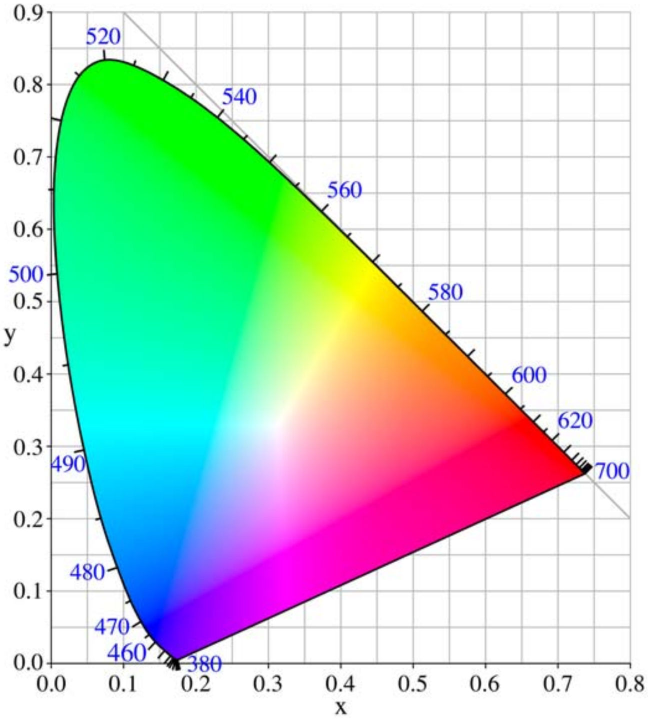

Figure 3.8 The CIE 1931 color space (x y)chromaticity diagram [27]

For any given stimulus, the transformation between r, g, b and x, y, z is given by the following set of equations:

$$x = \frac{0.49r + 0.31g + 0.2b}{0.66697r + 1.1324g + 1.20063b},$$

$$y = \frac{0.17697r + 0.8124g + 0.01063b}{0.66697r + 1.1324g + 1.20063b}, \tag{3.5.13}$$

$$z = \frac{0.0r + 0.01g + 0.99b}{0.66697r + 1.1324g + 1.20063b},$$

In 1976, the CIE introduced the color spaces CIELUV and CIELAB. Perceptual uniformity is what distinguishes the CIELUV and CIELAB color spaces. Thus, any change in value corresponds approximately to the same perceptual difference over any part of the space [30]. The CIELUV space was specifically designed for emissive colors that are found in various applications such as photography or computer graphics rendering program. For the 'a' value, CIELAB uses a red/green axis and a blue/yellow axis for the 'b' value [32]. This model is very similar to the way the human optic system works. CIELUV uses chromaticity (saturation) for the 'u' value and hue angle for the 'v' value. The CIELUV space uses the CIE 1976 ($u^{'}$ $v^{'}$) chromaticity diagram, shown in Figure 3.9, where L, U, V are the tristimulus values that correspond to the ($u^{'}$ $v^{'}$) coordinates; however, CIELAB uses a modification of Adam's chromatic-value diagram, as shown in Figure 3.10, where L, A, B are the tristimulus values that correspond to the (a^{*} b^{*}) coordinates [32].

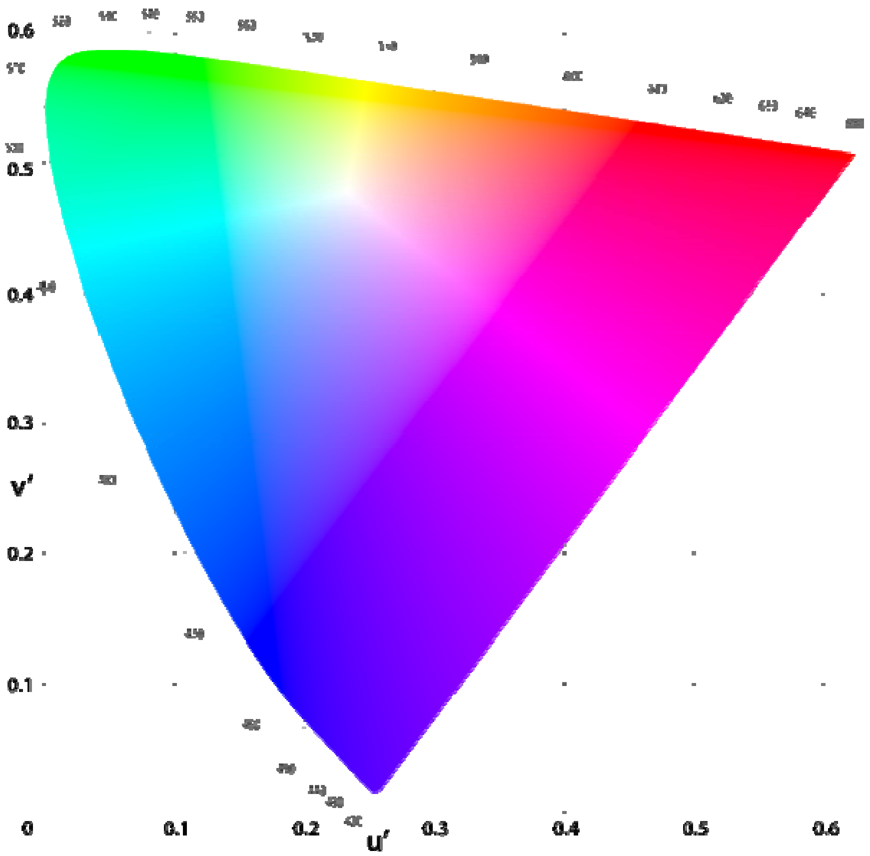

Figure 3.9 The CIE 1976 color space ($u^{'}$ $v^{'}$) chromaticity diagram [28].

In the CIELAB model presented in Figure 3.10, differences in colors perceived, correspond to measured linear colorimetric distances. The ‘a’ axis extends from green (-a) to red (+a) and the ‘b’ axis from blue (-b) to yellow (+b). The brightness (L) increases from the bottom to the top of the spherical model [33].

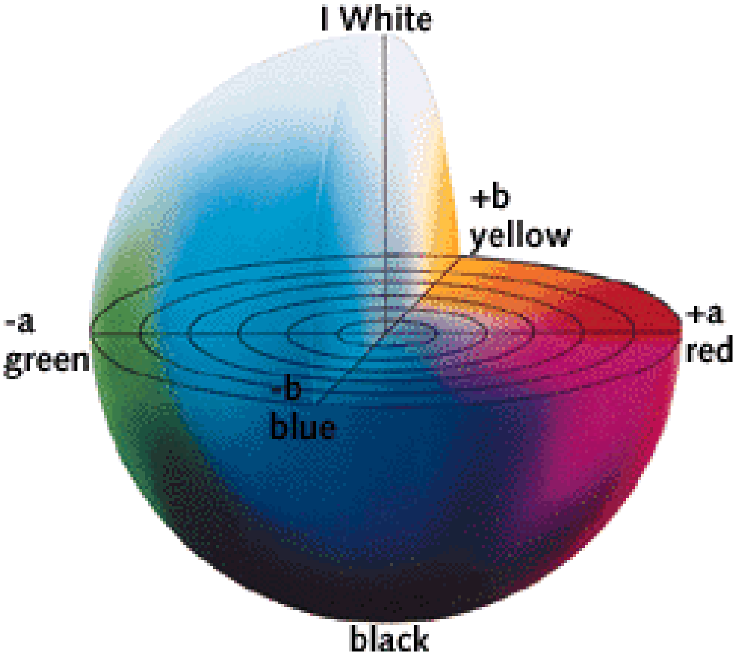

Figure 3.10 The CIELAB chromaticity diagram ($a^* \; b^*$) plane [33].

The transformation from CIE XYZ to CIELUV is performed with the following equations

For $\frac{Y}{Y_n} > 0.01$

$$L^* = 116\left(\frac{Y}{Y_n}\right)^{\frac{1}{3}} - 16$$

$$u^* = 13L^*\left(u' - u'_n\right) \tag{3.5.14}$$

$$v^* = 13L^*\left(v' - v'_n\right)$$

else

$$L^{*} = 903.3\left(\frac{Y}{Y_n}\right) \tag{3.5.15}$$

where

$$u^{'} = \frac{4X}{X + 15Y + 3Z}$$

$$u_n^{'} = \frac{4X_n}{X_n + 15Y_n + 3Z_n} \tag{3.5.16}$$

$$v^{'} = \frac{9Y}{X + 15Y + 3Z}$$

$$v_n^{'} = \frac{9Y_n}{X_n + 15Y_n + 3Z_n}$$

The transformation from CIE XYZ to CIELAB is performed with the following equations

$$L^{*} = 116\left(\frac{Y}{Y_n}\right)^{\frac{1}{3}} - 16$$

$$a^{*} = 500\left[\left(\frac{X}{X_n}\right)^{\frac{1}{3}} - \left(\frac{Y}{Y_n}\right)^{\frac{1}{3}}\right] \tag{3.5.17}$$

$$b^{*} = 200\left[\left(\frac{Y}{Y_n}\right)^{\frac{1}{3}} - \left(\frac{Z}{Z_n}\right)^{\frac{1}{3}}\right]$$

where L^{*} is the lightness scale, which depends only on Y the luminance value, for both color spaces CIELUV and CIELAB; The tristimulus values X_n, Y_n, Z_n are those of the nominally white object-color stimulus [30].

CHAPTER 4

THEORETICAL AND PRACTICAL MODELING OF RGBW PIXEL BASED LED DISPLAY

4.1 Introduction of the New Pixel with a White LED

Even though, the rapid development in solid state technology has witnessed advancements in high power LED obtaining on average 150 lumen/ Watt [34], efficiency of LED displays could be further improved by introducing a white LED to the pixel. In addition, the introduction of the white LED is expected to improve picture quality of LED displays. There are several approaches using LEDs to achieve white light. One approach is to use a blue or UV LED to excite one or more phosphors to produce white light [35] [36]. Another approach is to use RGB LEDs to give white light. A key challenge for RGB LEDs is to maintain the desired white point within acceptable tolerances. This arises from the significant spread in lumen output and wavelength of manufactured LEDs, and the changes in LED characteristics that occur with temperature and time. Maintaining the desired white point can only be achieved with feedback schemes to control the relative contributions of red, green, and blue to the white light [36]. This paper focuses on the first method of white light generation in which a blue LED is used. The traditional method of using LED light source composed of RGB LEDs is modified to include a white LED. The white LED will be turned on to the level of the appropriate luminance when all three RGB are turned on in order to produce a certain color. The luminance of the white LED will be decided based on the minimum luminance flux (which takes into account human eye response) of the RGB and tristimulus values, which are the amounts of the reference lights necessary for the additive mixture to provide a close match to the light considered [24].

By introducing the white LED into the pixel, usage of the green LED will be reduced, which is the least efficient. Also, usage of red and blue LEDs will be reduced which results in a life expectancy increase of the display on an average. Moreover, less complicated feedback control schemes for RGB LEDs will be needed in order to maintain achromatic point (AP) since pure white light is used to achieve the white point resulting in more uniform white color point integration with the added benefits of a less complicated control circuitry. Based on a theoretical modeling and test measurements (using a prototype) for the new suggested method (RGBW), the advantages compared to the RGB LED display technology will be demonstrated.

4.2 Issues with RGB

Although RGB has the benefit of color variability, it also has some challenging issues such as: Color instability due to temperature changes and the variability in light output of nominally identical LEDs by over a factor of two, and the wavelength can vary by many nanometers due to aging differently and initial spread in the performance of the LEDs [36]. A study on thermal effects on RGB LED characteristics was reported in [35]. The study in [35] shows a 10% decrease in light output for every 100C increase in temperature for AlInGaP red LED 5% for InGaN green LED and 2% for InGaN blue

LED. It is also shown that as temperature increases the LED shifts towards longer wavelength. In [36], minimum perceptible-color-difference (MPCD) as an outcome of changes in light output of the individual LEDs, due to aging or manufacturing inconsistency, was studied and reported. Results show the calculated shift in the (u, v) color coordinates as a result of a change in the flux of the red, green, or blue LEDs.

4.3 Theoretical Analysis of the New RGBW Pixel

In this study, the classical pixel RGB is modified to include a white LED. In a frame, some pixels will have a certain intensity of white. In other words, certain hues can be modeled as the addition of a certain amount of white and some intensities of two of the three colors, R, G and B. For every pixel that has some amount of white in it, or the color is not fully saturated; the maximum luminance flux of white of the color is supplied using the white LED in order to retain the saturation level required. In the process, the intensity of one of the three colors will be completely eliminated and the two others will be reduced in intensity. Figure 4.1 schematically demonstrates the process of conversion from RGB to RGBW through an example, where the source data is chosen to be R = 75, G = 90, and B = 45. First, the three data sources are compared in order to distinguish the source with the minimum intensity out of RGB which in this case is B. Then, the value of the minimum intensity will be deducted from all three sources so R would take the value 30, G = 45, and B = 0. Finally, this value will be supplied to the W which becomes 45. As shown in the example in figure 4.1, the converted data will consist of four data sources, RGB and W.

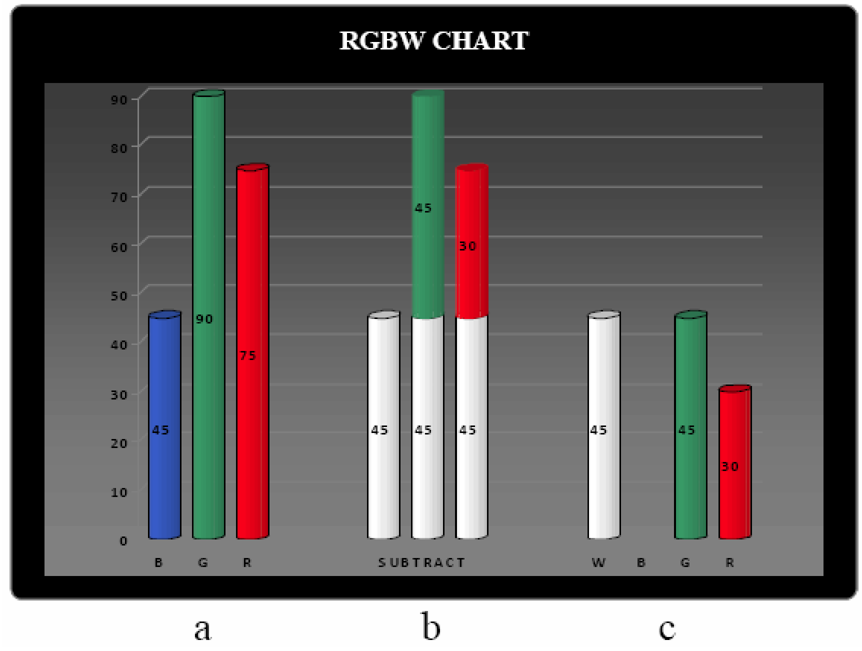

Figure 4.1 RGBW chart. Y axis represents 255 different possible levels of digital color intensities that correspond to an eight bit data bus for each color. (a) Intensity levels for RGB in a pixel (b) Identified intensity of white in the pixel (c) B completely eliminated, white LED introduced and R and G reduced.

The combination of light wavelengths to produce a given perceived color is not unique. The white intensity in a certain color affects its saturation [24]. In other words, a perfectly saturated color is missing the element of white; therefore, only monochromatic and dual chromatic colors can be perfectly saturated. That given, it is concluded that by eliminating the white component, the hue will not change but its saturation level will, which could be compensated by adding a white light from any other light source such as a white LED. The human eye can not distinguish between similar hues that are produced by different components of light wavelengths; however, it may affect the way colors of objects are perceived by the human eye if these light sources are used for ambient lighting purposes. Since this project is only concerned with display systems, one can conclude that using the white LED in order to display colors in such systems will not affect the colors perceived by the observers.

The following analysis theoretically demonstrates that the hue from RGBW and RGB will be the same. Using equation 4.1, the new color, Cnew, after reducing the intensities of R, G and B by x, is given by:

$$\begin{aligned} \mathrm{Cnew} &= (R\text{-x})\,\mathrm{R} + (B\text{-x})\mathrm{B} + (G\text{-x})\,\mathrm{G} \\ &= (R\mathrm{R}+B\mathrm{B}+G\mathrm{G}) - \mathrm{x}(\mathrm{R}+\mathrm{G}+\mathrm{B}) = \mathrm{C} - \mathrm{xW} \end{aligned} \tag{4.1}$$

Note that the rewritten equation 4.2 has two components on the right hand side. The first term corresponds to the old color with the original intensities of the R, G and B and the second term corresponds to the amount of white intensity, which was removed from the pixel by reducing intensities of R, G and B by x. The calculations above show that the process of reducing an x amount of luminance from every RGB LED is equivalent to the process of reducing the same amount of white light.

Considering the HSV system, one can also show that the hue can be maintained when comparing the traditional pixel to the new RGBW pixel set up. Using the set of equations 3.5.5 in order to determine the hue, all sub-pixel combinations can be taken into account as follows:

When R is maximum and G is minimum, H_{new} is given by:

$$H_{new} = 5 + \frac{(R-G)-(B-G)}{(R-G)-(G-G)} = 5 + \frac{R-B}{R-G} = H_{old} \tag{4.2.a}$$

When R is maximum and G is not minimum, H_{new} is given by:

$$H_{new} = 1 - \frac{(R-B)-(G-B)}{(R-B)-(B-B)} = 1 - \frac{R-G}{R-B} = H_{old} \tag{4.2.b}$$

When G is maximum and B is minimum, H_{new} is given by:

$$H_{new} = 1 + \frac{(G-B)-(R-B)}{(G-B)-(B-B)} = 1 + \frac{G-R}{G-B} = H_{old} \tag{4.2.c}$$

When G is maximum and B is not minimum, H_{new} is given by:

$$H_{new} = 3 - \frac{(G-R)-(B-R)}{(G-R)-(R-R)} = 3 - \frac{G-B}{G-R} = H_{old} \tag{4.2.d}$$

When B is maximum, H_{new} is given by:

$$H_{new} = 3 + \frac{(B-\min)-(G-\min)}{(B-\min)-(\min-\min)} = 3 + \frac{B-G}{B-\min} = H_{old} \tag{4.2.e}$$

where H_{new} is the hue obtained from the new RGBW pixel and H_{old} is the hue obtained from the traditional RGB pixel. Equations 4.2.a-4.2.e clearly show that the hues H_{new} (RGBW) and H_{old} are the same. Using equation 3.5.3, the saturation of the new pixel is found to be 1, which means it is fully saturated since the element of the white is removed. However, the saturation level can be individually controlled by the white LED to match the saturation of the old pixel. The value, as stated in equation 3.5.4, is the maximum component among RGB which in the new pixel configuration that value will be reduced by the minimum amount among RGB, which can also be compensated by the value of the white.

4.4 The RGBW LED Display Prototype and Driver

4.4.1 Hardware

An 8X8 pixel block display prototype is developed; each pixel consists of RGBW LEDs placed in a square configuration as shown in Figure 4.2. LEDs are driven by LED drivers. Each driver drives eight LEDs. The display block has eight parallel inputs, which implies that every four drivers are serially connected (red and white are serially connected, green and blue are serially connected). The prototype is driven by an FPGA.

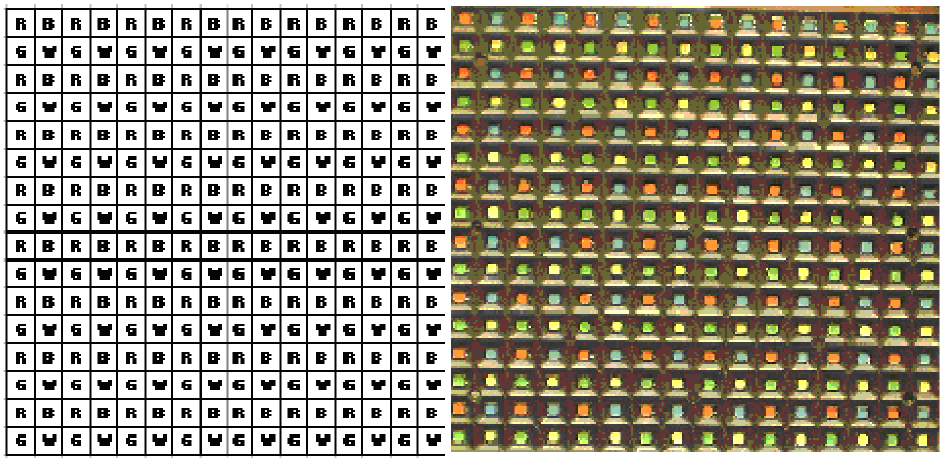

R	B	R	B	R	B	R	B	R	B	R	B	R	B	R	B
G	W	G	W	G	W	G	W	G	W	G	W	G	W	G	W
R	B	R	B	R	B	R	B	R	B	R	B	R	B	R	B
G	W	G	W	G	W	G	W	G	W	G	W	G	W	G	W
R	B	R	B	R	B	R	B	R	B	R	B	R	B	R	B
G	W	G	W	G	W	G	W	G	W	G	W	G	W	G	W
R	B	R	B	R	B	R	B	R	B	R	B	R	B	R	B
G	W	G	W	G	W	G	W	G	W	G	W	G	W	G	W
R	B	R	B	R	B	R	B	R	B	R	B	R	B	R	B
G	W	G	W	G	W	G	W	G	W	G	W	G	W	G	W
R	B	R	B	R	B	R	B	R	B	R	B	R	B	R	B
G	W	G	W	G	W	G	W	G	W	G	W	G	W	G	W
R	B	R	B	R	B	R	B	R	B	R	B	R	B	R	B
G	W	G	W	G	W	G	W	G	W	G	W	G	W	G	W
R	B	R	B	R	B	R	B	R	B	R	B	R	B	R	B
G	W	G	W	G	W	G	W	G	W	G	W	G	W	G	W

Figure 4.2 A schematic diagram showing the square pixel configuration with RGB and W LEDs used for this research and the prototype from TecnoVision.

4.4.2 The LED Driver

The STP08CDC596 chip is An 8-bit constant current LED sink driver with full outputs detection and is used for driving the LEDs that compose the pixels of the display. Key features as listed in the data sheet of the LED driver chip are [37]:

- 8 constant current output channels
- Adjustable output current through one external resistor
- Open and short line, short to GND, short to V-LED supply error detection
- Serial data in/parallel data out
- Serial out change state on the falling edges of clock

- Output current: 20-120mA
- 3.3V micro driver-able
- 25MHz clock frequency

The data is inputted serially through the serial data input (SDI) pin and outputted in parallel through the out 0 thru 7 pins. The latch-enable (LE) and the output-enable (OE) pins are data control pins. The clock is provided at the clock pin (CLK). Figure 4.3 shows the pin-out of the chip used.

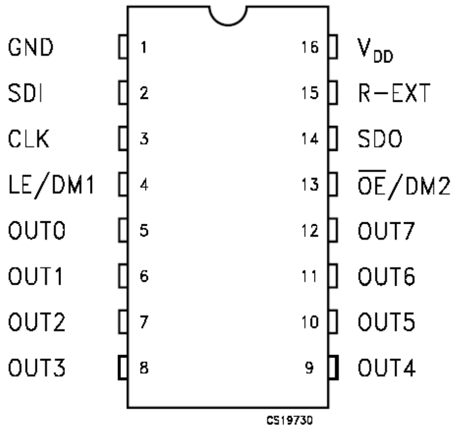

Figure 4.3 A schematic diagram showing the 8-bit constant current LED sink driver (STP08CDC596) [37].

The timing diagram provided in the data-sheet needs to be considered in the software design and is shown in Figure 4.4. In normal mode the OE/DM2 must remain low at least two clock cycles. In case of OE signal enabled (OE is active low) during no clock activity (clock stopped), after the CLK restarts, 3 full CLK cycles are necessary before disabling the OE signal (OE is passive high) [37].

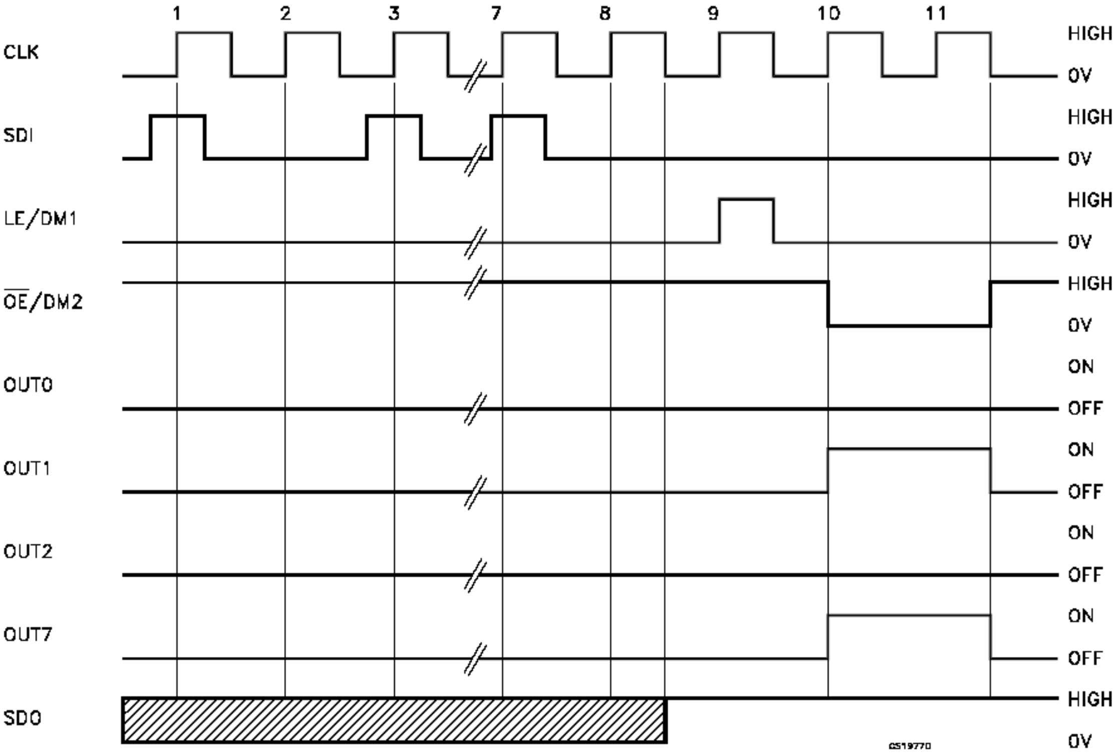

Figure 4.4 A timing diagram showing the pin's statuses of the LED driver chip [37].

There are 32 driver chips used in order to accommodate the number of LEDs, 256 LEDs, required for an 8x8 pixel display. The schematic in Figure 4.5 shows the layout of the circuitry supporting the prototype. In the schematics RW pins represent the data for red and white and the BG represent the blue and green data pins. The rest of the pins are described at the beginning of this section.

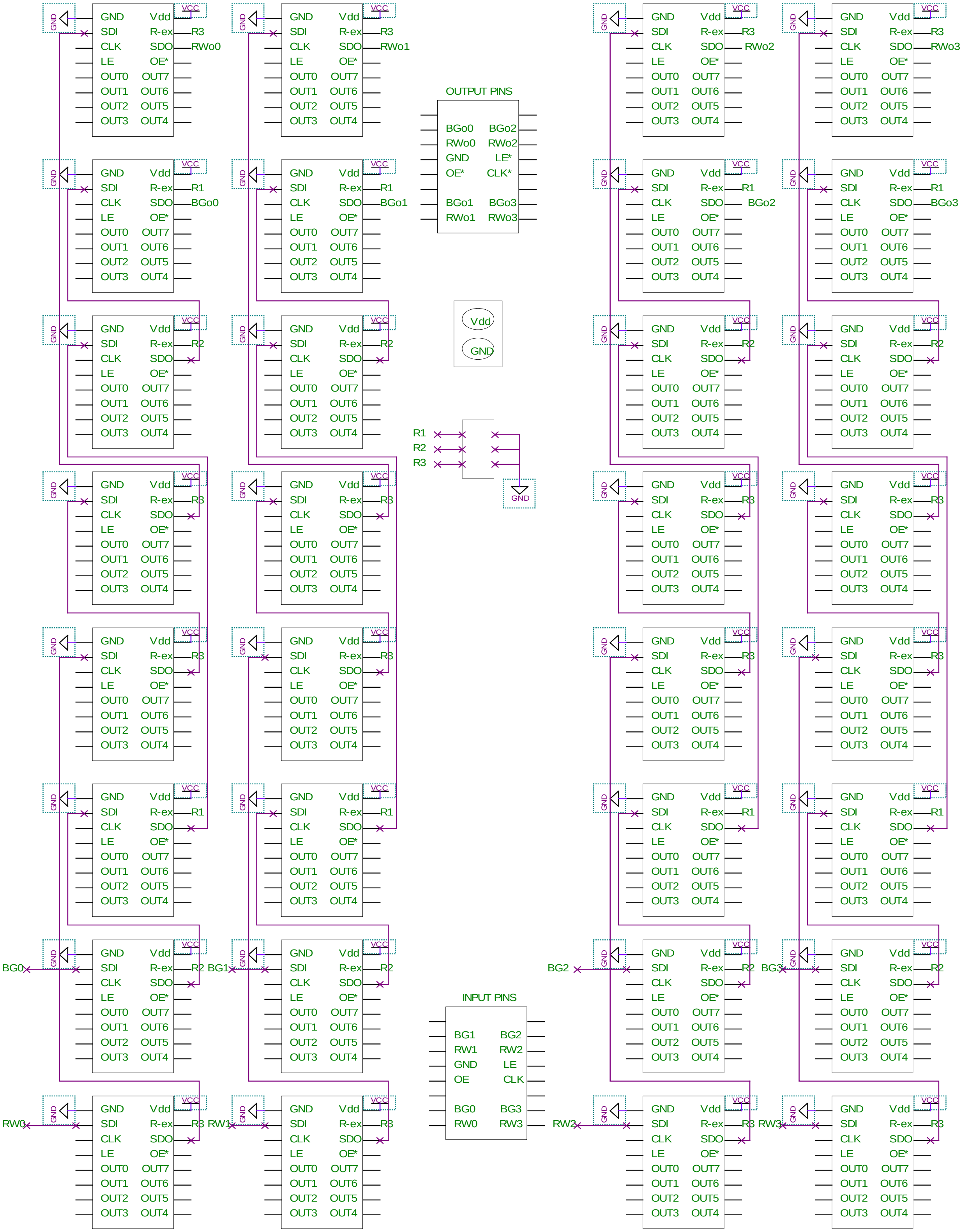

Figure 4.5 A schematic diagram showing the circuit layout of the prototype.

4.4.3 The Display Driver

In order to drive the LED display prototype, the DE2 development and education board is used. The DE2 has many key features and contains the appropriate components for the hardware requirements of the project. The following is a list of the DE2 components and features that are used in the project as listed in the user manual of the DE2 board [38]:

- Altera Cyclone® II 2C35 FPGA device
- Altera Serial Configuration device - EPCS16
- USB Blaster (on board) for programming and user API control; both JTAG and Active Serial
- 512-Kbyte SRAM
- 8-Mbyte SDRAM
- Expansion headers (76 signal pins)
- 4-Mbyte Flash memory
- 18 toggle switches
- 18 red user LEDs
- 50-MHz oscillator and 27-MHz oscillator for clock sources
- VGA DAC (10-bit high-speed triple DACs) with VGA-out connector

4.4.4 Software

As described in the block diagram in Figure 4.8 there are two different RGB sources: Pattern generator (implemented in memory), and real time serial digital input (SDI) video signal (outputted from a scalar board that converts video signal to RGB). In the pattern generator, the synchronization signals shown in Figures 4.6.a and 4.6.b are also generated.

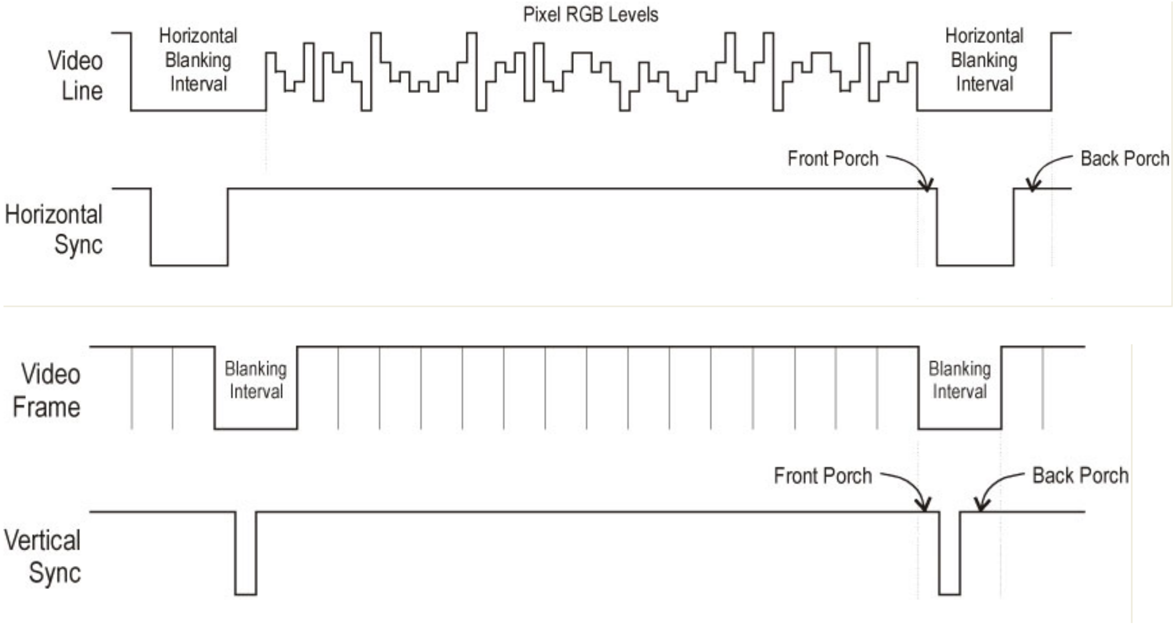

Figure 4.6 A timing diagram showing the (a) horizontal timing (b)vertical timing [39].

Using an FPGA The signals are decoded and fed into the RGB to RGBW converter. Then, the RGBW input data (eight bit data bus for every color) is remapped. Due to the architecture of the display, the input data looses its order when outputted directly to the display as shown in Figure 4.7. For optimal hardware design, such configuration was required.

R27	R26	R25	R24	R11	R10	R9	R8
W19	W18	W17	W16	W3	W2	W1	W0
R28	R29	R30	R31	R12	R13	R14	R15
W20	W21	W22	W23	W4	W5	W6	W7

Figure 4.7 A diagram showing the order of the white and the red of the pixels of the first two rows of the display without reordering

Finally, pulse width modulation (PWM) is used to output to the RGBW data to the display. The color accuracy of the white point will be maintained by reducing the variation in white point if the LEDs are driven using PWM [15]. A 5” x 5”of white plastic diffuser is used in order to properly mix the light of the pixel in order to perceive a uniform color.

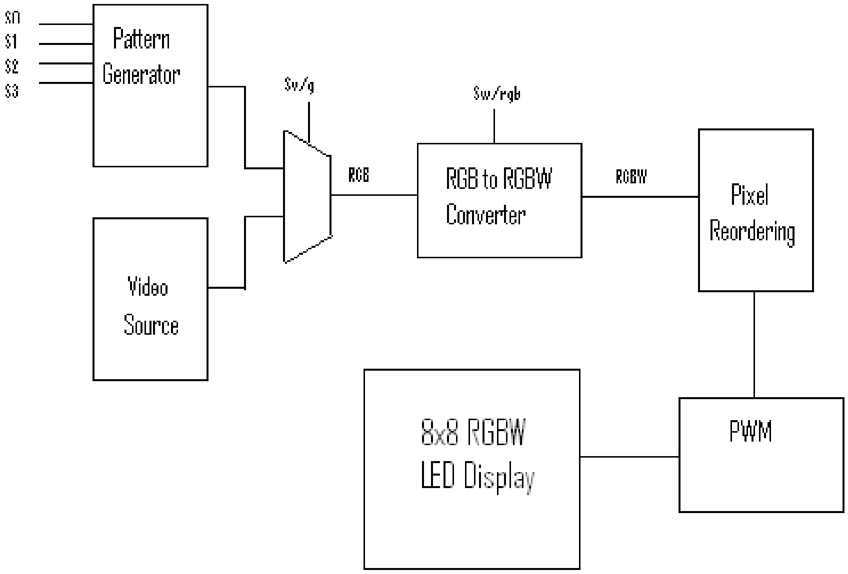

Figure 4.8 A block diagram where S (0-3) allow variety of solid colors to be displayed, S(v/g) selects pattern generator or video, and S(w/rgb) turns the RGB to RGBW conversion on or off.

Using the switches of the development board of the FPGA, one can choose to bypass the conversion so that the display will use the classical RGB pixel instead of RGBW. Using another set of switches, the hardware provides the possibility to choose various solid colors from the pattern generator to be displayed.

The following schematics Figures 4.9 (a thru i) demonstrate the logic implementation in the FPGA of every part described in the block diagram in Figure 4.8. These are selected parts of the schematics file that was split due to its large size.

A 27 MHz clock from the DE2 evaluation board is used for both synchronization of the implemented logic and for the generation of the signals required for image display (compatible with a VGA input connector) as shown in Figure 4.9.a. These signals include the horizontal and vertical syncs (hsync and vsync), horizontal and vertical blanks (hblank and vblank), and the vertical count (Vcnt). The logic was implemented with a 16.6 ms refreshing rate requirement assuming a resolution of 720x 480. Then, an extraction of 8x8 pixels was done to match the size of the prototype.

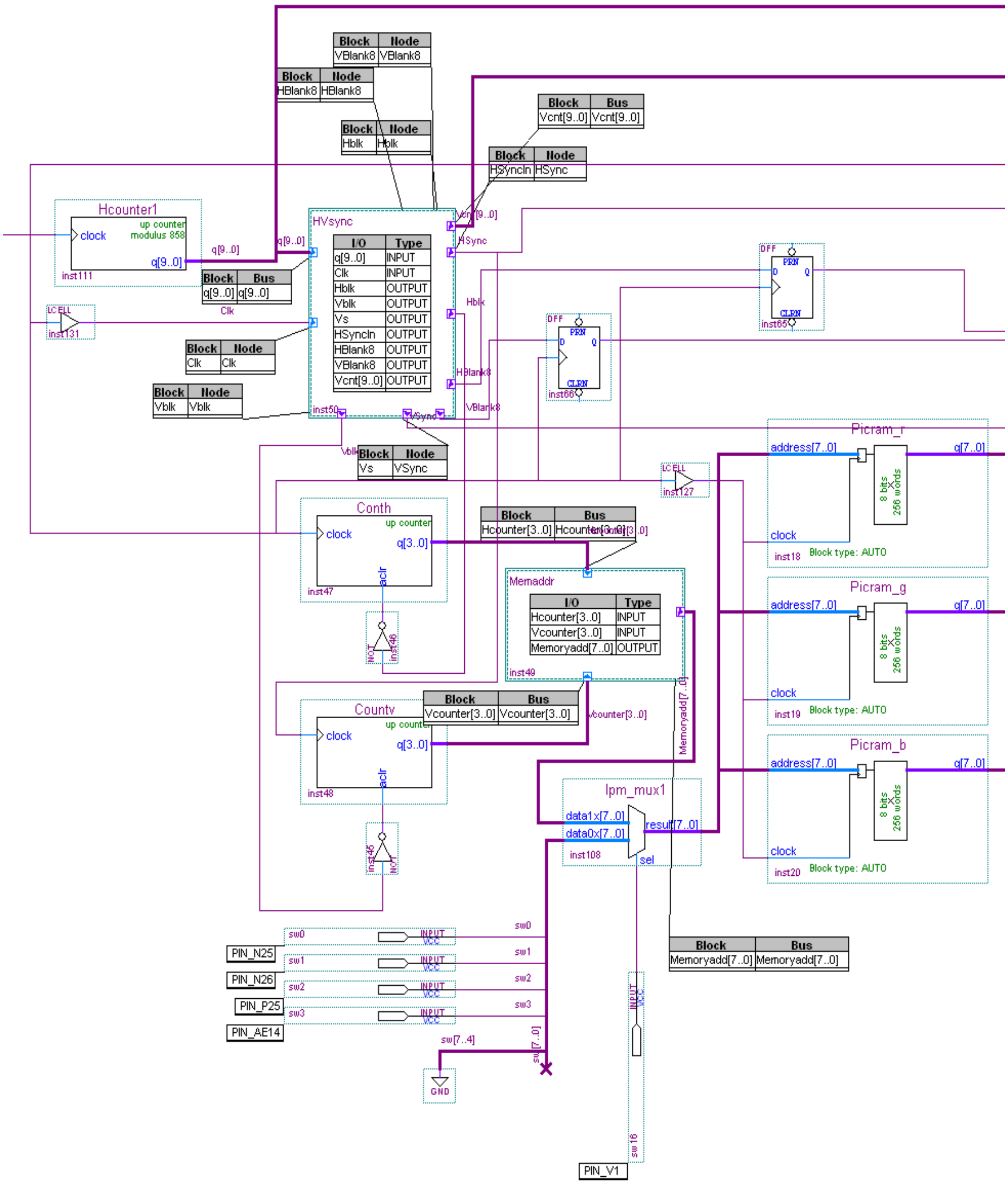

Figure 4.9.a A schematic diagram showing the implementation of the pattern generator.

The hsync and vsync are two of the signals of which a VGA connector consists for RGB video output. They provide the monitor with the timing information necessary to correctly display the pixel RGB data. VGA video output is a stream of frames that are refreshed at a certain frequency (refreshing rate). Every frame consists of a series of horizontal lines where each of which is made up of a series of pixels [40]. In every frame, the pixel data is transmitted in order from top left corner to bottom right corner. In order to locate the ends of every line and frame, separate horizontal and vertical synchronization signals are required [40]. There are two regions that every horizontal line of the display experiences: active video and blanking region. In the active video region, RGB values are outputted for every pixel in the line. In the blanking region, there is the front porch where black pixels are transmitted. Then, a horizontal sync pulse is transmitted which is an indicator of the end of the line. The blanking interval after the sync pulse is called the back porch where black pixels are also transmitted [40]. In order to display a single frame, all the lines of which the frame consists are transmitted in the active region of the vertical timing. Similar to the horizontal line, black lines will be transmitted in the front porch. Then, a vertical sync pulse is transmitted indicating the end of a frame followed be the back porch. Figure 4.6(a-b) is a timing diagram showing the appropriate timing of the vsync and hsync signals to be outputted with the video signal.

The synchronization signals are also used in order to address the RAM, which contains RGB data which can be manually changed through the software. As shown in Figure 4.9.a, the memory can be addressed either by the counter that is controlled by the horizontal and vertical counters or by the switches that can be manually controlled from the evaluation board by the user. The RGB data is inputted to the other parts of the project units from the data generator along with VGA video output. The interface is shown in Figure 4.9(b-c) where the RGB data from both sources are decoded with 2 to 1 multiplexers that select either source as an input to the next part which is the converter.

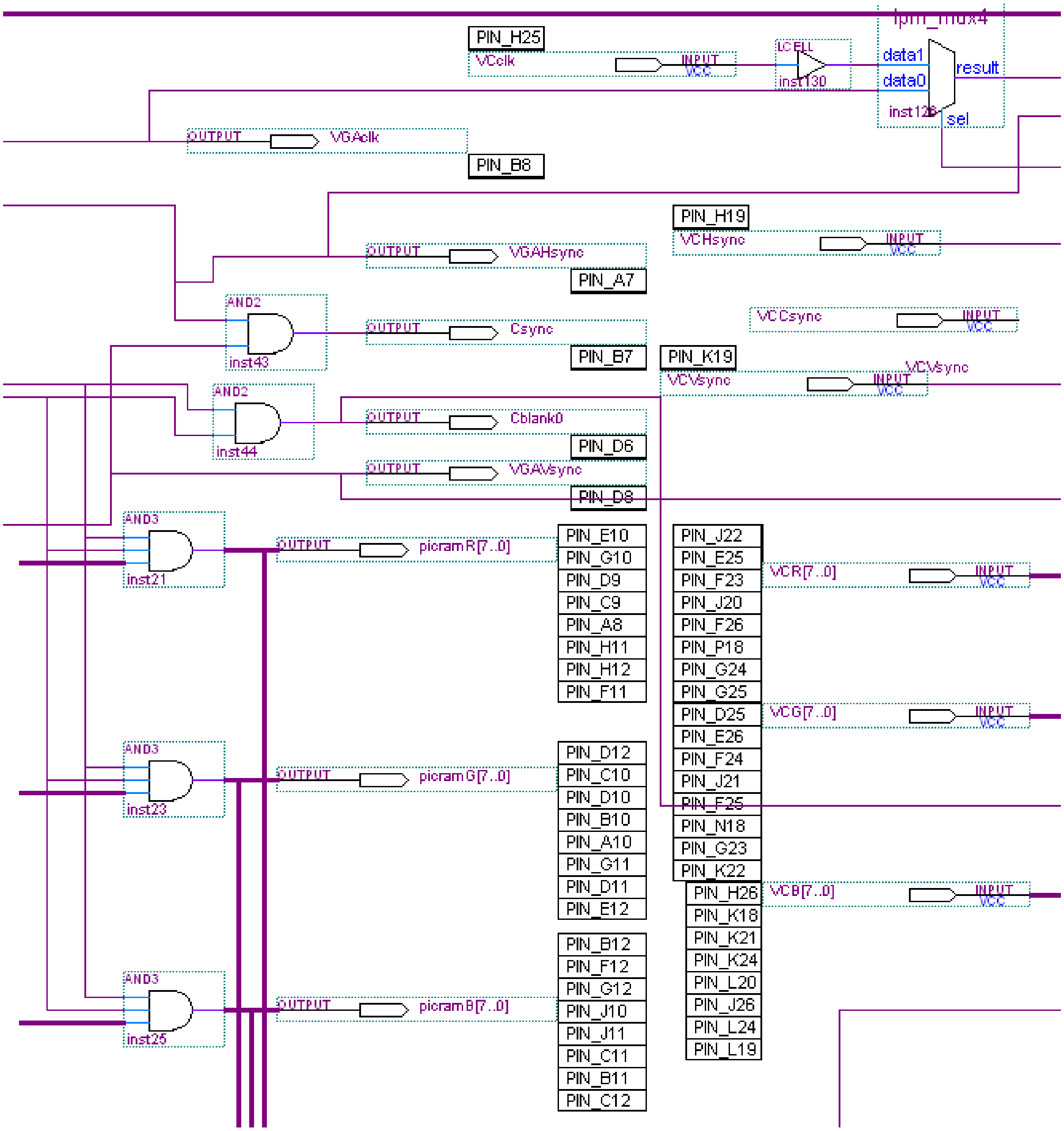

Figure 4.9.b A schematic diagram showing the video input source.

The data of the video input source is taken directly from the SDI which is an 8 bit data stream representing RGB. The desired signal, whether it is the generator or the video is determined by the select line (sel).

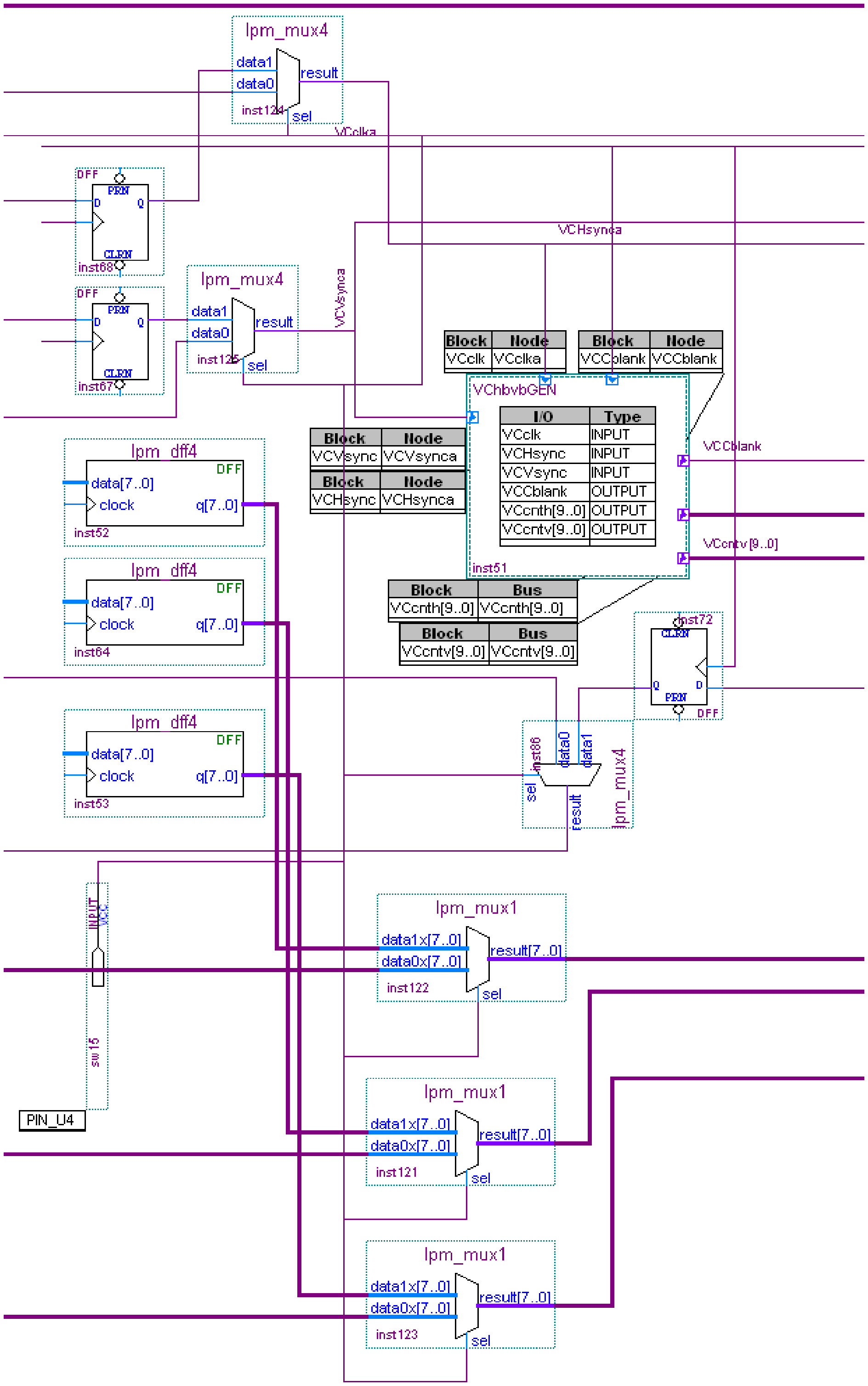

Figure 4.9.c A schematic diagram showing the interface between the input sources and the converter.

After receiving the RGB data from the appropriate source, it is passed to the RGB to RGBW convertor. The data is compared to each other to determine the color with the minimum value as shown in Figure 4.9.d. The logic levels of the comparator's outputs are used along with a lookup table to set the multiplexer to the value that needs to be subtracted from RGB and supplied to the white LED.

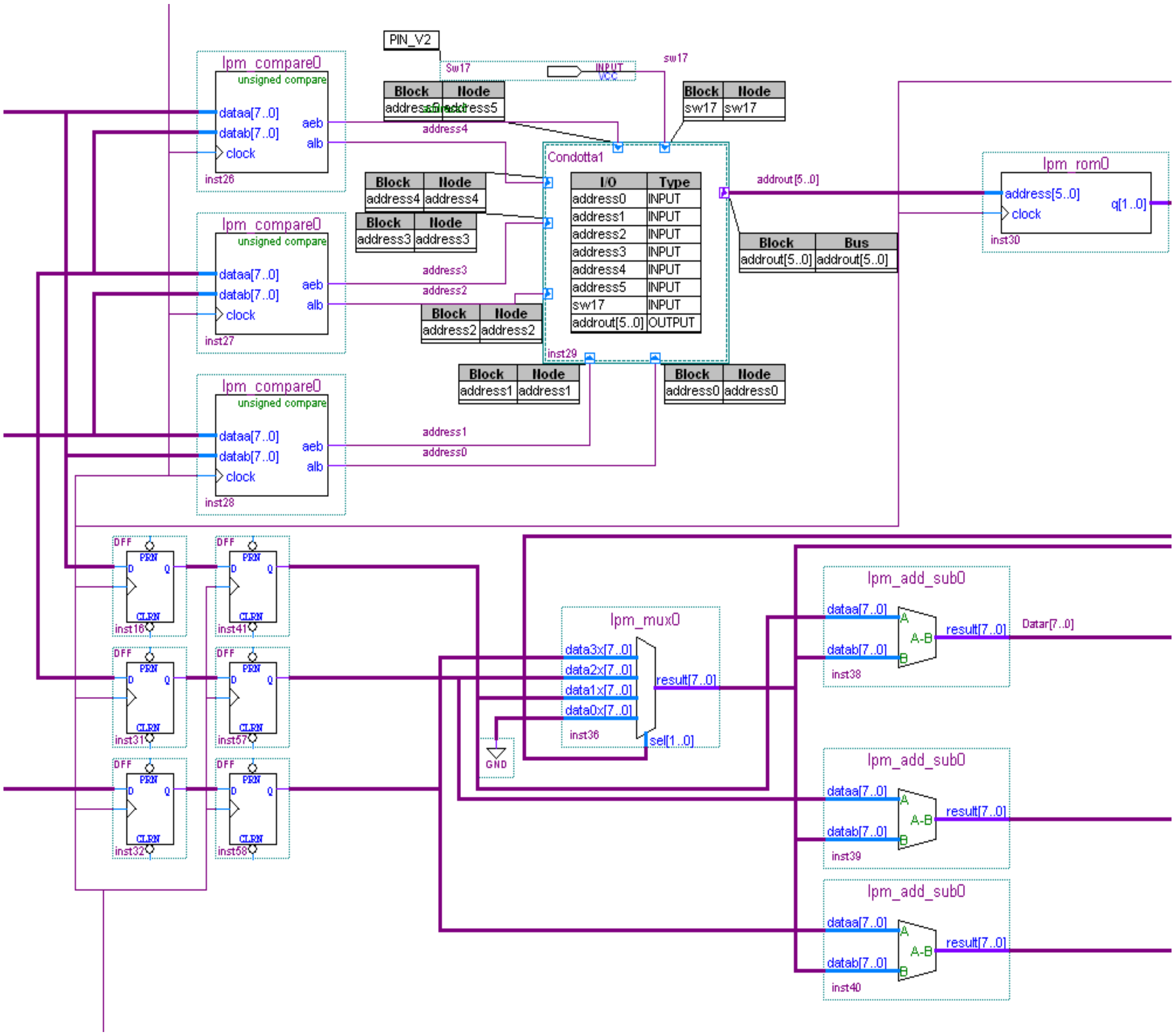

Figure 4.9.d A schematic diagram showing the implementation of the RGB to RGBW converter.

The block in Figure 4.9.e is an implementation of the control signals generation for different parts of the design. These signals include: FIFO memory read enable (FIFOrdEn), dual ported memory stage 1 and 2 read enables, DPst1rdEn and DPst2rdEn, respectively, and the LED display latch and output enables LEDisp and OEDisp, respectively.

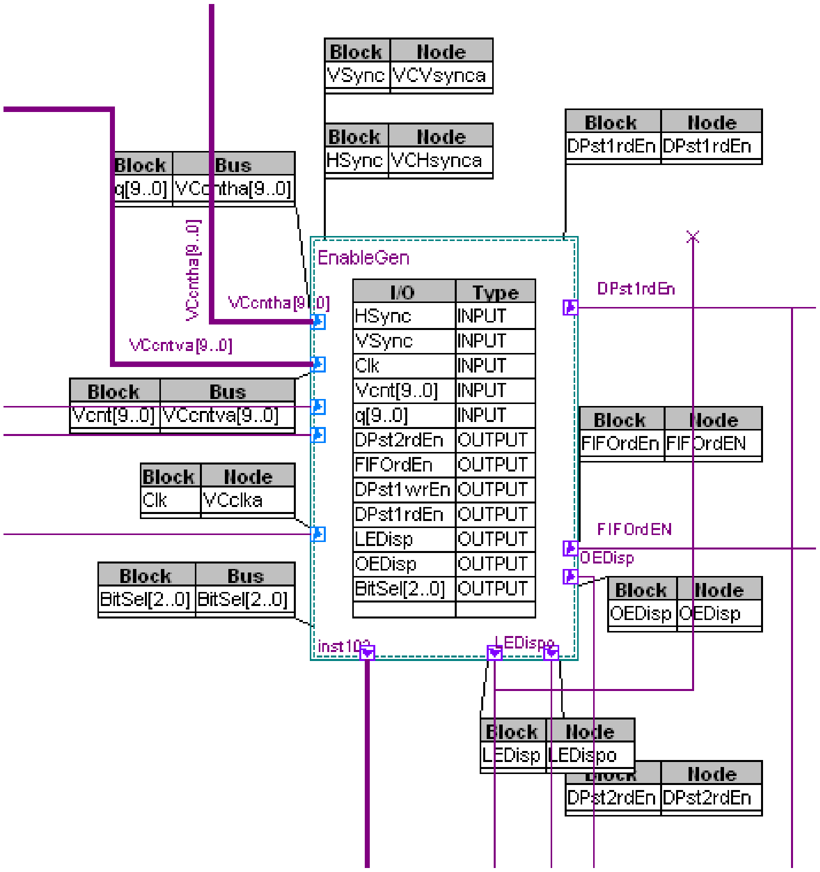

Figure 4.9.e A schematic diagram showing the implementation of the control signals generator.

The order of the data when directly outputted to the prototype the way it is received from the video or generator data stream takes a pattern as shown in Figure 4.8. Therefore, it was necessary to implement a pixel reordering mechanism.

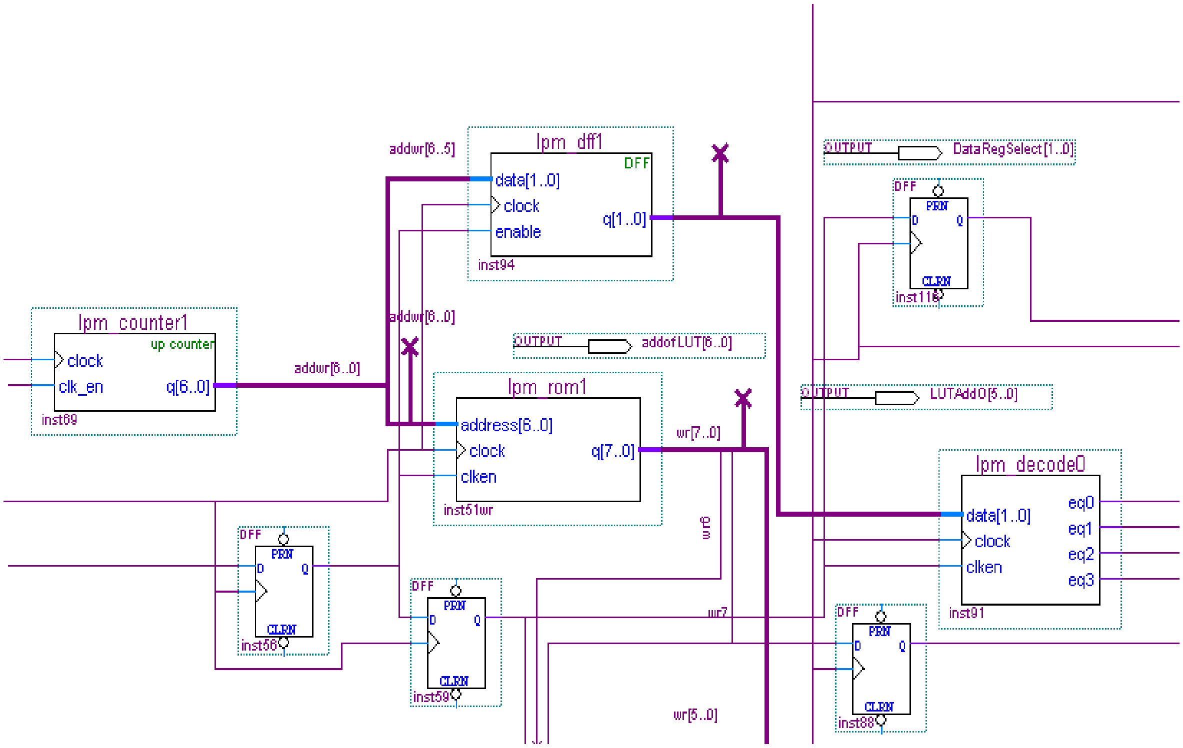

Figure 4.9.f A schematic diagram showing the implementation of the pixel reordering block.

Pixel reordering was done using the enable signals and a lookup table, as shown in Figure 4.9.f. These signals were used to address the dual ported memory shown in Figure 4.9.g. There are three memory stages one is FIFO and the other two stages are dual ported memories. After the RGB to RGBW conversion, the RGBW data is inputted to the FIFO then to the first dual ported memory stage; finally, inputted to the last dual ported memory stage in the desired order, shown in Figure 4.9.h.

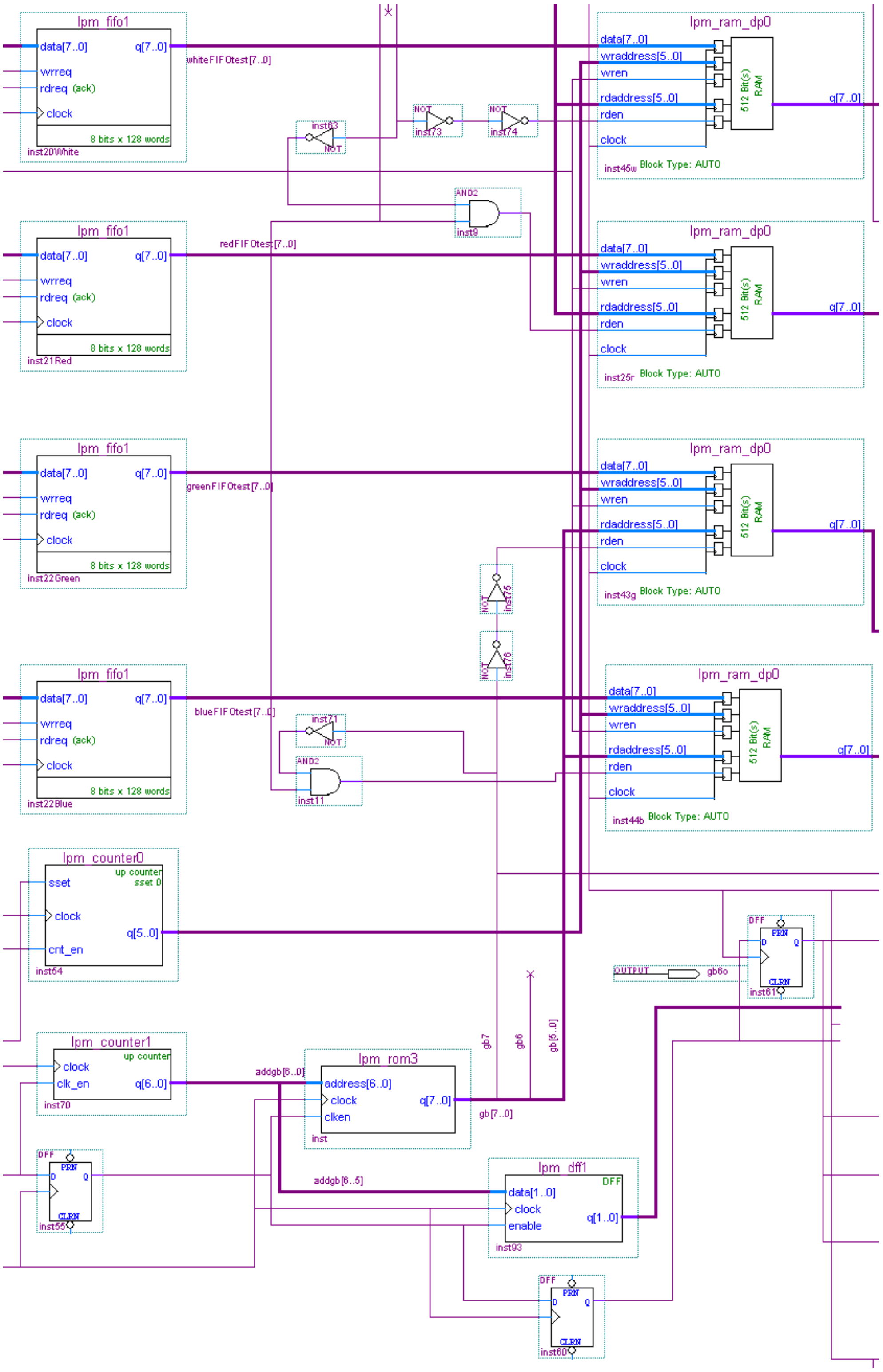

Figure 4.9.g A schematic diagram showing the implementation of the RGBW data processing- stage 1 and 2.

The 8 bit RGBW data lines are pulse width modulated which provides the ability of displaying 256 different intensities. After each bit outputted, latch enable (LE) has to be pulsed once and then output enable (OE) has to be pulsed. The duration of the OE pulse width determines the intensity of the LED; therefore, OE was doubled for every bit so that:

$$OE_{PWbit(x)} = 2 \text{ x } OE_{PWbit(x-1)} \tag{4.3}$$

The sample code below shows the settings of the LE, OE, and data output lines for bit 0 (refer to Appendix I for complete code).

```
    ---------------------------------
    DPst2rdv.clk   =        !HSync;
--DPst2rdv.clrn        =        !VSync;
  DPst2rdv.j      =        Vcnt[] == 1;
  DPst2rdv.k      =        Vcnt[] == 2;
    ---------------------------------
    LEDispdv.clk =        !HSync;
--LEDispdv.clrn        =        !VSync;
  LEDispdv.j      =        Vcnt[] == 1;
  LEDispdv.k      =        Vcnt[] == 2;
    ---------------------------------
    OEDispdv.clk =        !HSync;
--LEDispdv.clrn        =        !VSync;
  OEDispdv.j      =        Vcnt[] == 2;
  OEDispdv.k      =        Vcnt[] == 3;
    ---------------------------------
```

Figure 4.10 A sample AHDL code showing the settings of the LE, OE, and data output lines for bit 0.

Given that 16.6ms refresh rate has to be maintained, there are access of 431911 clocks in order to complete modulating 8 bit data lines for 64 pixels taking into account a clock period of 0.037µs. the pulse width was increased so that the LEDs will give a linear response with respect to the binary input of the data lines.

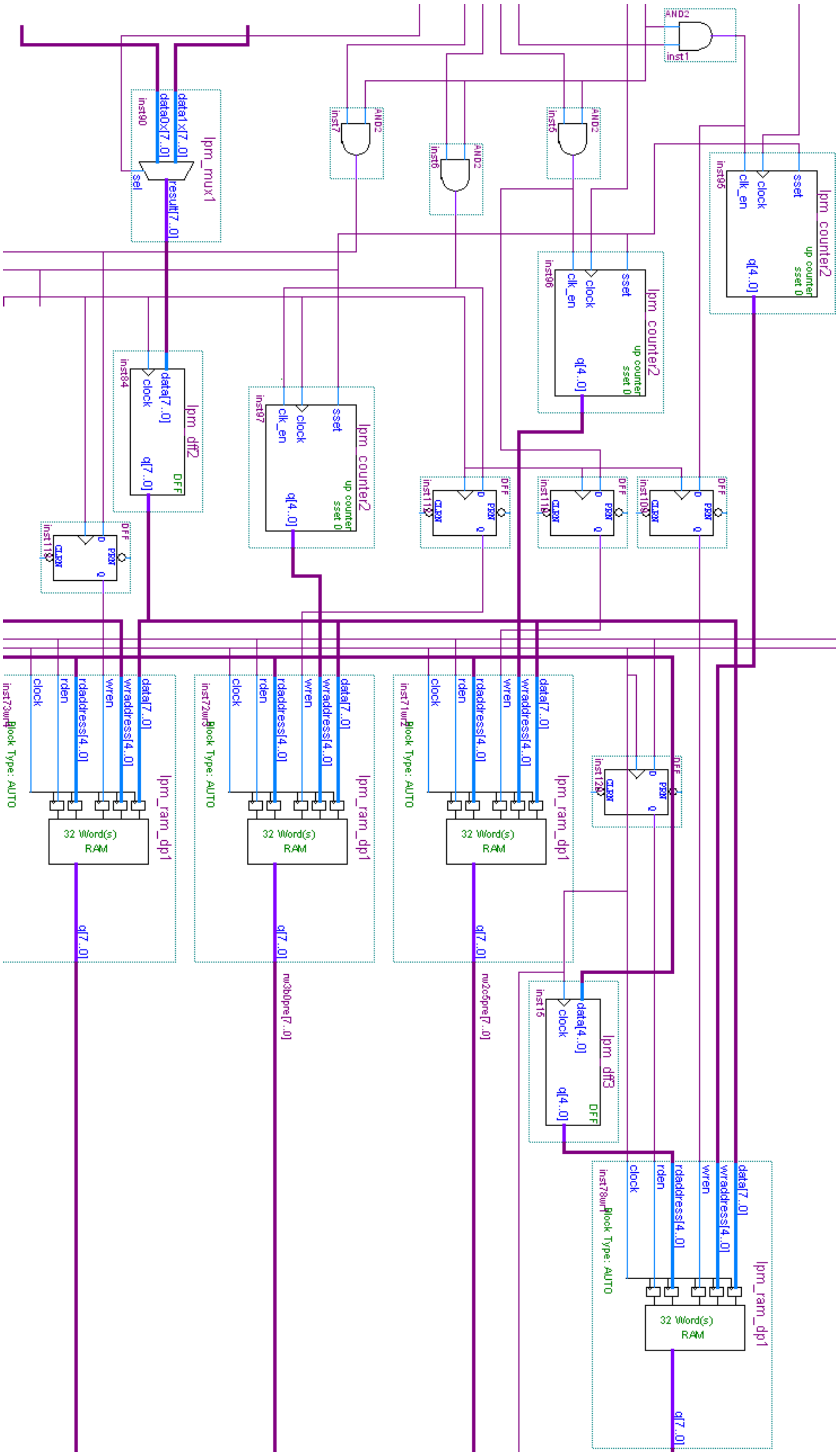

Figure 4.9.h A schematic diagram showing the implementation of the RGBW data processing- stage 3.

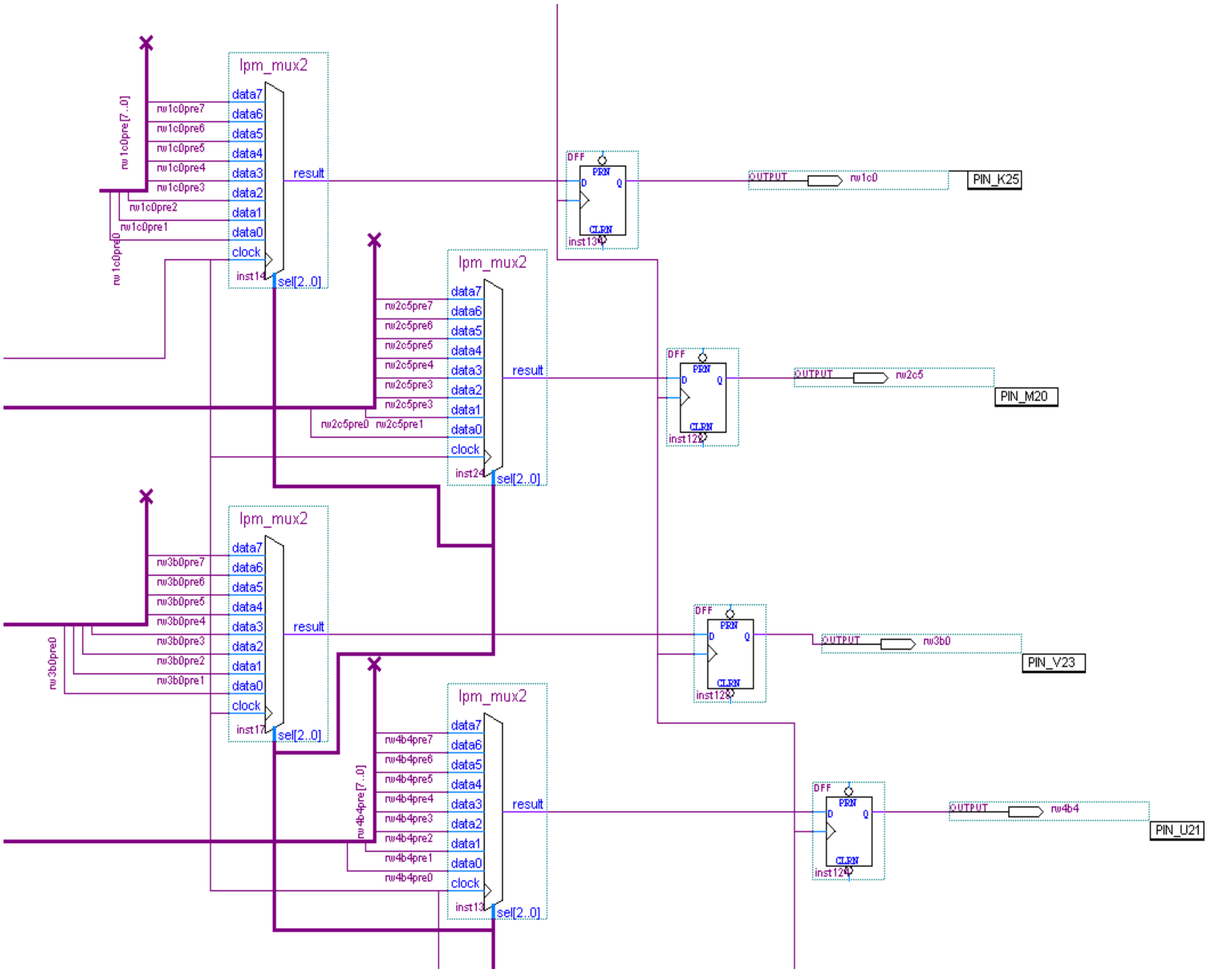

Figure 4.9.i A schematic diagram showing the implementation of the PWM of the RGBW data.

Using an 8 to 1 multiplexer, the appropriate bit is chosen in according to the pulse width of the OE signal, then, finally outputted to the LED display as demonstrated in Figure 4.9.i.

The intensity response was tested for the red, green, blue, and white LEDs using a spectrometer (Ocean Optics USB3000). The spectrometer was placed directly on top of the measured LED where complete stillness was maintained in every part for better accuracy. The results in Figure 4.10(a-d) clearly show a linear response.

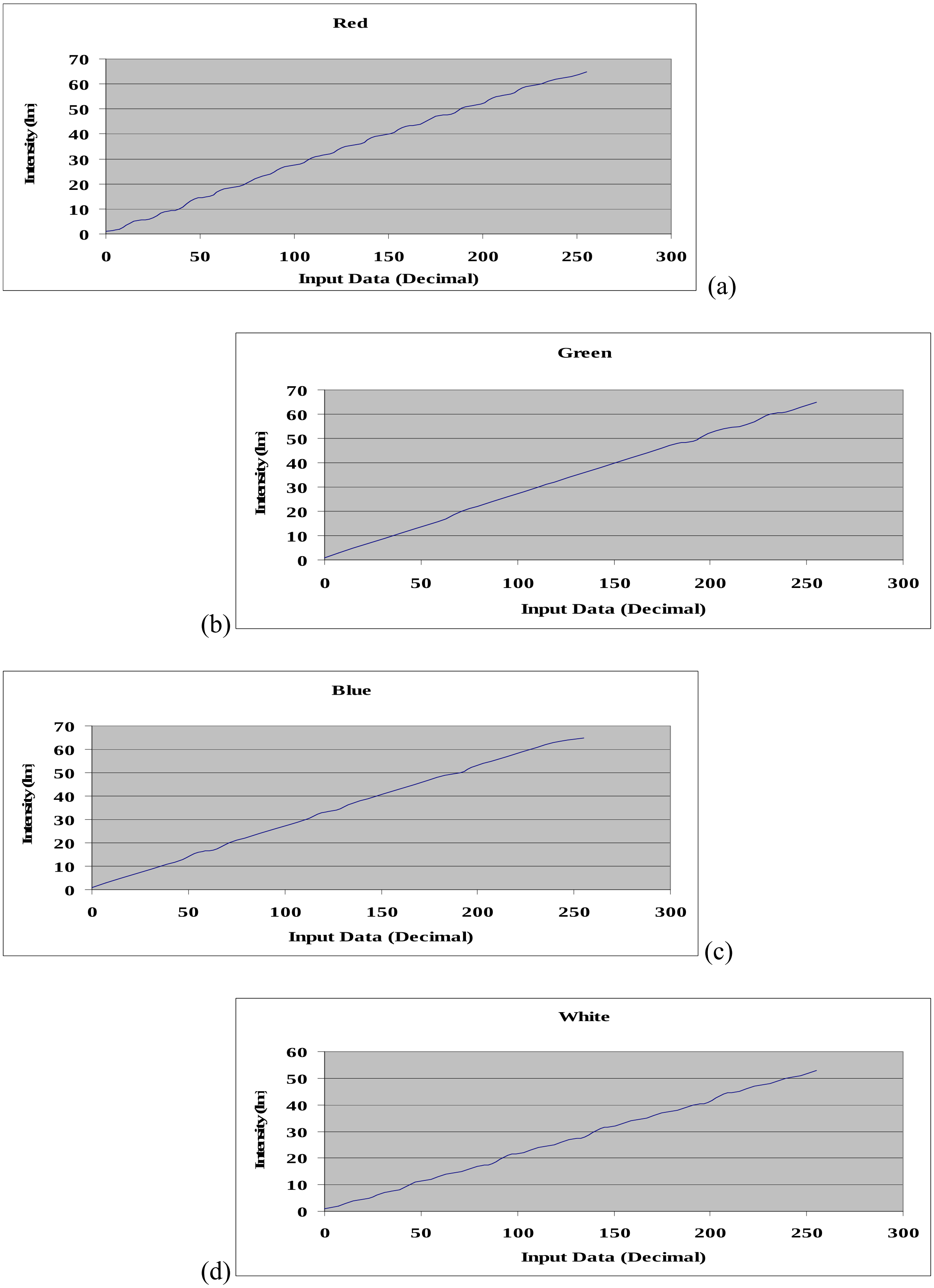

Figure 4.11 A graph showing the intensity response of the (a) red (b) green (c) blue (d) white LED.

CHAPTER 5

EXPERIMENTS, RESULTS, AND DISCUSSION

In this chapter, results and discussion are presented. Spectroscopic measurements of various colors for RGB and RGBW are shown, compared and contrasted. Details of the experimentation with respect to human perception of color from two different technologies (RGB and RGBW) and energy calculations based on measured currents are presented and discussed.

5.1 Spectroscopic Measurements

Using the spectrometer Ocean Optics USB4000, the spectrum, representing the radiant flux, of the colors generated by RGB is measured and compared to the spectrum of color generated by RGBW. The spectrometer was placed directly after the diffuser attached to the LED display in order to capture the right proportions of the light mixture. A static environment was maintained while measurements were taken. Figure 5.1 shows the spectra of the white light generated using the white LED and RGB LEDs, respectively.

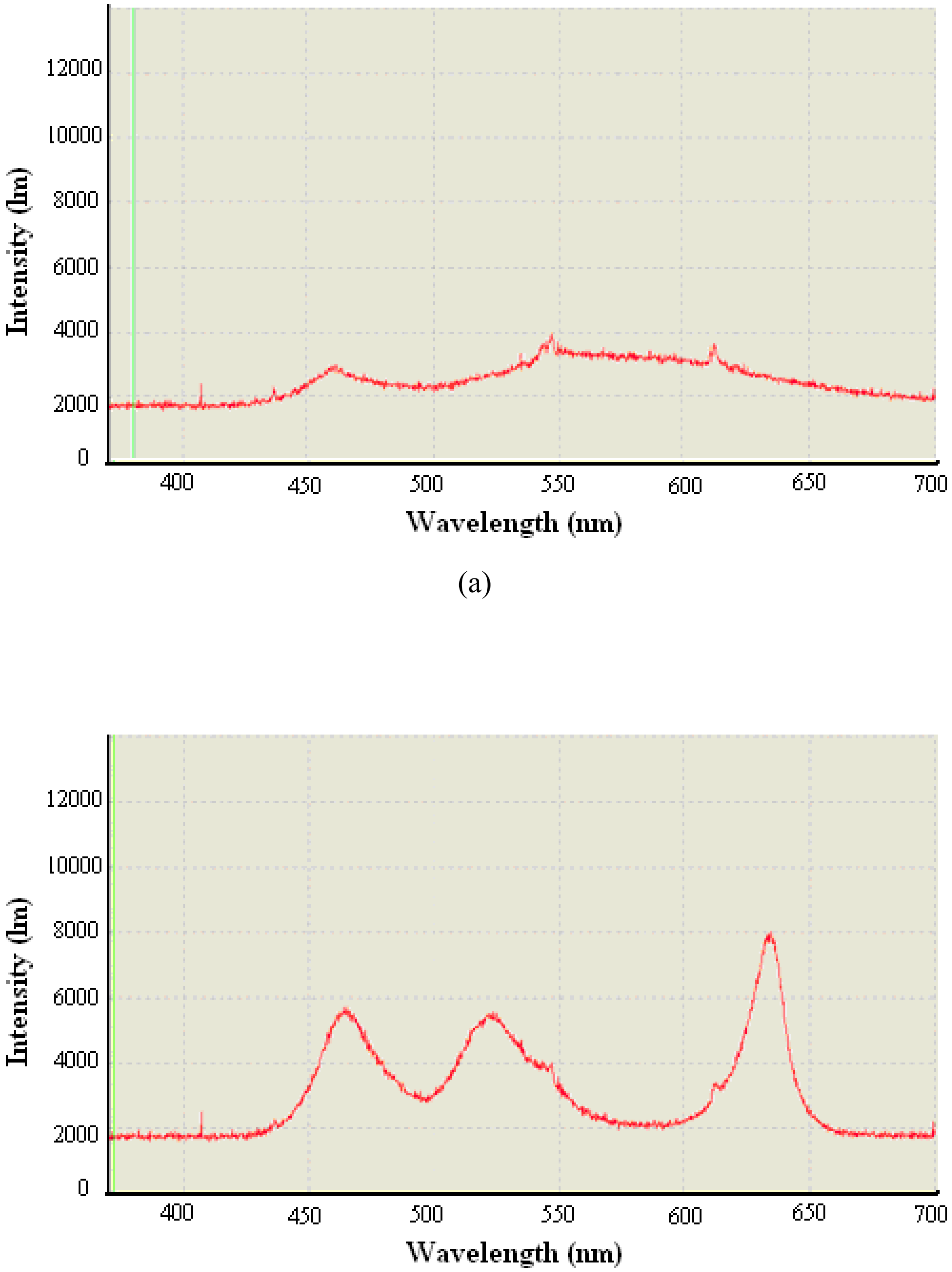

(a)

(b)

Figure 5.1. Spectrum of white, intensity with respect to wave length, using (a) RGBW and (b) RGB.

In Figure 5.1 (a), the intensities corresponding to the local maxima wavelengths are as follows: Red (3267 @ 612nm), Green (3647 @ 547nm), and Blue (2911 @ 460nm). On the other hand, the intensities corresponding to the local maxima wavelengths in (b) are: Red (8104 @ 633nm), Green (5297 @ 521nm), and Blue (5729 @ 464nm). The total brightness of white generated by the white LEDs is noticeably on an average less than the total brightness of white generated by RGB since intensity of white in the display prototype used can not be treated as separate from intensity of red LEDs. Furthermore, the intensity distribution among the various wavelengths differs slightly which results in a variation of the white perceived from the two different sources; even though both are perceived as white. This has an effect on the rest of the experimental measurements. The light spectra for three different colors Navy blue, light blue, and Yellow were also measured using RGBW and RGB configuration and are shown in Figures 5.2-4. Also numerical data of peak intensities of the R, G and B with RGBW and RGB configurations are presented in Table 1 confirm our results.

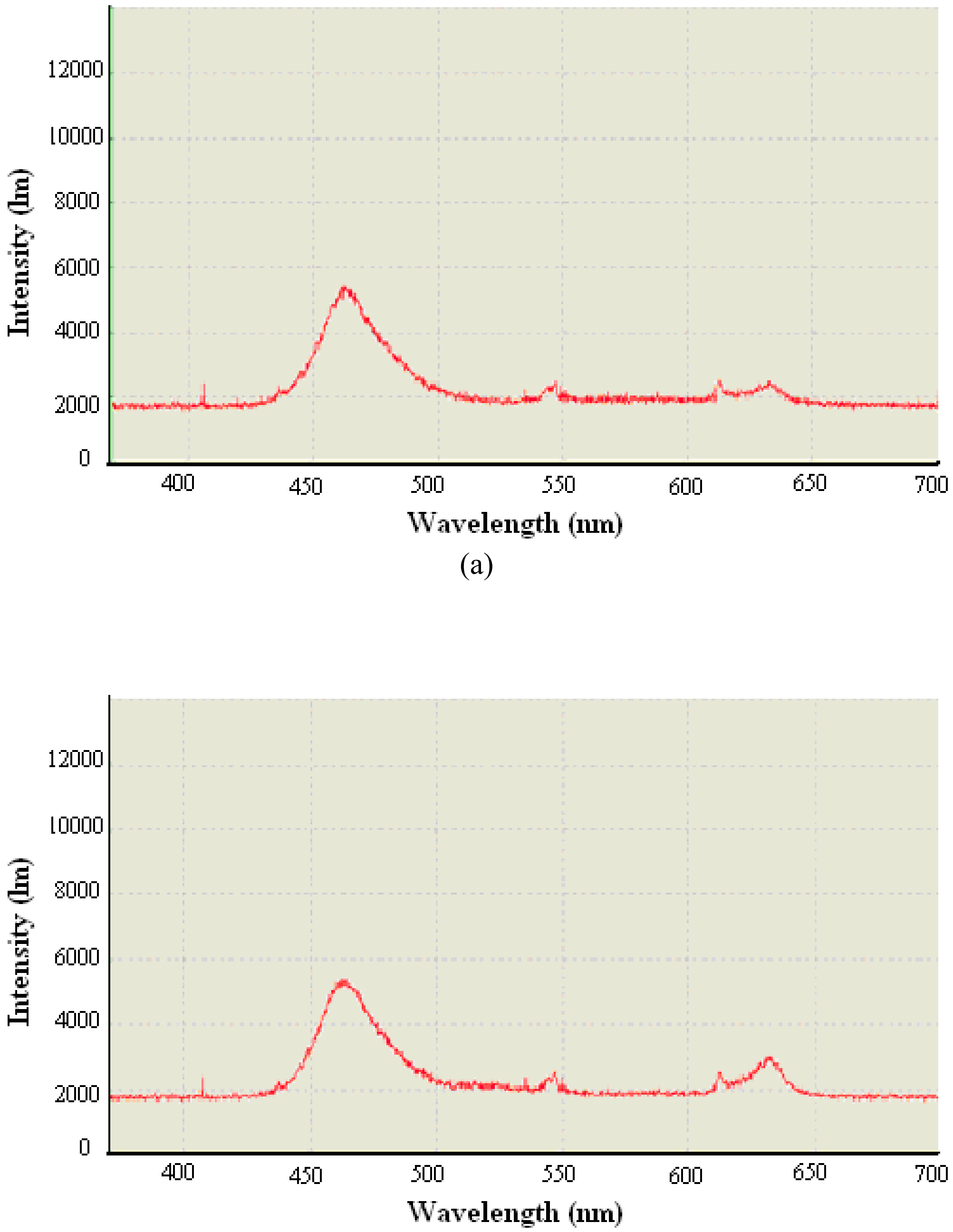

(a)

(b)

Figure 5.2. Spectrum of Navy Blue using (a) RGBW and (b) RGB

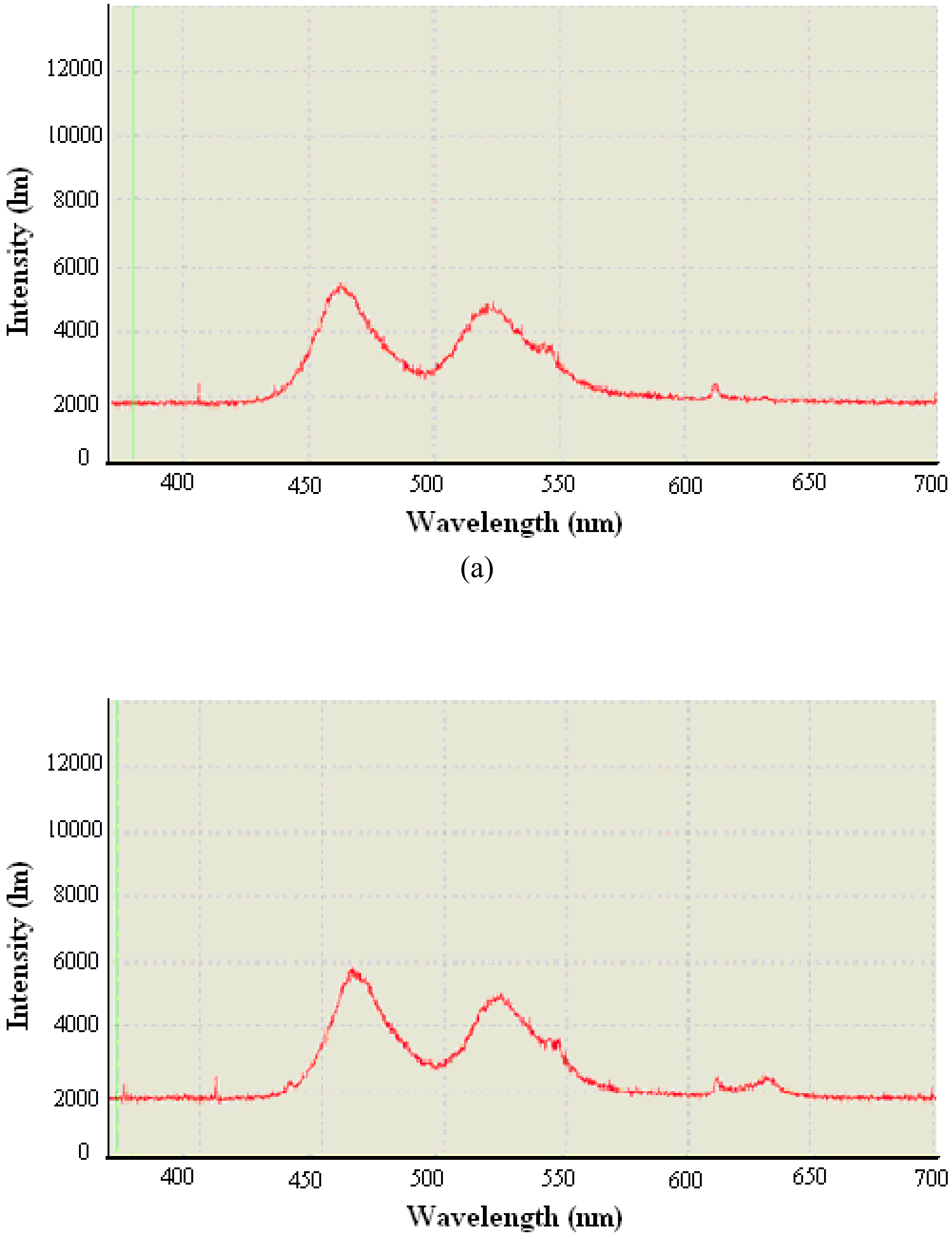

(a)

(b)

Figure 5.3. Spectrum of Light Blue using (a) RGBW and (b) RGB

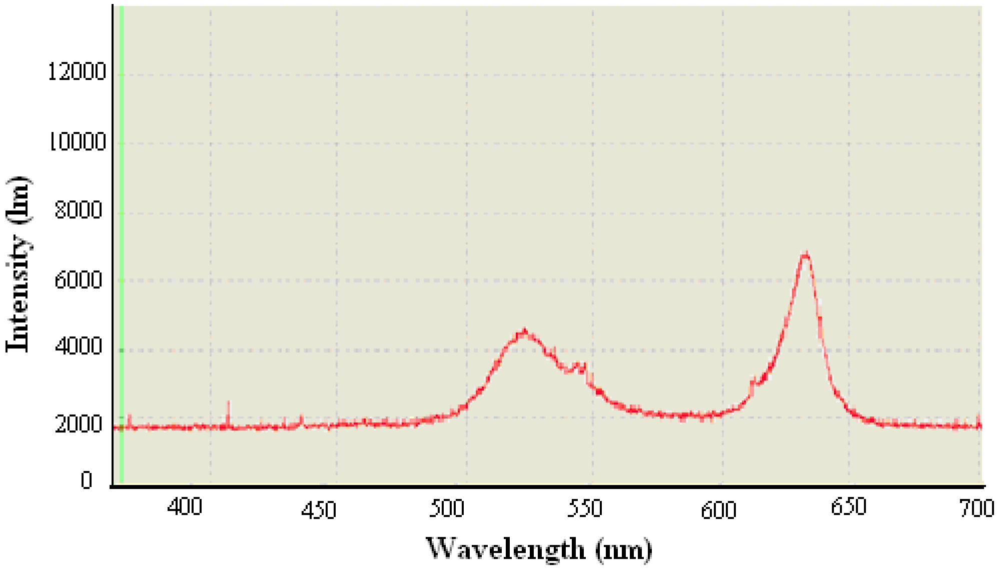

(a)

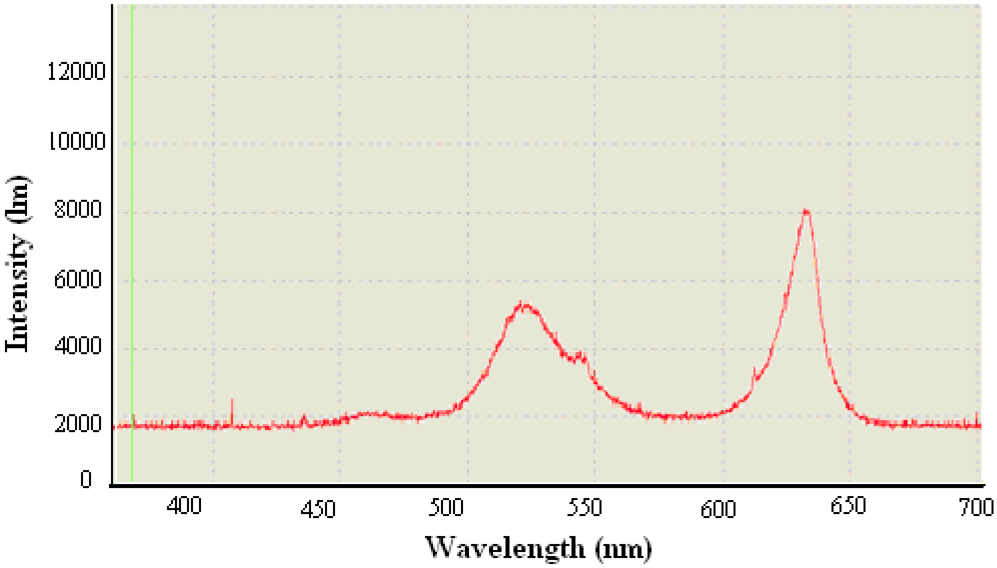

(b)

Figure 5.4. Spectrum of Yellow using (a) RGBW and (b) RGB

Table 5.1. Peak intensities in radiant flux units corresponding to R (612nm), G (547nm) and B(460nm) for RGB and RGBW configurations.

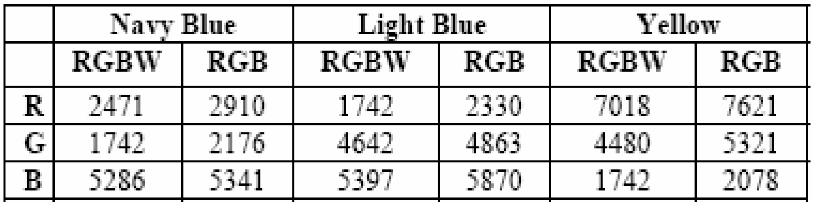

	Navy Blue		Light Blue		Yellow	
	RGBW	RGB	RGBW	RGB	RGBW	RGB
R	2471	2910	1742	2330	7018	7621
G	1742	2176	4642	4863	4480	5321
B	5286	5341	5397	5870	1742	2078

Table 5.1 shows the monochromatic intensity measurements at the primary colors for RGB and RGBW. These values are obtained from the spectrometer readings shown in Figures 5.2 - 5.4. From the figures, it is clear that the intensity spectrum distributions of the measured colors are very similar in wave form. The values in Table 5.1 demonstrate the colors to have the same proportions among the monochromatic waves for every primary color (RGB) which shows that the colors displayed using RGB have the same hue as the colors displayed using RGBW; however, it is noticeable that the overall intensity of the spectra exhibits a small difference between the RGB and RGBW. This is due to the architecture of the prototype, which does not allow a separate calibration control for the white LEDs.

5.2 Human Perception Experiments

5.2.1 Experimental Procedure

This part of the study required a special approval (refer to Appendix II) since human subjects were involved. In order to test how people perceive the difference between the old (RGB) and the new (RGBW) LED display architectures, it was necessary to conduct an experimental survey involving a sample of people. To obtain the approval, the

Institutional Review Board (IRB) reviews the research project which involves human subjects to ensure subjects are not at unjustified risk and that test subjects are given informed consent at the time of participation. Furthermore, researches have to undergo IRB training through the collaborative institutional training initiative (CITI) which offers different types of training. This requirement is designed to provide information and guidance to researchers in order to minimize risks.

Subjects were selected at random; recruiting was done at UNLV, an educational institution; therefore, majority of subjects were students between the ages of 18 and 30. Vast majority of students were willing to take the survey directly after briefly explaining to them about the experiment. They were told that they would have to compare colors displayed using an LED display and make a note of differences they notice. Upon their arrival to the laboratory were the experiment was conducted, more detailed instructions were given to them as well as a handout that contains detailed directions (refer to Appendix III for the informed consent), the approval and the survey questions (refer to Appendix IV).

Twelve pairs of different colors were tested. The colors fall into three groups, gray scale, low saturation, and high saturation. Every subject was shown pairs of colors and asked to determine whether the colors are:

(a) Identical = 98% or more similarity

(b) Almost the same = 90% or more similarity (the same hue)

(c) Not the same at all = less than 90%

(d) Unsure

Three different sets of experiments were conducted. In the first set, the experimental group, each color was displayed twice once with RGB and once with RGBW. There were 100 subjects in this category. In the second set, each color was displayed twice with RGB. This set is one of the control groups and had 20 subjects. In the third set, each color was displayed twice with RGBW and it is the second control group which also had 20 subjects. The purpose of the control groups of sets 2 and 3 was to assess the reliability or consistency of the results obtained in set 1.

5.2.2 Results and Discussion

Data of human perception for gray scale, low saturation colors, and high saturation colors are shown in Tables 5.2 – 5.4, respectively.

Table 5.2 Human Perception data for gray scale (i) White (ii) Gray and (iii) Dark Gray where (a) Identical, (b) Almost the same, (c) Not the same, (d) Unsure

White	a	b	c	d	Total
RGB-RGBW	7	37	56		100
RGB	15	5			20
RGBW	14	6			20

(i)

Gray	a	b	c	d	Total
RGB-RGBW	3	31	66		100
RGB	13	6	1		20
RGBW	11	9			20

(ii)

Dark Gray	a	b	c	d	Total
RGB-RGBW	10	55	35		100
RGB	10	8	2		20
RGBW	12	7	1		20

(iii)

In the experiment involving gray scale, it appears that most subjects perceived colors to be not the same. For the same reasons mentioned in section 5.1 which confirms the data obtained from the spectrometer. Due to the architecture of the prototype, which does not allow a separate calibration control for the white LEDs, gray scale shows the most inconsistent data.

Table 5.3 Human Perception data for low saturated colors (i) Purple (ii) Purplish Blue (iii) Medium Green and (iv) Yellow where (a) Identical, (b) Almost the same, (c) Not the same, (d) Unsure.

Purple	a	b	c	d	Total
RGB-RGBW	10	72	18		100
RGB	6	10	4		20
RGBW	13	6	1		20

(i)

Purplish Blue	a	b	c	d	Total
RGB-RGBW	16	65	19		100
RGB	11	9			20
RGBW	13	7			20

(ii)

Medium Green	A	b	c	d	e
RGB-RGBW	25	68	7		100
RGB	12	8			20
RGBW	14	6			20

(iii)

Yellow	a	b	c	d	Total
RGB-RGBW	15	68	17		100
RGB	12	8			20
RGBW	13	6	1		20

(iv)

Most subjects found low saturated colors to be almost the same. Keeping in mind that low saturation is equivalent to a high white value in the color, it is expected of test subjects to notice a minor difference between the RGB and RGBW colors.

Table 5.4 Human Perception data for high saturated colors (i) Rose (ii) Violet (iii) Cyan (iv) Green and (v) Orange where (a) Identical, (b) Almost the same, (c) Not the same, (d) Unsure

Rose	a	b	c	d	Total
RGB-RGBW	59	39	2		100
RGB	12	8			20
RGBW	12	8			20

(i)

Violet	A	b	c	d	Total
RGB-RGBW	62	36	2		100
RGB	10	9	1		20
RGBW	15	5			20

(ii)

Cyan	A	b	c	d	Total
RGB-RGBW	73	26	1		100
RGB	13	7			20
RGBW	16	4			20

(iii)

Green	A	b	c	d	Total
RGB-RGBW	48	52	0		100
RGB	15	4	1		20
RGBW	16	4			20

(iv)

Orange	A	b	c	d	Total
RGB-RGBW	35	61	4		100
RGB	10	9	1		20
RGBW	17	3			20

(v)

Most subjects found high saturated colors to be identical or almost the same. On the contrary of low saturation, high saturation means a low white value in the color; therefore, it is expected of test subjects to hardly notice any difference between the RGB and RGBW colors.

5.2.3 Statistical Analysis

5.2.3.1 Theory of Statistical Analysis

The binomial probability model is appropriate for the data collected from Experiments 1, 2, and 3, as the following will show. Let X denote the number of subjects out of N_j for Experiment *j (j* = 1, 2, 3) who thought that the colors produced were 'Identical or Almost the Same'. The probability distribution of X then can be modeled by the binomial probability distribution:

$$P(X = x) = \binom{N}{x} p_j^x (1 - p_j)^x, x = 1,2,\ldots,N \tag{5.1}$$

where pj is the proportion of subjects in the population who think that the colors produced in two trails are 'identical or almost the same'. The population proportion p_j is estimated by the sample proportion

$$\hat{p}_j = \frac{x_j}{N_j} \tag{5.2}$$

where x_j is the number of subjects who thought the colors in two trials were identical, for experiment j (j = 1, 2, 3). Confidence intervals for p_j can be computed using the following approximate formula for 95% confidence:

$$p_j(95\% Confidence - Intervals) = \hat{p}_j \pm 1.96 \times \sqrt{\frac{\hat{p}_j(1 - \hat{p}_j)}{N_j}} \tag{5.3}$$

Exact confidence intervals can also be calculated using the software package MINITAB. The later approach is used in this work. The 95% confidence interval for p_j has the property that the repeated use of the formula for computing the 95% confidence interval, over similar experiments, will contain the true unknown p_j 95% of the times.

5.2.3.2 Data Analysis

Using data presented in Table 5.2 and equation 5.3 the estimate, p_j and the upper and lower 95% confidence intervals were calculated using MINITAB and reported in Table 5.5 for white, gray, and dark gray. The data for “almost the same” and “Identical” were combined to obtain the estimate, p_j. Thus, values of $\hat{p}_j$ indicate that the pair of colors appear the same. The 95% confidence intervals (U95, L95) indicate the spread or the variability of data.

Table 5.5 $\hat{p}$, L95, and U95 values after the statistical analysis of the data for gray scale.

	WHITE RGB-RGBW	WHITE RGB	WHITE RGBW	GRAY RGB-RGBW	GRAY RGB	GRAY RGBW	DARK GRAY RGB-RGBW	DARK GRAY RGB	DARK GRAY RGBW
L95	0.34	0.86	0.86	0.25	0.75	0.86	0.55	0.68	0.75
$\hat{p}$	0.44	1	1	0.34	0.95	1	0.65	0.9	0.95
U95	0.54	1	1	0.44	0.99	1	0.74	0.99	0.99

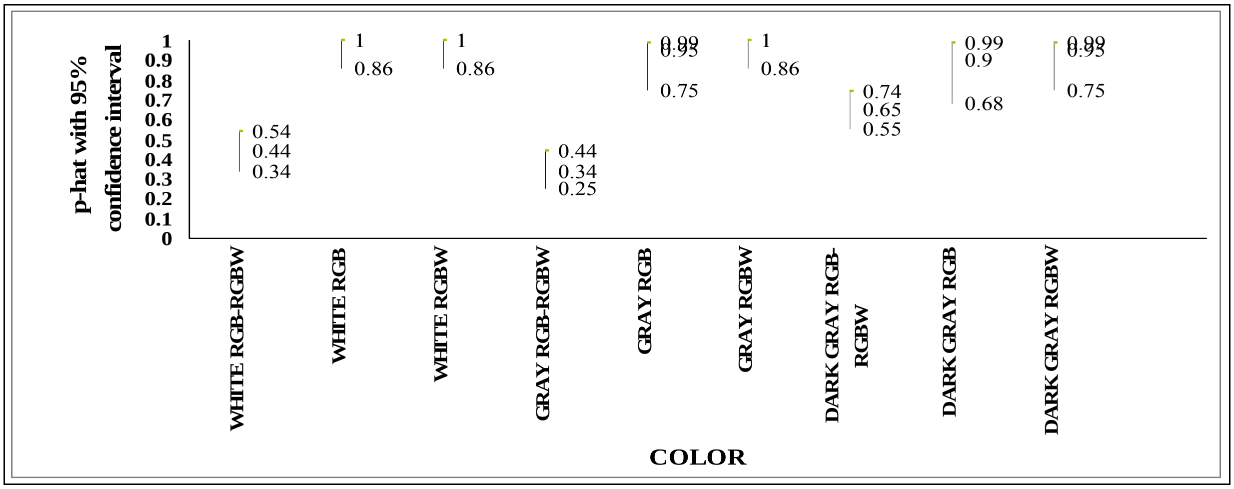

Figure 5.5 Estimate, $\hat{p}$, with 95% confidence interval for White, Gray, and Dark Gray.

It appears that white color created by RGB, as shown in Table and Figure 5.5, is perceived the same as that by RGBW only to 44% ± 10% of the subjects and only 34% ± 10% for gray. The reason for obtaining percentages below 50% stems from the fact that the white LEDs in the prototype that was used for this experiment did not have independent intensity control; thus, maintaining an equivalent intensity between the two whites was a challenge. Since gray has low saturation, the amount of white in it is fairly high, which explains why the data is below 50%. For dark gray, however, the percentage of subjects that found the colors generated by RGB and RGBW to be the same significantly increased to be 65% +9% /-10% since the white level decreases for high saturated colors.

Table 5.6 $\hat{p}$, L95, and U95 values after the statistical analysis of the data for low saturated colors.

	PURPLE RGB-RGBW	PURPLE RGB	PURPLE RGBW	PURPLISH BLUE RGB-RGBW	PURPLISH BLUE RGB	PURPLISH BLUE RGBW	MEDIUM GREEN RGB-RGBW	MEDIUM GREEN RGB	MEDIUM GREEN RGBW
L95	0.73	0.56	0.75	0.72	0.86	0.86	0.86	0.86	0.86
$\hat{p}$	0.82	0.8	0.95	0.81	1	1	0.93	1	1
U95	0.89	0.94	0.99	0.88	1	1	0.97	1	1

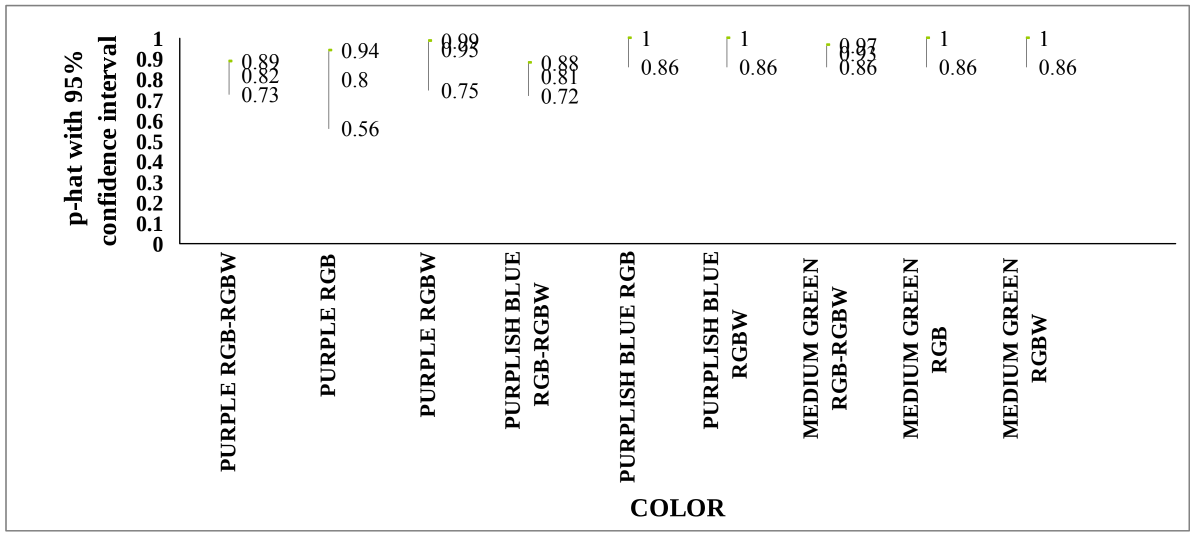

Figure 5.6 Estimate, $\hat{p}$, with 95% confidence interval for Purple, Purplish blue, and Medium Green.

As shown in Figure 5.2 and Figure 5.3, the percentages are dramatically improved compared to the gray scale. 82% (+6% /-9%) of test subjects for purple, 81% (+7% /-9%) for purplish blue, and 93% (+4% /-7%) for medium green found the difference between RGB and RGBW to be "almost the same or identical". This increase in percentage was expected since adding the right amount of white, as it was illustrated in the previous chapter section 4.3, does not change the hue of the perceived color.

Table 5.7 $\hat{p}$, L95, and U95 values after the statistical analysis of the data for yellow and high saturated colors.

	YELLOW RGB-RGBW	YELLOW RGB	YELLOW RGBW	ROSE RGB-RGBW	ROSE RGB	ROSE RGBW	VIOLET RGB-RGBW	VIOLET RGB	VIOLET RGBW
L95	0.74	0.86	0.75	0.93	0.86	0.86	0.93	0.75	0.86
$\hat{p}$	0.83	1	0.95	0.98	1	1	0.98	0.95	1
U95	0.89	1	0.99	0.99	1	1	0.99	0.99	1

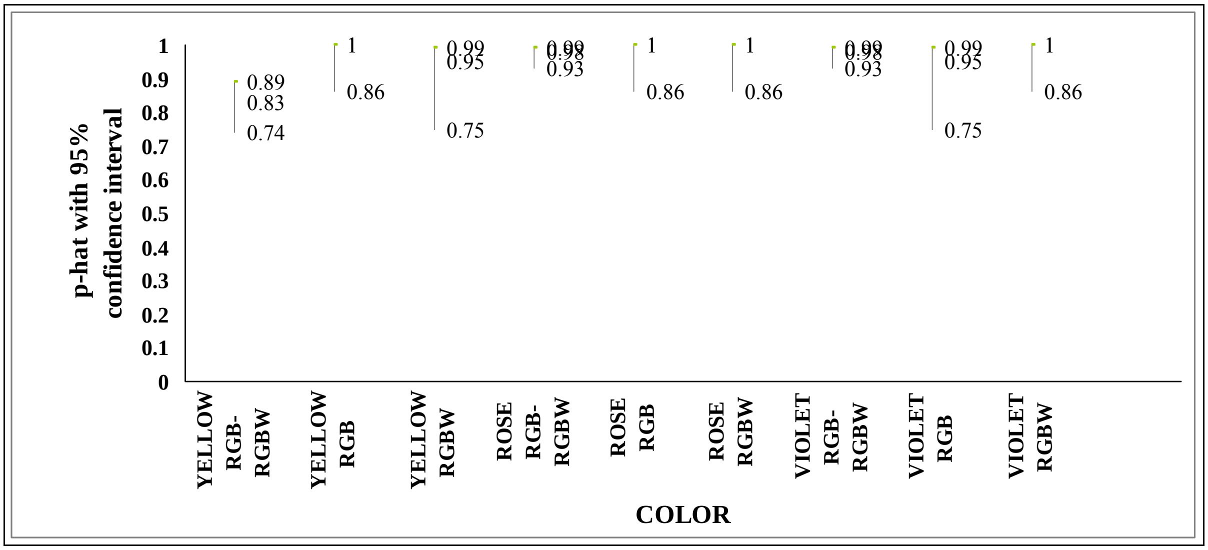

Figure 5.7 Estimate, $\hat{p}$, with 95% confidence interval for Yellow, Rose, and Violet.

The percentages for high saturated colors, as shown in Table 5.7-5.8 and Figure 5.7-5.8, seem to be very promising obtaining more than 95%. It is shown that 98% (+0% /-5%) of test subjects for rose, 98% (+0% /-5%) for violet, 99% (+0% /-4%) for CYAN, 100% (+0% /-3%) for green, and 96% (+2% /-6%) for orange found almost no difference between the colors when displayed using RGB and RGBW. This indicates that it is very difficult to differentiate between the two architectures (RGB and RGBW) for high saturated colors since the amount of white used in high saturated colors is minimal.

Table 5.8 $\hat{p}$, L95, and U95 values after the statistical analysis of the data for high saturated colors

	CYAN RGB-RGBW	CYAN RGB	CYAN RGBW	GREEN RGB-RGBW	GREEN RGB	GREEN RGBW	ORANGE RGB-RGBW	ORANGE RGB	ORANGE RGBW
L95	0.95	0.86	0.86	0.97	0.75	0.86	0.9	0.75	0.86
$\hat{p}$	0.99	1	1	1	0.95	1	0.96	0.95	1
U95	0.99	1	1	1	0.99	1	0.98	0.99	1

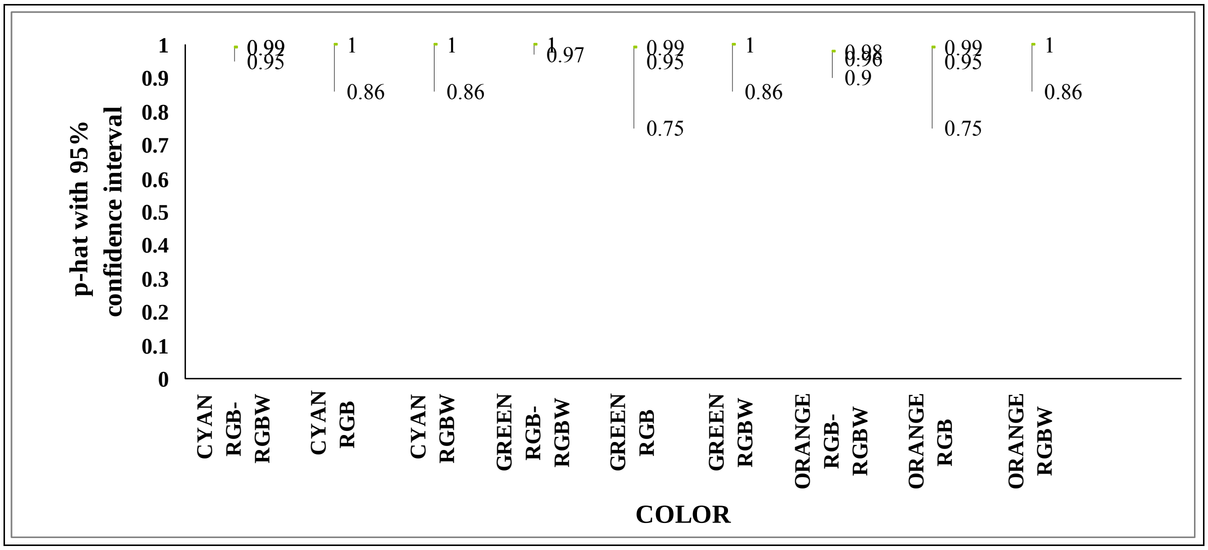

Figure 5.8 Estimate, $\hat{p}$, with 95% confidence interval for Cyan, Green, and Orange.

5.3 Energy Measurements and Calculations

5.3.1 Experimental Procedure

Since the power consumed is directly proportional to current supplied due to constant voltage, twelve pairs of different colors are tested. The colors are divided into three groups gray scale, low saturation, and high saturation. For every pair, the current supplied to the 8x8 pixel display is measured twice once for RGB and once for RGBW.

5.3.2 Results and Discussion

The currents consumed by the 8x8 pixel LED display are measured for the twelve pairs of colors using RGB and RGBW and listed in Table 5.9. It is noted that the current values are in the range of 0.63 - 1.78A where the highest values are consumed by white and the lowest values by dark gray.

Table 5.9 Measured currents for RGB, RGBW

	I (RGB) [A]	I (RGBW) [A]
White	1.78	0.91
Gray	1.4	0.93
Dark Gray	0.66	0.39
Purple	1.32	0.88
Purplish Blue	0.92	0.63
Medium Green	1.21	0.7
Yellow	1.27	0.86
Rose	1.06	0.91
Violet	1.16	1.06
Cyan	1.27	1.16
Green	1.15	1
Orange	1.24	1.16

5.3.3 Data Analysis

The power consumed by the LED display, P, is given by:

$$P = V \times I \qquad (5.4)$$

where V is the voltage supplied to the device, and I is the Current through the device. In this study, the voltage of operation used was 3.3v which is the required voltage by the system.

The percentage of power savings as a result of using RGBW instead of RGB, P_s, is given by:

$$\% P_s = (P_{RGB} - P_{RGBW}) / P_{RGB} \times 100 \tag{5.5}$$

Table 5.10 Power consumed by pixels for RGB, RGBW and % power savings of RGBW over RGB.

	P (RGB) [W]	P(RGBW) [W]	P savings %
White	5.87	3.00	49
Gray	4.62	3.07	34
Dark Gray	2.18	1.29	41
Purple	4.36	2.90	33
Purplish Blue	3.04	2.08	32
Medium Green	3.99	2.31	42
Yellow	4.19	2.84	32
Rose	3.5	3.00	14
Violet	3.83	3.5	9
Cyan	4.19	3.83	9
Green	3.8	3.3	13
Orange	4.09	3.83	6

Using the data reported in table 5.9 and the equations 5.4 and 5.5, P_{RGB}, P_{RGBW}, and $\%P_s$ were calculated and reported in Table 5.10 for twelve colors. % power saving for various colors is plotted in Figure 5.9

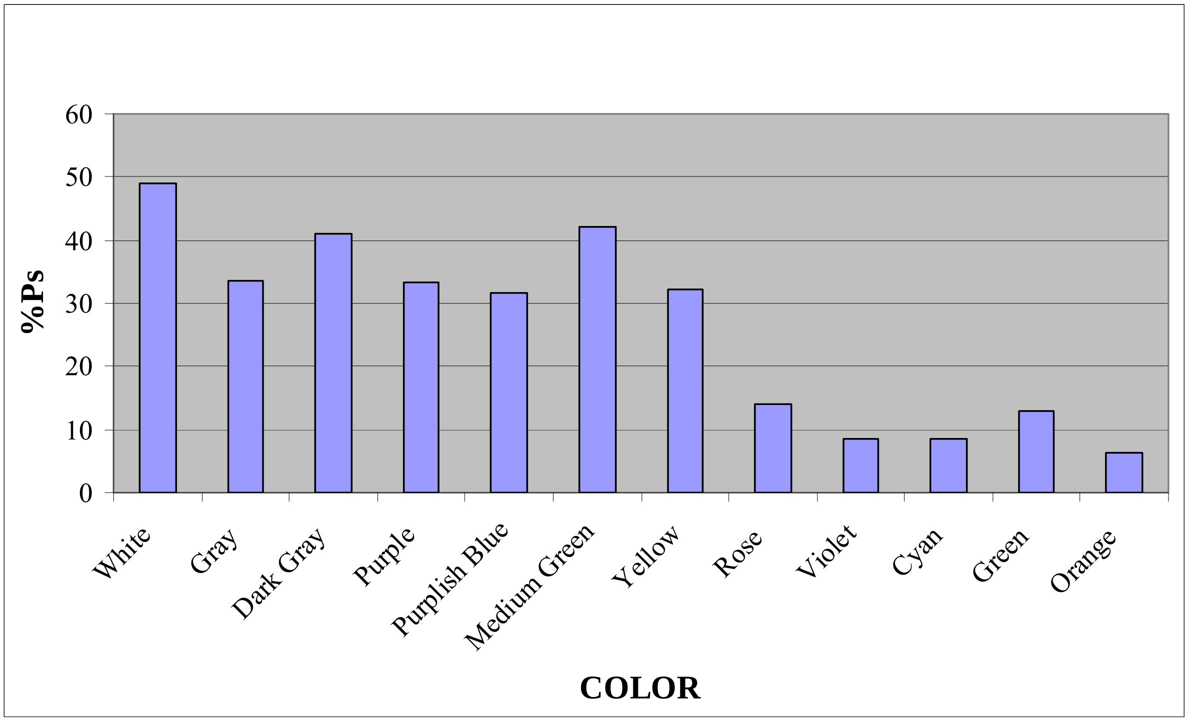

Figure 5.9 The % power savings for twelve colors

The data presented in Figure 5.9 shows power savings that ranges between 30% and 50% for gray scale and low saturated colors (purple, purplish blue, medium green, and yellow). Power savings for high saturated colors, such as rose, violet, cyan, green, and orange, is much lower than power savings for the gray scale and the low saturated colors. The low percentages for high saturated colors stems from the fact that the compensating white level of such colors is minimal. As expected, using the new RGBW pixel architecture saves power in most cases, i.e., gray scale, high saturation, and low saturation colors.

5.4 Colors from Display

Photographs were taken of twelve different colors generated by RGB and RGBW and are displayed next to one another in Figures 5.10-5.12. Photograph in (a) corresponds to RGB and that in (b) corresponds to RGBW.

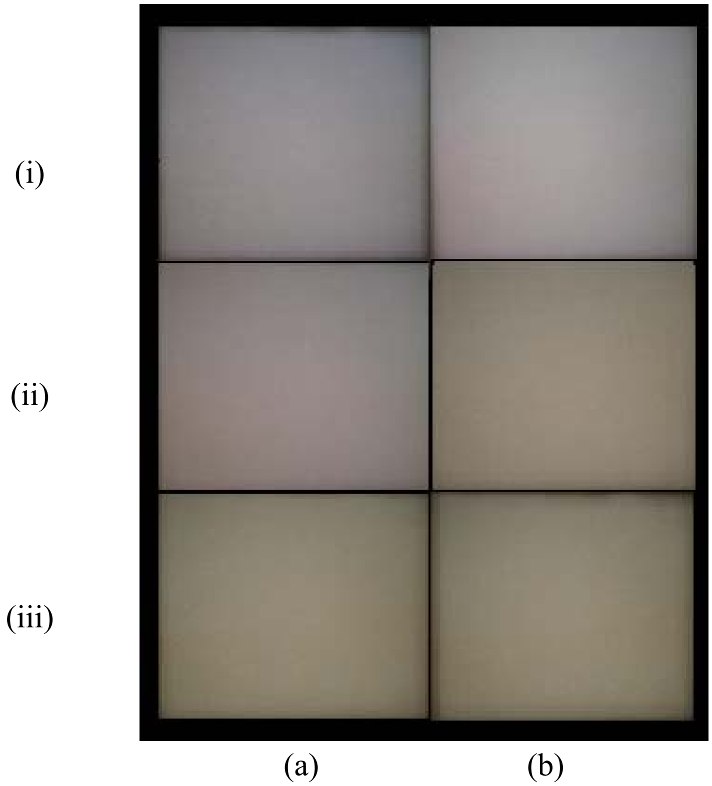

Figure 5.10 A photograph of gray scale colors from (a) RGB (b) RGBW (i) white (ii) gray (iii) dark gray.

For the photograph of gray scale shown in Figure 5.10, it is noted that colors displayed with RGB seem to be slightly brighter than colors displayed with RGBW. This is due to the fact that the white generated from RGB and the white generated from RGBW are some what different as seen in the spectrometer reading in Figure 5.1.

Column (a) seems to be brighter than (b).

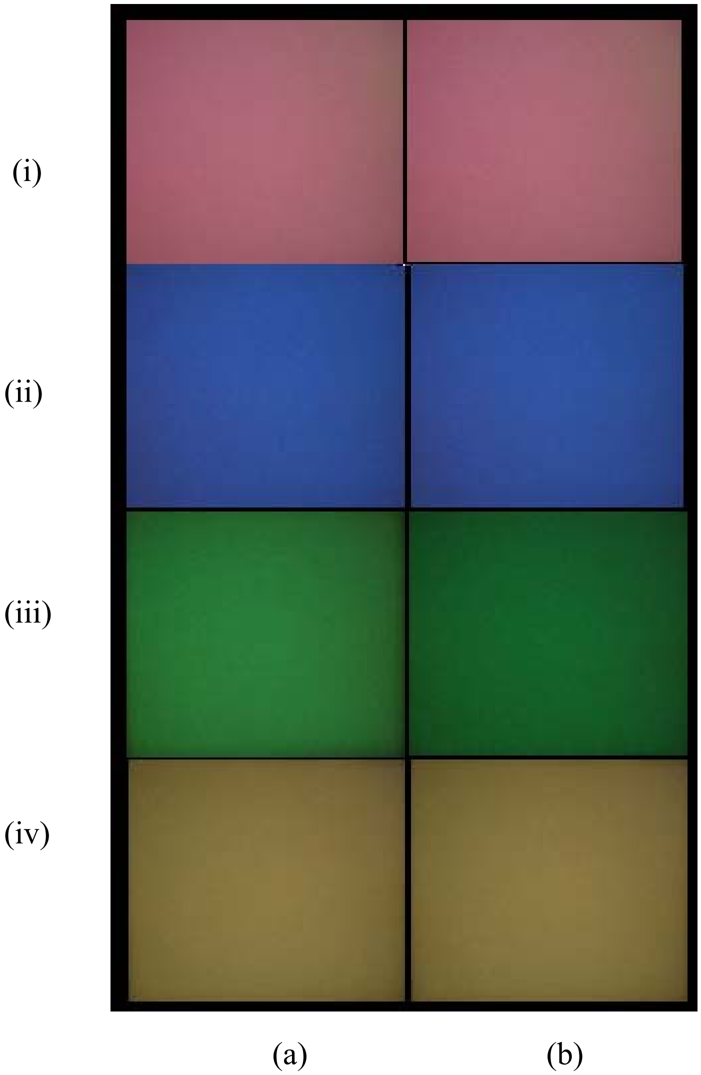

Figure 5.11 A photograph of low saturated colors from (a) RGB (b) RGBW (i) purple (ii) purplish blue (iii) medium green (iv) yellow.

Low saturated colors are shown in Figure 5.11. Photographs for RGB and RGBW for all colors appear to be very close; however, it is noticeable that column (a) is brighter than column (b) since the component of white is high in low saturated colors. A photograph of high saturated colors is shown in Figure 5.12. Colors in this photograph are also indistinguishably similar since the white component is low for this category of colors.

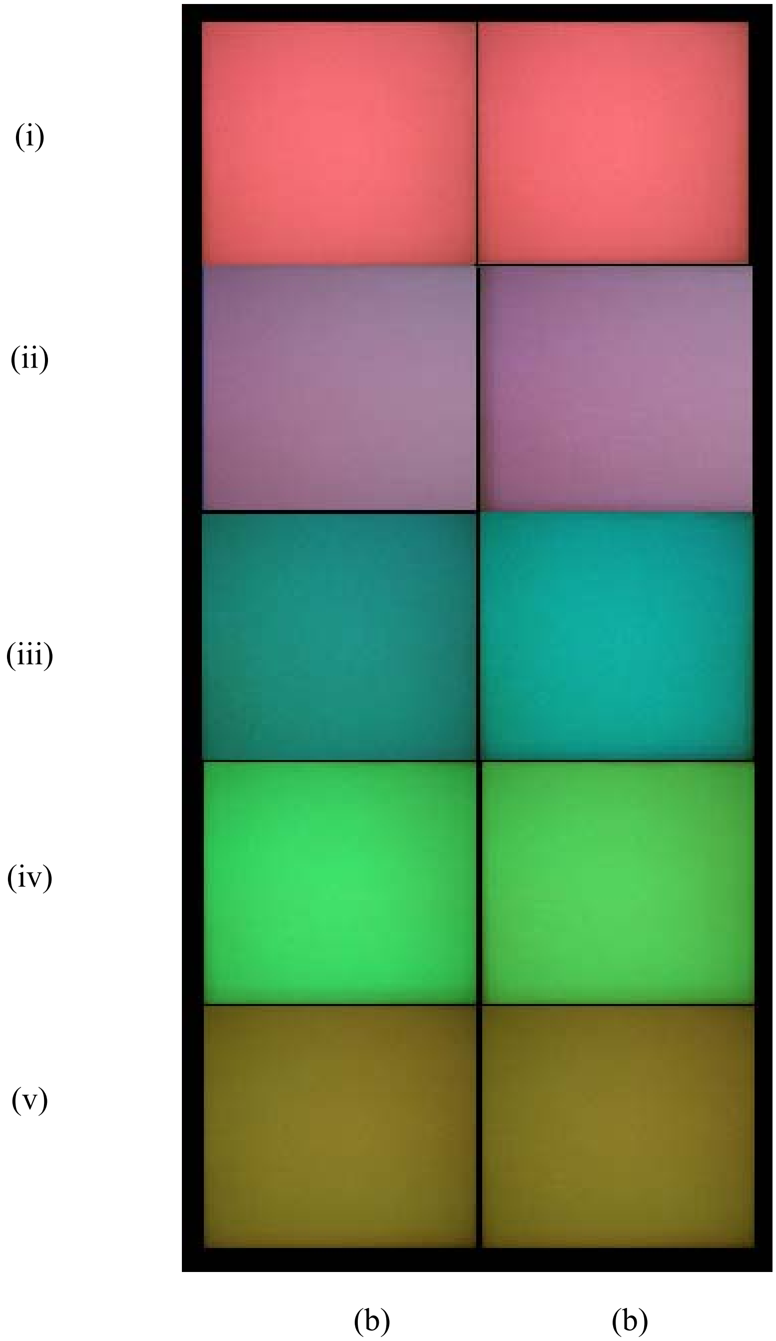

Figure 5.12 A photograph of high saturated colors from (a) RGB (b) RGBW (i) rose (ii) violate (iii) cyan (iv) green (v) orange.

CHAPTER 6

CONCLUSIONS AND RECOMMENDATIONS

In this work, a novel pixel configuration RGBW, consisting of red (R), green (G), blue (B), and white (W) LEDs, was employed and investigated for color generation. Energy consumption and various hues of new pixels were compared to standard pixels consisting of RGB LEDs. Human perception experiments were conducted in order to study the perceptual difference between the two architectures when colors are generated using RGBW vs. RGB. Various experimental approaches were considered such as spectrometric readings, human perception experiment, and theoretical analysis in order to verify that the hue is maintained with the new architecture. The spectrometer reading has shown that the spectrum of the colors generated using RGB and RGBW are similar. Furthermore, statistics has shown that 44% of test subjects found the colors in gray scale to be the same, whereas 82% and 95% of test subject found low saturated colors and high saturated colors, respectively, to be identical. Theoretical analysis of the new RGBW pixel based on fundamentals of color theory has shown that using RGBW will not change the hue when it replaces RGB. Real life captions were included demonstrating that the colors are almost indistinguishable. Power measurements for an 8x8 pixel LED display has demonstrated power savings, in all cases, using RGBW. The percentage of saved power, however, differed from one case to another, for instance using RGBW as an alternative achieved up to 49% power savings for gray scale, over 30% power savings for low saturated colors, and up to 12% for high saturated colors. Most colors have witnessed over 30% power savings.

Future research may include:

- Using the white LED in the pixel along with the RGB in order to create a brighter and sharper image.
- Developing a smart pixel where it would determine the cases where using the white LED is more efficient than RGB and operates accordingly.
- The resolution of the RGBW LED display can improve by studying different LED configurations for pixels such as RGB surrounding the white LED.
- Using the centered triangle configuration of RGBW with a white LED at the center of an equilateral triangle and study its performance against square configuration studied in this thesis.

APPENDIX I

AHDL CODE OF THE SOFTWARE IMPLIMENTATION

```
SUBDESIGN HVsync
(

Clk, q[9..0]                                    :INPUT;
HSyncIn, Hblk, Vs, Vblk, Vcnt[9..0], HBlank8 : OUTPUT;
VBlank8                 :OUTPUT;

)
variable

Hsff, Hblank, Vsff, Vblank, Shb, Svb, Shb8, Svb8 :JKFF;
vcount[9..0]                                          :DFF;


begin

Hsff.clk        =       Clk;
Hsff.j          =       q[] == 736;
Hsff.k          =       q[] == 781;

Hblank.clk      =       Clk;
Hblank.j        =       q[] == 0;
Hblank.k        =       q[] == 720;

Shb.clk                 =       Clk;
Shb.j           =       q[] == 360;
Shb.k           =       q[] == 376;

Shb8.clk        =       Clk;
Shb8.j          =       q[] == 362;
Shb8.k          =       q[] == 370;


HSyncIn                 =       !Hsff;
%Hblk           =       Hblank;%
```

```
Hblk            =          Shb;
HBlank8                    =          Shb8;

vcount[].clk    =          Hsff;
if vcount[]     == 525 then
vcount[]                   = 0;
else vcount[].d = vcount[].q +1;
end if;

Vsff.clk        =          Hsff;
Vsff.j          =          vcount[] == 495;
Vsff.k          =          vcount[] == 498;

Vblank.clk      =          Hsff;
Vblank.j        =          vcount[] == 0;
Vblank.k        =          vcount[] == 479;

Svb.clk                    =          Hsff;
Svb.j           =          vcount[] == 240;
Svb.k           =          vcount[] == 256;

Svb8.clk                   =          Hsff;
Svb8.j          =          vcount[] == 244;
Svb8.k          =          vcount[] == 252;

Vs                         =          Vsff;
%Hblk           =          Vblank;%
Vblk            =          Svb;
VBlank8                    =          Svb8;

Vcnt[]          =          Vcount[];

end;


SUBDESIGN VChbvbGEN
(
          -- {{ALTERA_IO_BEGIN}} DO NOT REMOVE THIS LINE!
          VCclk : INPUT;
          VCHsync : INPUT;
          VCVsync : INPUT;
          VCCblank : OUTPUT;
          VCcnth[9..0] : OUTPUT;
          VCcntv[9..0] : OUTPUT;
          -- {{ALTERA_IO_END}} DO NOT REMOVE THIS LINE!
)
```

```
variable

        cnth[9..0]              :dff;
        cntv[9..0]              :dff;
        blankh                  :jkff;
        blankv                  :jkff;

begin

        cnth[].clk   =   VCclk;
        cnth[].clrn  =   VCHsync;
        cnth[].d         =   cnth[].q +1;

        VCcnth[9..0] =   cnth;

        blankh.clk       =   VCclk;
        blankh.j         =   cnth[] == 362;
        blankh.k         =   cnth[] == 370;



        cntv[].clk       =          VCHsync;
        cntv[].d         =   cntv[].q + 1;
        cntv[].clrn  =   VCVsync;

        VCcntv[9..0] =   cntv;

        blankv.clk       =   VCHsync;
        blankv.j         =   cntv[] == 244;
        blankv.k         =   cntv[] == 252;

        VCCblank         =  blankv and blankh;

end;

SUBDESIGN Condotta1
(
        -- {{ALTERA_IO_BEGIN}} DO NOT REMOVE THIS LINE!
        address0 : INPUT;
        address1 : INPUT;
        address2 : INPUT;
        address3 : INPUT;
        address4 : INPUT;
        address5 : INPUT;
        sw17 : INPUT;
```

```
	addrout[5..0] : OUTPUT;
	-- {{ALTERA_IO_END}} DO NOT REMOVE THIS LINE!
)

Begin
if sw17 == 1 then
	addrout[5..0] = address[5..0];
else
	addrout[5..0]	=	56;
end;

--if sw17==1 then
--	addrout[5..0]	=	address[5..0];
--end;

End;


SUBDESIGN EnableGen
(
	-- {{ALTERA_IO_BEGIN}} DO NOT REMOVE THIS LINE!
	HSync : INPUT;
	VSync : INPUT;
	Clk : INPUT;
	Vcnt[9..0] : INPUT;
	q[9..0] : INPUT;
	DPst2rdEn : OUTPUT;
	FIFOrdEn : OUTPUT;
	DPst1wrEn : OUTPUT;
	DPst1rdEn : OUTPUT;
	LEDisp : OUTPUT;
	OEDisp : OUTPUT;
	BitSel[2..0] : OUTPUT;
	-- {{ALTERA_IO_END}} DO NOT REMOVE THIS LINE!
)


variable

counth[9..0], countv[9..0], FIFOrd, delay1, DPst1rd, DPst2rd, LEDispd,OEDispd,
BitSelC[2..0]		:dff;
FIFOrdh, FIFOrdv, DPst1rdh, DPst1rdv, DPst2rdh, DPst2rdv, LEDispdh, LEDispdv,
OEDispdh, OEDispdv		:jkff;


begin
```

```
--Main counters
--counth[].clk  =         Clk;
--counth[].clrn=          HSync;
--counth[].d              =         counth[].q + 1;


--countv[].clk  =         HSync;
--countv[].clrn=          !VSync;
--countv[].d              =         countv[].q + 1;

BitSelC[].clk   =         Clk;

if Vcnt[] >= 1 and Vcnt[] < 3  then
BitSelC[].d = 0;

elsif Vcnt[] >= 3 and Vcnt[] < 6 then
BitSelC[].d = 1;

elsif Vcnt[] >= 6 and Vcnt[] < 11 then
BitSelC[].d = 2;

elsif Vcnt[] >= 11 and Vcnt[] < 20 then
BitSelC[].d = 3;

elsif Vcnt[] >= 20 and Vcnt[] < 37 then
BitSelC[].d = 4;

elsif Vcnt[] >= 37 and Vcnt[] < 71 then
BitSelC[].d = 5;

elsif Vcnt[] >= 71 and Vcnt[] < 139 then
BitSelC[].d = 6;

elsif Vcnt[] >= 139 and Vcnt[] < 273 then
BitSelC[].d = 7;

end if;

BitSel = BitSelC;



------------------------------
FIFOrdh.clk               =         Clk;
--FIFOrdh.clrn=           HSync;
FIFOrdh.j                 =         q[] == 400;
```

```
FIFOrdh.k          =      q[] == 464;
FIFOrdv.clk        =      !HSync;
--FIFOrdv.clrn=    !VSync;
FIFOrdv.j          =      Vcnt[] == 255;
FIFOrdv.k          =      Vcnt[] == 256;

FIFOrd.clk         =      Clk;
FIFOrd.d           =      FIFOrdh and FIFOrdv;

FIFOrdEn           =      FIFOrd;

------------------------------

delay1.clk         =      Clk;
delay1.d           =      FIFOrd;

DPst1wrEn          =      delay1;

-------------------------------
DPst1rdh.clk  =    Clk;
--DPst1rdh.clrn    =      HSync;
DPst1rdh.j         =      q[] == 471;
DPst1rdh.k         =      q[] == 599;

DPst1rdv.clk  =    !HSync;
--DPst1rdv.clrn    =      !VSync;
DPst1rdv.j         =      Vcnt[] == 256;
DPst1rdv.k         =      Vcnt[] == 257;

DPst1rd.clk        =      Clk;
DPst1rd.d          =      DPst1rdh and DPst1rdv;

DPst1rdEn          =      DPst1rd;

-------------------------------
-------------------------------
DPst2rdh.clk  =    Clk;
--DPst2rdh.clrn    =      HSync;
DPst2rdh.j         =      q[] == 1;
DPst2rdh.k         =      q[] == 33;
-------------------------------
LEDispdh.clk  =    Clk;
--LEDispdh.clrn    =      HSync;
LEDispdh.j         =      q[] == 137;
LEDispdh.k         =      q[] == 138;
-------------------------------
```

```
OEDispdh.clk =        Clk;
--LEDispdh.clrn       =       HSync;
OEDispdh.j            =       q[] == 0;
OEDispdh.k            =       q[] == 858;
-------------------------------
-------------------------------

---------------------------------
---------------------------------
--Bit0
---------------------------------
DPst2rdv.clk   =      !HSync;
--DPst2rdv.clrn       =       !VSync;
DPst2rdv.j            =       Vcnt[] == 1;
DPst2rdv.k            =       Vcnt[] == 2;
----------------------------------
LEDispdv.clk =        !HSync;
--LEDispdv.clrn       =       !VSync;
LEDispdv.j            =       Vcnt[] == 1;
LEDispdv.k            =       Vcnt[] == 2;
----------------------------------
OEDispdv.clk =        !HSync;
--LEDispdv.clrn       =       !VSync;
OEDispdv.j            =       Vcnt[] == 2;
OEDispdv.k            =       Vcnt[] == 3;
----------------------------------
----------------------------------



---------------------------------
---------------------------------
--Bit1
---------------------------------
DPst2rdv.clk   =      !HSync;
--DPst2rdv.clrn       =       !VSync;
DPst2rdv.j            =       Vcnt[] == 3;
DPst2rdv.k            =       Vcnt[] == 4;
----------------------------------
LEDispdv.clk =        !HSync;
--LEDispdv.clrn       =       !VSync;
LEDispdv.j            =       Vcnt[] == 3;
LEDispdv.k            =       Vcnt[] == 4;
----------------------------------
OEDispdv.clk =        !HSync;
--LEDispdv.clrn       =       !VSync;
OEDispdv.j            =       Vcnt[] == 4;
```

```
OEDispdv.k          =       Vcnt[] == 6;
---------------------------------
---------------------------------
--Bit2
---------------------------------
DPst2rdv.clk   =        !HSync;
--DPst2rdv.clrn         =       !VSync;
DPst2rdv.j          =       Vcnt[] == 6;
DPst2rdv.k          =       Vcnt[] == 7;
----------------------------------
LEDispdv.clk =        !HSync;
--LEDispdv.clrn         =       !VSync;
LEDispdv.j          =       Vcnt[] == 6;
LEDispdv.k          =       Vcnt[] == 7;
----------------------------------
OEDispdv.clk =        !HSync;
--LEDispdv.clrn         =       !VSync;
OEDispdv.j          =       Vcnt[] == 7;
OEDispdv.k          =       Vcnt[] == 11;
----------------------------------
----------------------------------



---------------------------------
---------------------------------
--Bit3
---------------------------------
DPst2rdv.clk   =        !HSync;
--DPst2rdv.clrn         =       !VSync;
DPst2rdv.j          =       Vcnt[] == 11;
DPst2rdv.k          =       Vcnt[] == 12;
----------------------------------
LEDispdv.clk =        !HSync;
--LEDispdv.clrn         =       !VSync;
LEDispdv.j          =       Vcnt[] == 11;
LEDispdv.k          =       Vcnt[] == 12;
----------------------------------
OEDispdv.clk =        !HSync;
--LEDispdv.clrn         =       !VSync;
OEDispdv.j          =       Vcnt[] == 12;
OEDispdv.k          =       Vcnt[] == 20;
----------------------------------
----------------------------------
---------------------------------
---------------------------------
--Bit4
```

```
---------------------------------
DPst2rdv.clk   =        !HSync;
--DPst2rdv.clrn         =        !VSync;
DPst2rdv.j              =        Vcnt[] == 20;
DPst2rdv.k              =        Vcnt[] == 21;
----------------------------------
LEDispdv.clk =          !HSync;
--LEDispdv.clrn         =        !VSync;
LEDispdv.j              =        Vcnt[] == 20;
LEDispdv.k              =        Vcnt[] == 21;
----------------------------------
OEDispdv.clk =          !HSync;
--LEDispdv.clrn         =        !VSync;
OEDispdv.j              =        Vcnt[] == 21;
OEDispdv.k              =        Vcnt[] == 37;
----------------------------------
----------------------------------



---------------------------------
---------------------------------
--Bit5
---------------------------------
DPst2rdv.clk   =        !HSync;
--DPst2rdv.clrn         =        !VSync;
DPst2rdv.j              =        Vcnt[] == 37;
DPst2rdv.k              =        Vcnt[] == 38;
----------------------------------
LEDispdv.clk =          !HSync;
--LEDispdv.clrn         =        !VSync;
LEDispdv.j              =        Vcnt[] == 37;
LEDispdv.k              =        Vcnt[] == 38;
----------------------------------
OEDispdv.clk =          !HSync;
--LEDispdv.clrn         =        !VSync;
OEDispdv.j              =        Vcnt[] == 38;
OEDispdv.k              =        Vcnt[] == 71;
----------------------------------
----------------------------------



---------------------------------
---------------------------------
--Bit6
---------------------------------
DPst2rdv.clk   =        !HSync;
```

```
--DPst2rdv.clrn       =       !VSync;
DPst2rdv.j            =       Vcnt[] == 71;
DPst2rdv.k            =       Vcnt[] == 72;
---------------------------------
LEDispdv.clk =        !HSync;
--LEDispdv.clrn       =       !VSync;
LEDispdv.j            =       Vcnt[] == 71;
LEDispdv.k            =       Vcnt[] == 72;
---------------------------------
OEDispdv.clk =        !HSync;
--LEDispdv.clrn       =       !VSync;
OEDispdv.j            =       Vcnt[] == 72;
OEDispdv.k            =       Vcnt[] == 139;
---------------------------------
---------------------------------



--------------------------------
--------------------------------
--Bit7
--------------------------------
DPst2rdv.clk   =      !HSync;
--DPst2rdv.clrn       =       !VSync;
DPst2rdv.j            =       Vcnt[] == 139;
DPst2rdv.k            =       Vcnt[] == 140;
---------------------------------
LEDispdv.clk =        !HSync;
--LEDispdv.clrn       =       !VSync;
LEDispdv.j            =       Vcnt[] == 139;
LEDispdv.k            =       Vcnt[] == 140;
---------------------------------
OEDispdv.clk =        !HSync;
--LEDispdv.clrn       =       !VSync;
OEDispdv.j            =       Vcnt[] == 140;
OEDispdv.k            =       Vcnt[] == 273;
---------------------------------
---------------------------------


------------------------------------------------
DPst2rd.clk           =       Clk;
DPst2rd.d             =       DPst2rdh and DPst2rdv;
DPst2rdEn             =       DPst2rd;

LEDispd.clk           =       Clk;
LEDispd.d             =       LEDispdh and LEDispdv;
LEDisp                                =       LEDispd;
```

```
OEDispd.clk         =       Clk;
OEDispd.d           =       OEDispdh and OEDispdv;
OEDisp                      =       OEDispd;



end;
```

APPENDIX II

BIOMEDICAL IRB – EXPEDITED REVIEW
APPROVAL NOTICE

NOTICE TO ALL RESEARCHERS:
Please be aware that a protocol violation (e.g., failure to submit a modification for any change) of an IRB approved protocol may result in mandatory remedial education, additional audits, re-consenting subjects, researcher probation suspension of any research protocol at issue, suspension of additional existing research protocols, invalidation of all research conducted under the research protocol at issue, and further appropriate consequences as determined by the IRB and the Institutional Officer.

DATE: July 9, 2008

TO: Dr. Rama Venkat, Electrical and Computer Engineering

FROM: Office for the Protection of Research Subjects

RE: Notification of IRB Action by Dr. John Mercer, Chair
Protocol Title: University of Nevada Light Emitting Diode Display Engineering (NV)
Protocol #: 0805-2740

This memorandum is notification that the project referenced above has been reviewed by the UNLV Biomedical Institutional Review Board (IRB) as indicated in regulatory statutes 45 CFR 46. The protocol has been reviewed and approved.

The protocol is approved for a period of one year from the date of IRB approval. The expiration date of this protocol is July 6, 2009. Work on the project may begin as soon as you receive written notification from the Office for the Protection of Research Subjects (OPRS).

PLEASE NOTE:
Attached to this approval notice is the official Informed Consent/Assent (IC/IA) Form for this study. The IC/IA contains an official approval stamp. Only copies of this official IC/IA form may be used when obtaining consent. Please keep the original for your records.

Should there be *any* change to the protocol, it will be necessary to submit a Modification Form through OPRS. No changes may be made to the existing protocol until modifications have been approved by the IRB.

Should the use of human subjects described in this protocol continue beyond July 6, 2009 it would be necessary to submit a Continuing Review Request Form *60 days* before the expiration date.

If you have questions or require any assistance, please contact the Office for the Protection of Research Subjects at OPRSHumanSubjects@unlv.edu or call 895-2794.

APPENDIX III

INFORMED CONSENT

INFORMED CONSENT

Department of Electrical and Computer Engineering

TITLE OF STUDY: University of Nevada Light Emitting Diode Display Engineering (NV)

INVESTIGATOR(S): Dr. Rama Venkat

Contact Phone Number: 895-1094

Purpose of the Study

You are invited to participate in a research study. The purpose of this study is to obtain data "how human beings perceive a variety of colors generated by two methods of LED Display lighting (Red-Green-Blue (RGB) & Red-Green-Blue-White(RGBW))".

Participants

You are being asked to participate in the study because the quality of display is a perceived characteristics and hence data based on human perception is absolutely necessary. If you know that you are color-blind, please let us know as the research involves viewing various colors generated by two different technologies we are comparing.

Procedures

If you volunteer to participate in this study, you will be asked to do the following:

- Sit 5 feet away from a 6 inch x 6 inch white screen where same color from two different technologies and sometimes the same technology will be displayed. Some of you will be assigned to the control group and others to experimental group. You will not know which group you belong to. Only the researcher will know.
- Observe the color and record on a form if the colors are:
  - (i) identical
  - (ii) almost the same
  - (iii) not at all the same.

- If you are not sure, then you can ask the researcher to repeat the procedure for another viewing of the colors.
- If you are uncomfortable with viewing the colors or any other part of the experimentation, you can withdraw by letting the researcher know.

Benefits of Participation

There may not be direct benefits to you as a participant in this study. However, we hope to learn if the new technology we are developing, which we know saves energy, provides the same quality of colors in a display.

Risks of Participation

There are risks involved in all research studies. This study may include only minimal risks. State the level of anticipated risks (i.e. you may become uncomfortable when answering some questions). Te study involves minimal risk only as the subjects will be viewing colors of same brightness as they see in real life. At any time during the experimentation, if the subject is uncomfortable and does not want to continue, he/she can withdraw by letting the researcher know.

Cost /Compensation

There will not be financial cost to you to participate in this study. The study will take 30 minutes of your time. You will not be compensated for your time.

Contact Information

If you have any questions or concerns about the study, you may contact Dr. Rama Venkat at 895 1094. For questions regarding the rights of research subjects, any complaints or comments regarding the manner in which the study is being conducted you may contact the UNLV Office for the Protection of Research Subjects at 702-895-2794.

Voluntary Participation

Your participation in this study is voluntary. You may refuse to participate in this study or in any part of this study. You may withdraw at any time without prejudice to your relations with the university. You are encouraged to ask questions about this study at the beginning or any time during the research study.

Confidentiality

All information gathered in this study will be kept completely confidential. No reference will be made in written or oral materials that could link you to this study. All records will be stored in a locked facility at UNLV for at least 3 years after completion of the study. After the storage time the information gathered will be deleted.

Participant Consent:

I have read the above information and agree to participate in this study. I am at least 18 years of age. A copy of this form has been given to me.

_______________________________ Date _______________

Signature of Participant

____

Participant Name (Please Print)

Participant Note: Please do not sign this document if the Approval Stamp is missing or is expired.

APPENDIX IV

HUMAN EXPERIMENT QUESTIONNAIRE

Questionnaire for the Subjects

Part 1

Circle "Yes" or "No" for the following questions.

1.	Are you 18 years or older (adult)?	Yes	No
2.	Are you color-blind (if know)?	Yes	No
3.	Are you sensitive to any colors?	Yes	No
4.	Are you sensitive to normal day-to-day light intensity?	Yes	No

Part 2

For each pair of colors that you are asked to view, please circle the appropriate answer of the three choices. If you are not sure, please ask the researcher to repeat the experiment.

Pair 1

Describe color 1: ______________________________
Describe color 2: ______________________________
Compare the colors:

a. Identical
b. Almost the same
c. Not at all the same
d. Unsure

Pair 2

Describe color 1: ______________________________
Describe color 2: ______________________________
Compare the colors:

a. Identical
b. Almost the same
c. Not at all the same
d. Unsure

Pair 3

Describe color 1: ______________________________
Describe color 2: ______________________________
Compare the colors:

a. Identical
b. Almost the same
c. Not at all the same
d. Unsure

Pair 4
Describe color 1: ______________________________
Describe color 2: ______________________________
Compare the colors:
a. Identical
b. Almost the same
c. Not at all the same
d. Unsure

Pair 5
Describe color 1: ______________________________
Describe color 2: ______________________________
Compare the colors:
a. Identical
b. Almost the same
c. Not at all the same
d. Unsure

Pair 6
Describe color 1: ______________________________
Describe color 2: ______________________________
Compare the colors:
a. Identical
b. Almost the same
c. Not at all the same
d. Unsure

Pair 7
Describe color 1: ______________________________
Describe color 2: ______________________________
Compare the colors:
a. Identical
b. Almost the same
c. Not at all the same
d. Unsure

Pair 8
Describe color 1: ______________________________
Describe color 2: ______________________________

Compare the colors:

a. Identical
b. Almost the same
c. Not at all the same
d. Unsure

Pair 9

Describe color 1: ______________________________
Describe color 2: ______________________________
Compare the colors:

a. Identical
b. Almost the same
c. Not at all the same
d. Unsure

Pair 10

Describe color 1: ______________________________
Describe color 2: ______________________________
Compare the colors:

a. Identical
b. Almost the same
c. Not at all the same
d. Unsure

Pair 11

Describe color 1: ______________________________
Describe color 2: ______________________________
Compare the colors:

a. Identical
b. Almost the same
c. Not at all the same
d. Unsure

Pair 12

Describe color 1: ______________________________
Describe color 2: ______________________________
Compare the colors:

a. Identical
b. Almost the same
c. Not at all the same
d. Unsure

BIBLIOGRAPHY

[1] Souk, J.H., Jongseo Lee, "Recent Picture Quality Enhancement Technology Based on Human Visual Perception in LCD TVs"*, Journal of Display Technology,* Volume 3, Issue 4, Pages: 371 - 376, Dec,2007.

[2] http://www.audioholics.com/education/display-formatstechnology/displaytechnologi-esguide-lcd-plasma-dlp-lcosd-ila-crt

[3] http://www.plasma.com/classroom/LCD_tv_versus_plasma_tv.htm

[4] http://www.unbeatable.co.uk/buyingguides/PlasmaVsLcd-Televisions/32.html

[5] Grantham K. H. Pang, Chi-Ho Chan, and Thomas T. O. Kwan , "Tricolor Light-Emitting Diode Dot Matrix Display System with Audio Output" *IEEE Transaction on Industry Applications*, Volume. 37, No. 2, March/April 2001.

[6] Kohrou Takahashi, Nobuyuki Tadokoro and Satoshi Takeuchi, "High Density LED Display Panel on Silicon Microreflector and Integrated Circuit", *Electronic Manufacturing Technology Symposium18th IEEE/CPMT International,* Page(s): 272-275, December 1995.

[7] R. E. Brown, "LED Displays Past, Present, Future", IEEE Transactions on Consumer Electronics, Vol. CE-24, No. 3, August 1978.

[8] J. Wilson, J.F.B Hawkes, *Optoelectronics*, Prentice Hall, UK, 1989.

[9] http://www.lctecdisplays.com/TN_LCD_technology_side_2.asp

[10] http://www.mc2.chalmers.se/pl/lc/engelska/applications/Displays.html

[11] www.wtec.org/loyola/dsply_jp/c5_s2.html

[12] Chun-Ho Chen, Han-Ping D. Shieh, "Effects of Backlight Profiles on Perceived Image Quality for High Dynamic Range LCDs", *Journal of Display Technology*, Volume. 4, No. 2, June 2008.

[13] http://compreviews.about.com/od/multimedia/a/LCDSpecs.htm

[14] http://techgage.com/articles/displays/lcd-monitors/

[15] http://www.businessweek.com/magazine/content/08_30/b4093044731823.htm

[16] http://www.ece.uiuc.edu/alumni/w02-03/plasma_history.html

[17] http://en.wikipedia.org/wiki/Image:Plasma-display-composition.svg

[18] Y. Kim, S. Park, "Simple driving waveform and circuit for plasma display", *Electronics Letters*, Volume 44, Issue 9, Page(s):572 - 572 April 24, 2008.

[19] Dong-Myung Lee, Dong-Seok Hyun, "A New Driving Scheme for Plasma TVs Using Multi-Functional Gate Driver", *IEEE Transactions on Consumer Electronics,* Volume 53, Issue 4, Page(s):1553 – 1559, November 2007

[20] http://www.consumersearch.com/www/electronics/plasma-tv/

[21] http://en.wikipedia.org/wiki/LED_Panels

[22] http://www.neutekled.com/cms/index.php?option=com_content&task=view&id=27-& Itemid =102

[23] http://www.coema.org.cn/E_LEDdisplay.htm

[24] Wyszecki & Stiles, *Color Science*, John Wiley, USA, 1967.

[25] http://www.northdevonhealth.nhs.uk/patientinformation/ophthalmology/understanding_ c ataracts.htm.

[26] http://www.hamwaves.com/antennas/diel-rod.html.

[27] http://www.hyperphysics.phyastr.gsu.edu/hbase/vision/colper.html

[28] http://en.wikipedia.org/wiki/Color_space

[29] Williamson, Samuel J., *Light and Color in nature and art*, John Wiley, Canada.

[30] Marko Tkalcic, Jurij F. Tasic, "Colour spaces - perceptual, historical and applicational background", *EUROCON 2003. Computer as a Tool. The IEEE Region 8,*Volume 1, page(s): 304- 308, September 2003

[31] http://www.mathworks.com

[32] Gaurav Sharma, *Digital Color Imaging Handbook*, CRC Press, 2003

[33] cit.dixie.edu/vt/reading/gamuts.asp

[34] http://www.nichia.com

[35] Muthu, S., Schuurmans, F.J., Pashley, M.D. “Red, green, and blue LED based white light generation: issues and control” *Industry Applications Conference*, Volume 1, Issue Pages: 327 – 333, 2002.

[36] S.Muthu, F. Schuurmans, and M. Pashley, “Red, Green and Blue LEDs for white light illumination”, *IEEE journal on selected topics in quatum electronics,*pp. Vol. 8, No. 2, March/April 2002.

[37] STMicroelectronics, STP08CDC596 An 8-bit constant current LED sink driver with full outputs detection datasheet.

[38] Altera Corporation, DE2 Development and Education Board, User Manual version 1.4

[39] http://www.eecg.toronto.edu/~tm4/rgbout.html

[40] http://web.mit.edu/6.111/www/s2004/NEWKIT/vga.shtml

VITA

Graduate College
University of Nevada, Las Vegas

Neveen Shlayan

Degrees:

Bachelor of Science, Electrical Engineering, 2006
University of Nevada, Las Vegas

Master of Science, Electrical and Computer Engineering, 2008
University of Nevada, Las Vegas

Special Honors and Awards:

Tau Beta Pi, Engineering honor society
Cum Laude, Fall 2006
Best Engineering project award, Fall 2006
Outstanding ECE senior student, Fall 2006
Dean's List award

Publications:

A Novel RGBW Pixel for LED Displays, icseng,pp.407-411, 2008 19th International Conference on Systems Engineering, 2008

Review of Packet Switching Technologies for Future NoC, icseng,pp.306-311, 2008 19th International Conference on Systems Engineering, 2008

Dissertation/Thesis Title: A Novel RGBW Pixel for LED Displays

Dissertation/Thesis Examination Committee:

Chairperson, Dr. Rama Venkat, Ph. D.
Committee Member, Dr. Paolo Ginnobi, Ph. D.
Committee Member, Dr. Emma Regentova, Ph. D.
Graduate Faculty Representative, Dr. Mohamed Trabia, Ph. D.

Appendix D
Detailed Final Report

Task 3
“Hybrid Solar Lighting”

UNLV
Renewable Energy Center
4505 S. Maryland Pkwy
Las Vegas, NV 89154-4027
Phone: 702-895-0429
Fax: 702-895-1123
www.me.unlv.edu/research/energy.htm

Photonics Research and Development
Subcontract #RF-06-PRD-003

Board of Regents, UCCSN,
University of Nevada, Las Vegas

Final Report
Task 3.0 Hybrid Solar Lighting
Subtask 3.2, Southern Nevada HSL
Demonstration Project & Evaluation of Field Units

Submitted by: Ahmad Abu Heiba
UNLV Center for Energy Research

Date submitted:
September 24, 2008

PHOTONICS RESEARCH AND DEVELOPMENT FINAL REPORT
APPENDIX D – TASK 3
HYBRID SOLAR LIGHTING

It was decided to install the HSL system at the Center for Energy Research at Taylor Hall at UNLV. Preparation for installing the system was done by the end of 2006. A concrete base was poured to support a rigid conduit pole on which the tracking system was installed. A 45°Bend was retrofitted into the side wall of the building to route the fibers into the fixtures inside. A meteorological station was also installed on a pole adjacent to the HSL system. The station measures wind speed and direction, ambient temperature, and relative humidity. A normal incident pyrheliometer (NIP) was also installed in an existing solar tracker at the site to measure incident solar radiation. A program was written, installed and tested for the DAS system data logger. Temperature measurements were taken at the exterior of the connection between the fiber optic bundle and the receiver to confirm a set point for a thermal overload which is to be installed in receivers currently being prepared for testing. During testing it was found that the temperature of the fiber optic bundle reached 64.5 °C while the system was tracking at a time when the ambient temperature was 47 °C. The set point for the thermal overload was set for 70 °C.

A Reliability Validation Exercise (RVE) was set up to evaluate the reliability of the fiber optic receivers of the HSL system under a variety of environmental conditions. Over time, Sunlight Direct has put substantial effort into improving the HSL receiver design and understanding its performance. Concurrent with that, they have focused on methods for characterizing the performance of the fiber optic receiver subsystem elements. Sunlight Direct is now capable of quantifying key performance metrics associated with each fiber optic receiver they manufacture. This RVE was an opportunity to develop field performance data at multiple sites during the high-flux, high-temperature conditions of the summer months. Those data would be compared to the characterization data developed during the manufacturing processes at Sunlight Direct. For this exercise UNLV worked with Sunlight Direct, Oak Ridge National Laboratory (ORNL), San Diego State University (SDSU), and Utah State University (USU) in a round robin exchange of receivers to test their performance. An extensive testing schedule was set up for July and August of 2007. The RVE test was started on July 16, 2007 and ended on August 13, 2007. Over the course of the testing period five receiver tubes of different designs were tested. Loss of tracking during this period led to a hole being burnt into the primary mirror. This, in turn, led to delays in UNLV test schedule. Data was collected continuously over the course of the testing period.

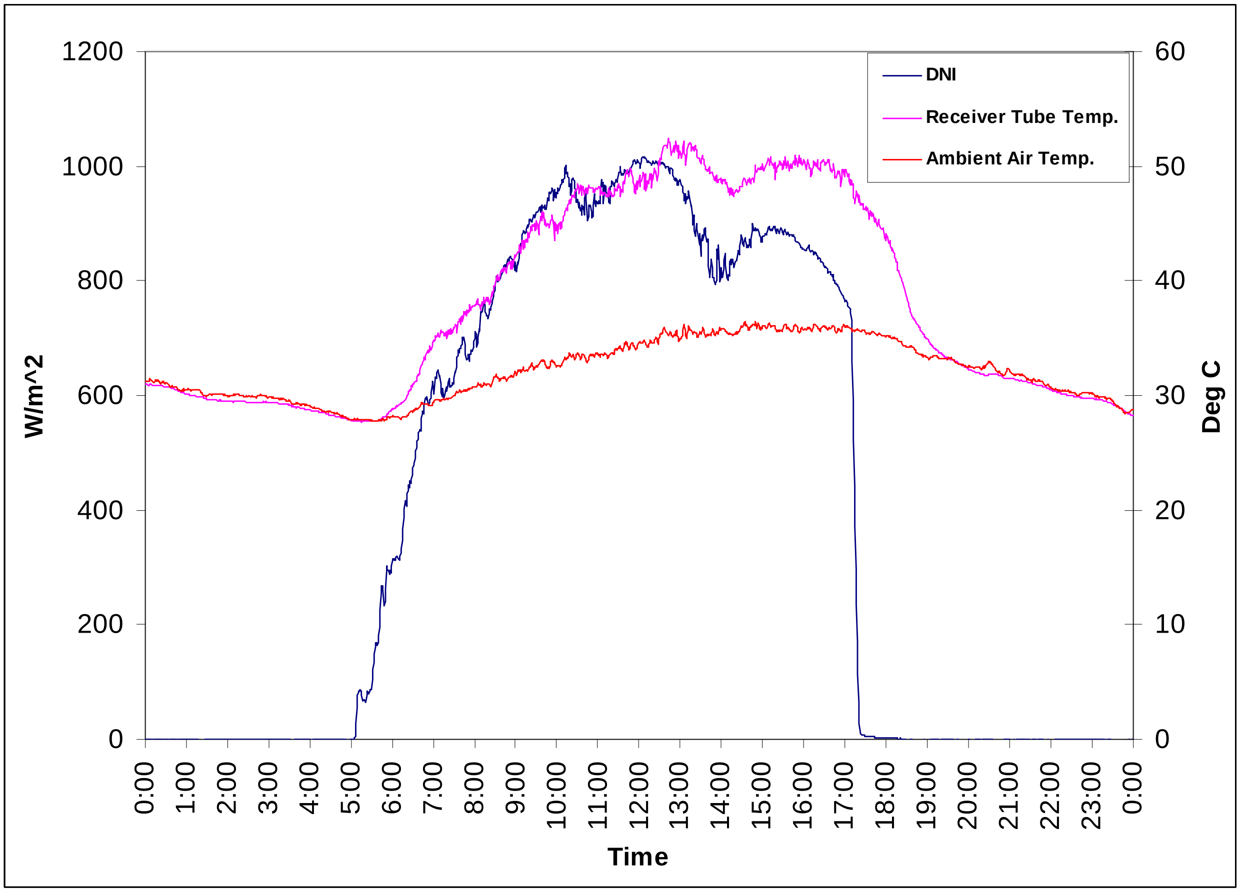

Figure 1 shows a sample of the collected data for one day. Collected data during testing was sent to Sunlight-Direct to be evaluated. If the complete set of data is desired, it will can be furnished on request.

In October 2007, light-dispersing rods in one fixture were removed per Sunlight-Direct request. A different way to disperse the light was decided. Instead of using rods, individual ends of the fibers penetrated the top of the fixture (Figure 2). This new technique was thought to yield more lighting. The rods impart a considerable amount of optical losses (~42%). The rods also don't look as bright as was thought they would be. Instead they look more greenish-yellow. The fixture with the new technique is observed to look brighter.

On Nov 15th, 2007 a press conference was held at Taylor Hall, *Renewable Energy and Energy Efficiency Policies*, sponsored by the Nevada Conservation League (http://nvgreenvote.org/). This was a side event for the CNN Democratic Debate held at UNLV, and the system was displayed and discussed with the visitors. Staff from the Center visited the New Horizons School in Las Vegas on December 10 to see a partial unveiling of their "Greenest Classroom in Nevada" project. Of particular interest was the Sunlight Direct unit that has been installed there. It was only partially in operation, but the personnel at the school were very positive about the effects of the unit on the student learning.

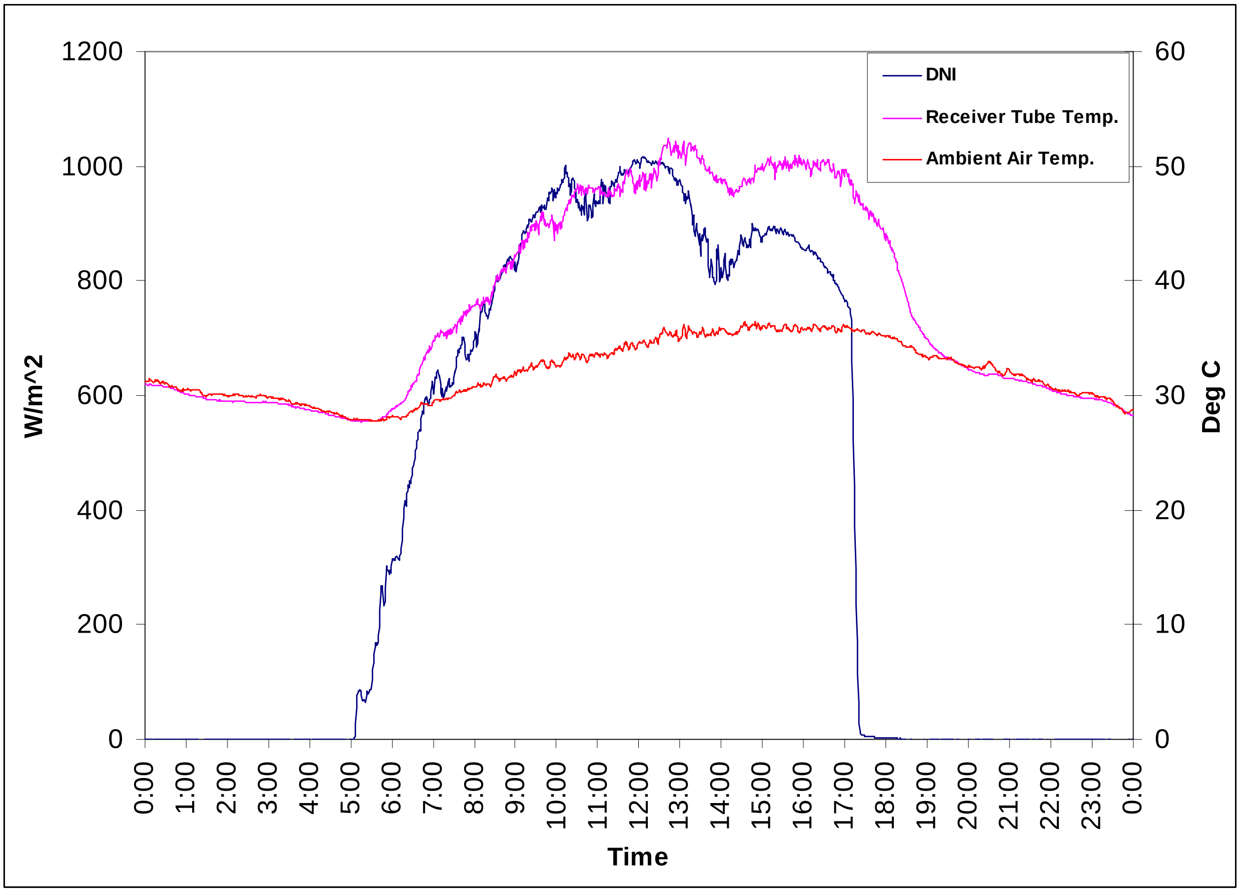

Figure 1. Some of the data collected on 8/6/2007.

Figure 2. The new light dispersing technique.

The tracking was noticed to be off on 9th of March, 2008, that is the first morning after daylight savings time change. Changing the tracker time to match the change in time didn't resolve the tracking issue. An offset in both the west and the up directions had to be set to put the focus back onto the receiver.

On March 20th, 2008, a newly-designed receiver tube was installed (Figure 3). The new receiver tube was tested for two weeks to see if it was going to fail (overheat) or survive under maximum solar flux. The secondary mirror was adjusted to give 100% focal strength. The weather condition (sunny, partly cloudy, or cloudy) was kept in a log. The log was to be used as a quick check of the receiver's environmental stress. The receiver was designed, based on the testing data collected over the course of last year, to meet the maximum solar flux requirement without overheating. At the ends of the two weeks testing period no thermal damage was noticed.

Figure 3. A picture of the newly- designed receiver. The external surface was extended to enhance the dissipation of heat.

Illumination level measurements were taken at Taylor Hall to verify a mathematical model of the HSL system. The illumination measurements will be taken over a 7x5 points (2x4 ft) grid. The points are distributed over the area that the HSL luminaires cover, with one point at the center of each luminaire. Several light meters were purchased to take the measurements. A metal frame was manufactured to mount the meters on and take the measurements. The measurements will be taken fourteen points (2 rows out of five rows) at a time.

PHOTONICS RESEARCH AND DEVELOPMENT FINAL REPORT
APPENDIX D – TASK 3
HYBRID SOLAR LIGHTING

On June 13th, 2008, the optical efficiency of the primary mirror was measured using a special tool supplied by Sunlight-Direct. The optical efficiency was found to be 29.6%. According to Duncan Earl from Sunlight-Direct, this efficiency is typically 80%. Such low efficiency is attributed to the surface errors of the mirror or the coating. Statistically 25% of the manufactured primary mirrors will have such imperfections and in turn low optical efficiency.

In conclusion, two major issues were observed,

1. Tracking; it was noticed to be unstable. The unit loses track often. No pattern was identified over the times that the system had lost track. At times, loss of tracking resulted in physical damage of the primary mirror.
2. Light dispersing; the current rods are obviously not the best way. They are really dim. On the other hand, the new technique has to be modeled to ensure its compatibility with the application in terms of spatial distribution of the light.